Fast and Modular Biomolecular Circuits using Spatial Organization

Gourab Chatterjee

A dissertation
submitted in partial fulfillment of the
requirements for the degree of

Doctor of Philosophy

University of Washington

2017

Reading Committee:

Georg Seelig, Chair

Paul A. Wiggins

Eric Klavins

Program Authorized to Offer Degree:
Bioengineering

University of Washington

Abstract

Fast and Modular Biomolecular Circuits using Spatial Organization

Gourab Chatterjee

Chair of the Supervisory Committee:
Associate Professor Georg Seelig
Electrical Engineering and Computer Science and Engineering,
Adjunct Associate Professor: Bioengineering

Biological information processing hubs ranging from brain to cells to enzyme cascades extensively use spatial organization to process massively parallel molecular instructions and accurately respond to external and internal stimuli. Similarly, human-engineered systems ranging from ancient irrigation networks to modern semiconductor circuits have extensively used spatial organization to steer flux along intended pathways and minimize undesired interactions. In the quest of building artificial nanosystems driven by the fundamental concepts of natural design, DNA has emerged as an incredibly powerful biomaterial due to its biocompatibility, polymeric mechanical properties and predictable sequence programmability. DNA-based nanostructures can potentially detect intracellular or extracellular components like RNAs, proteins or small biological molecules and activate specific bioprocesses (e.g. RNA interference) upon successful detection. Furthermore, these nanodevices can perform molecular computation using one or more intracellular components as input signals and generate an output signal (e.g. a readout or bioprocess activation). During my Ph.D. I have been working on developing a novel class of such DNA-based molecular circuits for molecular computation and molecular imaging

using spatial organization as the fundamental design principle.

In my thesis, I start with presenting a brief overview and key advancements in the field of DNA Nanotechnology (Chapter 1). Here, I have also presented different DNA-based nanosystems that use spatial organization.

For the major part of my Ph.D. I have worked on the design and development of an integrated architecture for building fast and modular molecular circuits on a DNA origami scaffold using spatial localization as a basic design principle (Chapter 2). These spatially-localized DNA-based circuits exhibit significantly faster circuit operation and extensive reuse of circuit components with minimal interference due to spatial localization of circuit components. These nanoscale circuit boards can potentially be used for multiplexed molecular sensing in living cells.

The fundamental challenges for detecting intracellular components in living cells with nucleic acid nanodevices include their *in vivo* stability, efficiency, and control over intracellular localization.We have worked on these challenges and used nucleic acid strand displacement probes to detect intracellular mRNAs in living mammalian cells (Chapter 3). Using the categorically redesigned probes, we performed mRNA quantification and real-time mRNA visualization studies. The findings from this study will act as fundamental guidelines for building complex DNA-based molecular systems which can operate with intracellular components in living mammalian cells.

ACKNOWLEDGEMENTS

The past several years at the University of Washington have been one of the most interesting and memorable phases of my life.

I thank Georg Seelig for being such an amazing advisor. He gave me the freedom to work on new ideas (even if some of them were crazy) while always being there when I needed some advice. His continuous support and encouragement through the ups and downs of my research has helped me grow towards being a better scientist, mentor and communicator.

I thank the other members of my supervisory committee, Eric Klavins, Paul A. Wiggins, Suzie H. Pun and Dustin J. Maly. I got to understand the depth and attention to detail science demands, from the short meetings with Eric in the initial years. Paul, Suzie and Dustin have always given me valuable guidance and asked questions that led me to have a better understanding of my project.

I thank Dorian Taylor Varga, Peggy Sharp and other members of the Department of Bioengineering, UW Seattle, for their constant support and guidance throughout my Ph.D. I have always appreciated your prompt responses and active support in numerous situations.

I thank Neil Dalchau and Andrew Phillips for being amazing collaborators and more importantly great colleagues. I have always admired Neil's calm, positive outlook and Andrew's constant support and encouragement. Their valuable insights and inputs during our conversations really helped me think deeper about my research. I hope we'll con-

tinue our interactions over more projects in future. I also want to thank other members of the Biological Computation Group at Microsoft Research Cambridge, Boyan Yordanov, Colin Gravill, Paul Grant, Sara-Jane Dunn and Luca Cardelli. You are one of the best groups that I have ever worked with and I really enjoyed my stay in Cambridge last year. I hope to do it again sometime.

I thank Richard A. Muscat, Luis Ceze and Karin Strauss for all the valuable feedback and comments during our discussions throughout my Ph.D. I am excited and looking forward for the days ahead.

I want to thank all of the members in Seelig lab (past and present). It has always been fun and exciting to work and chat with Yuan-Jyue Chen. I really enjoyed working on our collaborative projects and I look forward to working with him in the future. I want to thank Randolph, Alex, Sergii, Ben, Sifang, Sundipta, Ahmed, Sherry, Arjun, Paul, Alberto, Nick, Ban, Charlie, Will, Anna, Briana, Alex B., Kali, Sumit, Will, Yue, Anna, Claire for all the fun times in the lab as well as numerous discussions and sharing of ideas. It has been my pleasure to work, play, eat, chat and chill with all of you.

I want to thank all the Klavins lab members (Yaoyu, Leli, Leandra, David, Miles, Nick) and the MOLES 3rd floor members, we have always been one big lab together and it has been great to work and hang out with all of you.

I want to thank all the members of MISL lab. Although I got to know you over the last year, but I have thoroughly enjoyed all the time in the lab, in the lab meetings and outside. You all are great people to be around.

I want to thank National Science Foundation, Microsoft Research, National Institute of Health and University of Washington for providing funding and support for conducting my research.

I thank Debosmit Ray, Bijetri Bose, Nitin Agarwal, and Debmalya Sinha for making Seattle a home away from home. This is just the start! I also want to thank friends, colleagues and acquaintances whom I met in Seattle and outside during all these years, specially Devjyoti, Aditya, Suvankar da and Anamol. The journey wouldn't have been the same without all of you.

Thank you Jagori Saha, for being in my life and allowing me to be in yours. Here's to many more years to come!

And, Thank you Maa, Baba, Bhaida, Boudi and my little niece Saranya (Khushi) for always being there for me. A few lines or pages will never be enough to describe what you all have done for me. I have been, I am and I will always be grateful to have you as my family and to be a part of your lives.

Contents

List of Figures

List of Tables

DEDICATION

to my Family

Chapter 1

DNA NANOTECHNOLOGY AND SPATIAL ORGANIZATION

DNA nanotechnology utilizes predictable sequence programmability of DNA strand interactions to rationally design different nanoscale systems with a wide range of applications. Specific DNA sequences can be designed to create functional devices with interesting steady state behavioral characteristics or unique out-of-equilibrium dynamics (Dynamic DNA Nanotechnology). Elementary DNA sequences can also self-assemble into multi-dimensional nanostructures. DNA-based nanostructures can be used as elementary building blocks or uniquely addressable scaffolds for different applications in biomaterial research and development. I am involved in an ongoing work with Georg Seelig, Yonggang Ke, Carlos Castro, Hao Yan, Pengfei Wang and Andrew Turberfield for a comprehensive review introducing Structural and Dynamic DNA Nanotechnology to the Materials Research Community. My main focus has been on presenting the use of spatial organization in DNA-based nanostructures for exhibiting chemical reaction pathways and reaction-diffusion systems. The version presented in this chapter has a brief introduction to DNA Nanotechnology followed by a draft of the above-mentioned topics in the last two sections.

1.1 Introduction

DNA-based molecular nanosystems have rapidly emerged over the last few decades as interdisciplinary efforts combining biochemistry[1, 2], material science[3, 4], engineering[5, 6] and computation[7]. The predictable interactions between nucleic acid sequences through

Watson-Crick base pairing has made synthetic DNA sequences, a widely recognized raw material for development of simple and complex molecular nanostructures. Due to the biocompatibility of DNA, DNA-based nanostructures have been developed for interaction with mammalian cell surface markers for targeted cell-based therapeutics[8, 9, 10] and intracellular delivery[11, 12, 13]. Several dynamic nucleic acid devices have shown potential applications towards cellular bio-sensing[14, 15], detection of cellular RNAs[16] and intracellular regulation through RNA interference (RNAi)[17, 18, 19]. Recently, molecular systems comprising of synthetic DNA components have been delivered inside mammalian cells[20] and used to perform molecular computations upon detection of combinations of intracellular miRNAs. Although the state of use of nucleic acid based nanosystems may be far from ready for being used in clinical scenarios, there is tremendous potential of such technologies for towards personalized nano-medicine. Cell lysates[21] and fixed cells are also used by researchers as analogous but less complex environments for proof-of-concept tests with DNA nanostructures aimed towards cellular applications. To this end, DNA-based molecular devices have been used in fixed cells to improve the sensitivity and specificity of existing imaging methods like fluorescence in situ hybridization (FISH)[22, 23].

Studies within the domain of DNA nanotechnology can be broadly classified into two focus areas: Dynamic and Structural DNA nanotechnology[7, 1].

1.2 Dynamic DNA nanotechnology and strand displacement

Dynamic DNA nanotechnology focuses on using programmable DNA hybridization between different DNA complexes to create reconfigurable and autonomous devices, which are capable of producing unique temporal behaviors upon self-assembly. DNA-based interactions in molecular systems are mainly governed by two important concepts: forma-

tion of base pairs which leads to enthalpy gain of the system, and, release of DNA strands which leads to entropy gain[7], both of which results in free energy for driving the reactions forward. The interactions in dynamic DNA-based molecular circuits are largely based on the underlying mechanistic phenomenon: DNA strand displacement. DNA strand displacement is a process through which two DNA complexes with partial or full complementarity interact with each other, displacing one or more pre-hybridized strands from the participating complexes. The process is generally initiated by hybridization through a single stranded domain termed as toehold, and proceeds through a random walk process consisting of reversible single nucleotide hybridization and dissociation steps known as branch migration. The branch migration process culminates with eventual displacement of a single stranded sequence from the participating double-stranded complex. This process is driven forward due to gain in enthalpy due to base pairing at the toehold, and gain in entropy due to strand release.

Following up on the pioneering work on strand displacement by Yurke et al.[24], Simmel and Yurke[25] used toehold-mediated strand displacement to develop a nanoactuator that switches from a relaxed circular form to a stretched conformation. This was followed by a series of studies with DNA tweezers, refining them to act as autonomous devices[26], and using the concept to act as a force gauge[27], developing freely interacting semi-autonomous and autonomous nanomechanical devices controlled by DNA. Seelig et al.[28] proposed and tested designs for Boolean logic gates that used short DNA oligonucleotides as input and output signals, using only strand displacement. They also demonstrated cascaded logic circuits that exhibited a complete set of logic functions (AND, OR and NOT) with thresholding and signal restoration, where a multi-component circuit was shown to demonstrate the correct digital output with varied concentrations of the inputs. Qian and Winfree[29] proposed a general approach of constructing logical AND

and OR gates from a basic gate motif with amplification and thresholding. They demonstrated how arbitrary feed-forward digital logic circuits, relay contact circuits, and various analog circuits could be systematically built from their approach. In reality, chemical reaction kinetics follow analog behavior with a wide range of variations like oscillations and pattern formation leading to significant signal fluctuations on operation. Soloveichik et al.[30] suggested a systematic approach for approximating arbitrary mass action kinetics and suggested an automated process for implementing a system of coupled chemical reactions through DNA strand-displacement cascades. Using DNA strand displacement, Zhang et al.[31] demonstrated an extensive study on the effects of thermodynamic properties of hybridization and developed a molecular toehold exchange probe that enables near-optimal single-base discrimination and perform robustly across diverse temperature, salt and conditions.

In typical strand-displacement reactions, the single-stranded input is converted to an inert double-stranded by-product. However, researchers have explored mechanisms through which the same input molecule can participate in multiple strand-displacement reaction cycles, thereby leading to the release of many outputs. This concept led to the design and development of non-covalent DNA catalytic system, where DNA strands or complexes kinetically trapped in metastable configurations are used as fuels to thermodynamically drive the catalytic reaction forward by fast rearrangement of the fuels to products. This concept was first explored by Turberfield et al.[32] as a system with two complementary strands with constrained hybridization via binding to shorter auxiliary strands. Addition of a specific input strand released the auxiliary strands and catalytically accelerated the formation of the double-stranded product. Seelig et al.[33] reported an improved version of non-covalent DNA catalytic systems with significantly lower leakage using reactant complexes with complementary DNA hairpin or bulge structures, where

the sequence of the released single-stranded output was unrelated to the input. The standardized design of the system made it applicable for modular implementation and design of multilayered DNA strand-displacement cascades.

DNA hairpins have been explored as excellent examples of metastable DNA complexes which can sequester toehold domains in inactive states within the hairpin loops and act as fuels for autonomous DNA devices[34]. In a DNA strand-displacement cascade, the output from one reaction serves as the input to a downstream reaction. Dirks and Pierce[35] reported the use of DNA hairpins in strand-displacement cascade reactions, where sequestered toeholds in the hairpin loop of any hairpin were initially inactive, but addition of an initiator strand accelerated the reaction. DNA hairpins have been studied to possess significant potential towards design and conceptualization of spatially localized circuit designs[36] as the toehold domain exposed on reaction of one hairpin remains localized to the complex and can readily interact with the next available hairpin. Using modular representation and design of multilayered reaction cascades, Zhang et al.[37] rationally demonstrated the first example of a catalytic system that is driven by the entropy gain of additional released molecules, rather than enthalpy gain of base-pair formation. Zhang and Winfree[38] further improved this entropy-driven catalyst system to allow dynamic allosteric modulation. Qian and Winfree[39] demonstrated the extensive use of a relayed catalytic motif to scale up strand displacement cascades and demonstrated a multilayered complex molecular circuit capable of performing square root function. Recently, Chen et al.[40] developed a conditionally fluorescent molecular probe using the specificity of DNA strand displacement and a four-way branch migration process, capable of discriminating single nucleotide mismatches and showed its applicability towards detection of microbial antibiotic resistance. Recently, DNA origami technique has also been used to construct DNA nanostructures with dynamic behaviors[41].

1.3 Structural DNA nanotechnology and DNA origami

Structural DNA nanotechnology focuses on assembly of complex multi-dimensional structures from basic bricks with nanometer resolutions since the concept of use of nucleic acid sequences (oligonucleotides) as a structural engineering material was introduced by N. Seeman[42]. Subsequently, Winfree et al.[43] and others used DNA nanotiles assembled from multiple oligonucleotides to self-assemble a variety of two and three dimensional DNA lattices and other spatially patterned DNA structures[44, 45]. Rothemund[46] introduced the concept of scaffolded DNA self-assembly by developing the DNA origami technique. DNA origami relies on assembly of a long single-stranded scaffold strand into a target structure through controlled hybridization with a large number of short staple strands. This technique was widely adopted and explored by others to develop sophisticated self-assembled 3D DNA nanostructures[10, 47]. This technique offers a wide range of flexibility towards designing unique molecular structures from DNA sequences[48, 49], which can be modified with other functional components with nanoscale precision[50, 51].

1.4 Spatial organization for programmable biomolecular reactions

Several DNA-based nanoscale supramolecular structures had been built using spatial organization as a fundamental design principle. The intended behaviors range from molecular machines for cargo transport to molecular imaging tools to nanoscale computational circuits for molecular logic. This section highlights some of the key advancements.

Initial attempts on building nanoscale molecular machines were inspired by intracellular bipedal walkers like kinesin which are capable of transporting intracellular cargo over distances in the range of micrometers. Towards designing nanomachines that can perform simple unidirectional motion relative to an external substrate, Sherman and Seeman[52]

presented the first design of a DNA-based biped walker which perform worm-like movement along a precisely controlled path. Shin and Pierce[53] continued the efforts by demonstrating a kinesin-like DNA nanomotor that can walk along a pre-programmed double-stranded DNA track. These devices however lacked synchronicity in motion and were dependent on sequential addition of helper fuel strands for step-wise motion. Yin et al.[54] demonstrated an autonomous enzyme-free bipedal DNA walker capable of stochastic locomotion along a defined DNA track. Shortly after, Omabegho et al.[55] demonstrated the example of an autonomous DNA bipedal walker that performed coordinated brownian motion on a double stranded DNA backbone with the help of fuel strands. Several other studies on enzyme-assisted() and enzyme-free DNA walkers[56, 57] and motors[58, 59] performing controlled motion along a predefined path on a double-stranded DNA track have been published.

The advent of scaffolded DNA origami technique by Rothemund[46] widened the possibility of designing DNA-based assemblies as precisely addressable biomolecular scaffolds for creating spatially organized landscapes. A multi-dimensional DNA origami scaffold can be precisely modified to create one or more predefined paths for more complex operation of molecular motors over longer distances and more complicated paths. Lund et al.[60] showed the operation of a spider-shaped DNA walker capable of moving via an excited walk process along a spatially organized path on two-dimensional DNA origami scaffold (Fig. 1.1,A). Wickham et al.[61] demonstrated the stepwise programmable motion of autonomous but nicking enzyme-assisted processive motors along user-defined paths on a DNA origami scaffold (Fig. 1.1,B). Gu et al.[62] demonstrated an enzyme-free tensegrity-triangle shaped DNA walker that can transport along a defined path on a two-dimensional DNA origami tile scaffold (Fig. 1.1,C). With the ultimate goal of building molecular motors capable of striding longer distances, Liber et al.[63] showed

the operation of an enzyme-free bipedal DNA motor which can move back and forth between two independently annealed origami tiles which were assembled together (Fig. 1.1,D). Recently, Tomov et al.[64] designed an integrated microfluidics and fluorescence microscopy interface for higher processivity, control and system characterization, which allowed a bipedal DNA walker to carry up to 32 steps on a DNA origami track (Fig. 1.1,E).

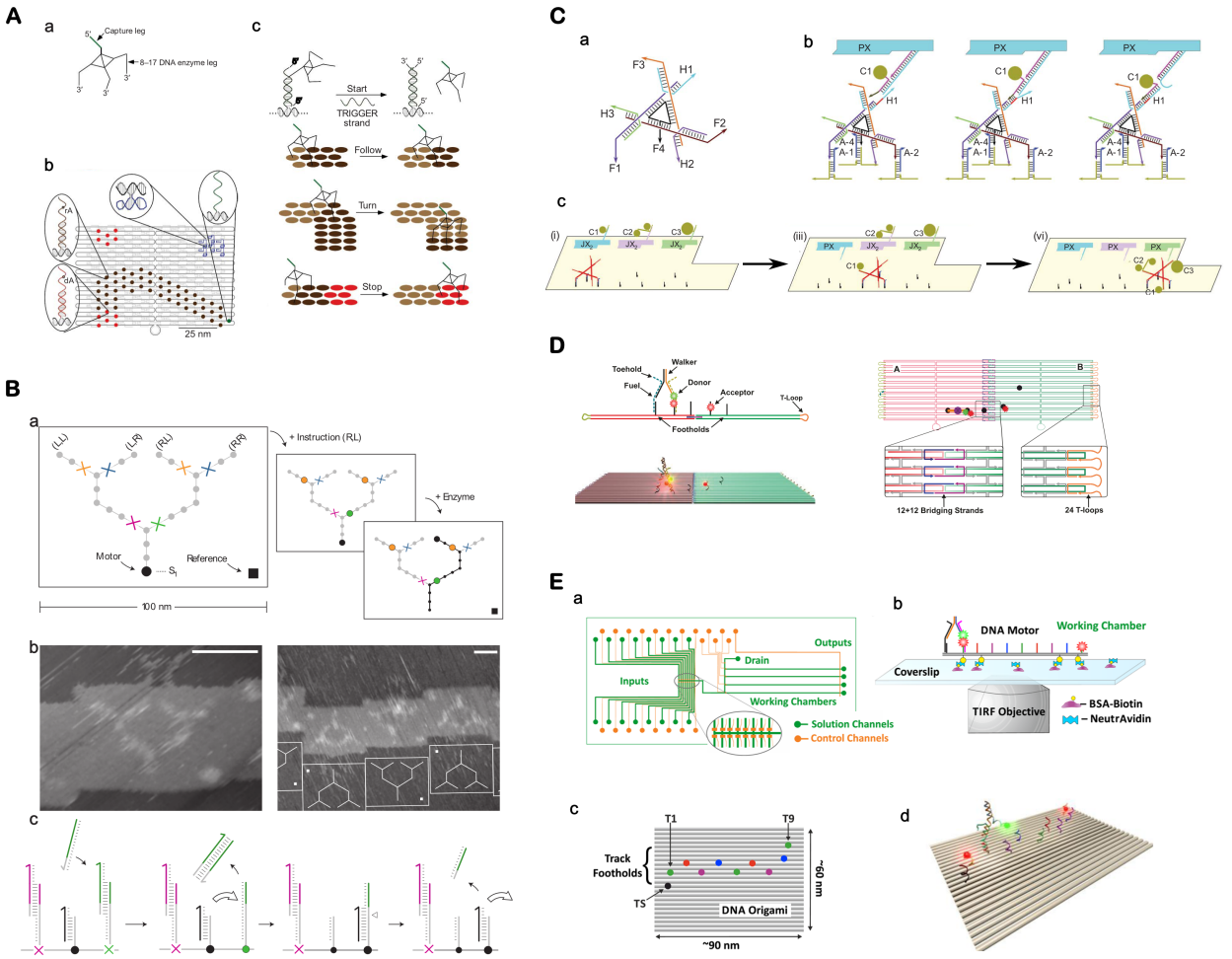

Figure 1.1: DNA nanomotors operating on precisely modified DNA origami scaffolds. A:a) Stick representation of the spider DNA-walker. b) A representative origami landscape. c) Schematic representation of the walk. ref:[60] **B:**a) The DNA track network assembled on a rectangular DNA origami substrate. Selective displacement of blocking strands from junction stators (coloured crosses) opens just one path. The motor (black circle) travels down the open path, destroying the track behind it. b) Tracks decorated with excess motor visualized by AFM (scale bars, 50 nm). c) Interaction mechanism.ref:[61] **C:**a) Walker structure. b) Cargo transfer. The PX state brings the arm of cassette one close to H1 (left), the brown toehold binds its complement (red; centre) and branch migration transfers the cargo strand to H1 (right). c) The basic components of the system are the origami tile (tan outline), programmable two-state DNA machines inserted in series into the file (blue, purple and green) and the walker trigonal arrangement of DNA double helices in red).ref:[62] **D:** Origami-A and B were connected using the bridging strands strategy(blue and purple strands). The track contained five footholds that branched from the origami plain (black dots and strands); three were located on origami-A, and two were located on origami-B. The walker leg (green indicates donor) and two of the footholds (red indicates acceptors) were labeled with fluorophores to enable single-molecule fluorescence monitoring.ref:[63] **E:**a) Diagram of the of the microfluidics device. c) DNA origami contains 10 protruding foothold strands (TS and T1T9; different colors indicate different DNA sequences), which form the track on which the walker strides. d) Three-dimensional schematic of the motor.ref:[64]

The high accuracy of spatial addressability with DNA origami scaffolds have been utilized for building a wide range of biomolecular systems with interesting features. Zhou et al.[65] demonstrated an active plasmonic system by directional and progressive transport of a plasmonic nanorod on a multi-layered DNA origami scaffold through nucleic acid hybridization and strand displacement (Fig. 1.2,A). DNA origami scaffolds have been extensively used as platforms for analyzing different classes of interactions using single-molecule imaging, as discussed in this excellent review by Rajendran et al[66]. Recently, Jungmann et al.[67] demonstrated a novel quantitative super-resolution imaging technique using precisely positioned fluorophore docking sites on a DNA origami scaffold, called qPAINT (Fig. 1.2,B).

The field of DNA Nanotechnology has heavily invested in the development of DNA-based molecular circuits capable of exhibiting a wide complexities of molecular computation, primarily using nucleic acid strand displacement. Due to the simplicity and predictability of DNA interactions using strand displacement, demonstrations of DNA-based molecular circuits rapidly escalated to exhibit complex behavior[28, 68] and large scale[39]. But concerns about practical limitations for complex circuit designs with freely interacting components have also been raised about non-specific interactions due to partial complementarity between strands designed with A, T, G and C (four nucleotides). There has been a major interest towards circuit designs with spatially localized components, where DNA sequences can be reused with minimal possibility of non-specific interaction. In spatially localized molecular circuits, only components close to each other can interact, while components separated by appropriate distances would have minimal interactions owing to structural limits[36, 69]. Dalchau et al.[70] presented a theoretical analysis overview on the dynamics of spatially localized circuits. Muscat et al.[36] presented a novel design of DNA-based molecular circuits with spatially localized compo-

nents based on hybridization chain reaction[35]. This work was recently experimentally realized as part of my doctoral research (described in more details in Chapter 2) through precise spatial organization of circuit components on a DNA origami scaffold (Fig. 1.2,C). Using the modular DNA domino architecture, we showed that spatial localization of DNA circuit components significantly improves reaction speed, and demonstrated a class of basic and advanced spatially localized molecular circuits with extensively reused circuit components.

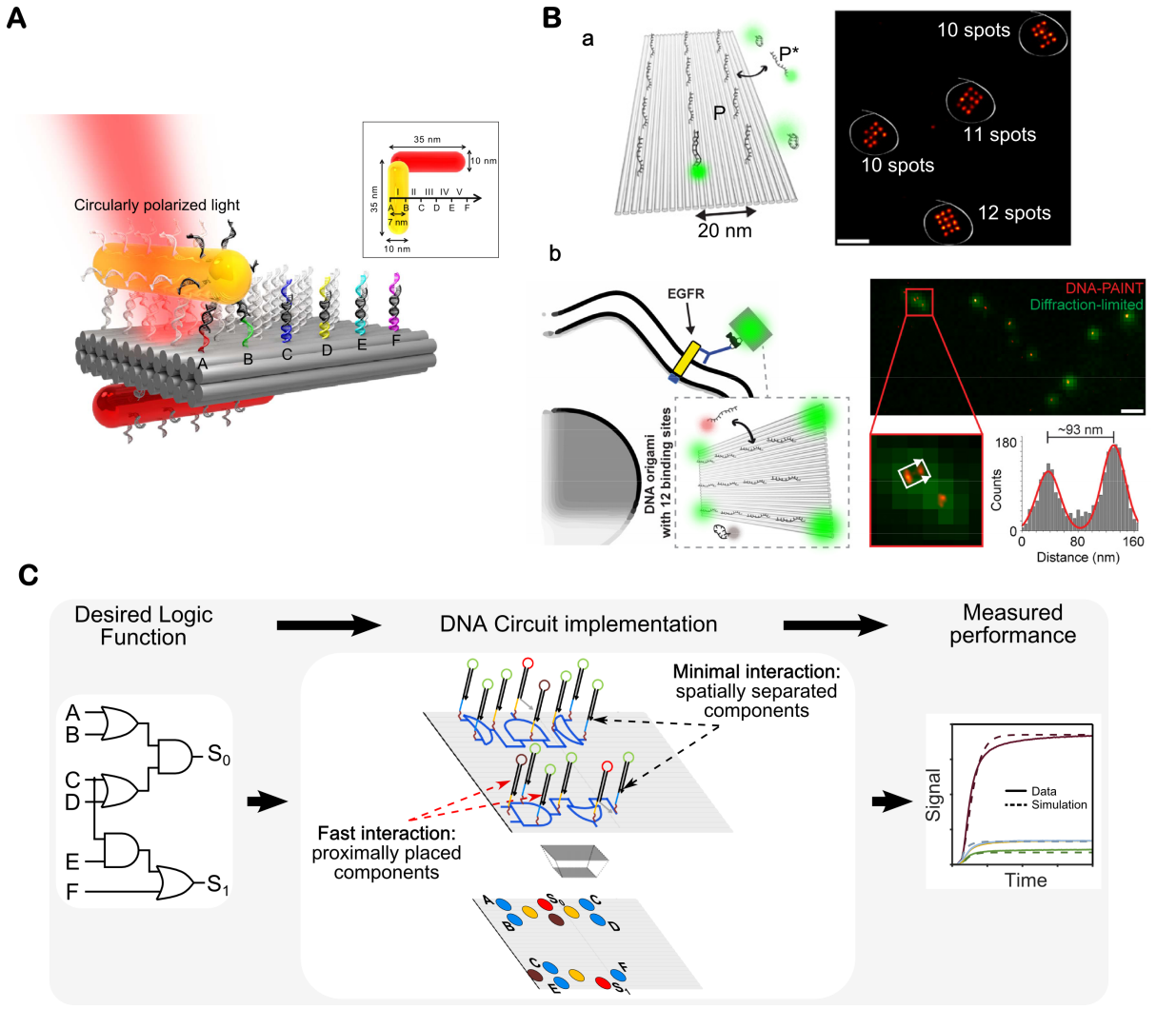

Figure 1.2: Use of spatially addressable DNA origami scaffolds for biomolecular applications. **A:** Schematic of the plasmonic walker.ref:[65] **B:**a) DNA origami structure with 12 designed docking sites(left) DNA-PAINT image of the structures(right). b) CHO cells were transfected to transiently express EGF receptors (EGFR). EGFR labeling is performed with pre-assembled antibody-DNA origami conjugates (44 fixed Cy3 labels,12 DNA-PAINT docking sites for Atto 655-labeled imager strands); Diffraction-limited (green) and super-resolved DNA-PAINT image (red) of DNA origami on a cell membrane. Transverse profile of two origami structures on a cell membrane in the boxed region are spaced 93 nm apart.ref:[67] **C:** Schematic representation of the spatially-localized architecture: A desired logic function (left) is mapped on the DNA origami scaffold (middle) and corresponding staple strands are modified with hairpin components. The circuit is prepared and tested to get the resultant output profile (right).ref: Chapter 2

1.5 Use of spatial organization for reaction-diffusion systems

Biological organisms exhibit complex behavior and functions through a spatio-temporal synergy between different simultaneously operating simpler sub-components. Bioprocesses ranging from mitotic spindle formation[71] to embryonic differentiation[72] result from synchronized molecular functions communicated through diffusible signalling molecules across distances beyond the cellular scale. As discussed before, there has been commendable progress in designing artificial systems with a wide range of structure and functions using DNA Nanotechnology. Several enzyme-assisted DNA circuits have shown non-equilibrium dissipative behaviors like nonlinear oscillators[73, 74, 75] and memory switches[76]. But, for developing artificial molecular systems which can replicate the complexity and scale of biological organisms, programmable communication between interacting components is important. One promising approach for such cell-free biochemical system design is to use spatially organized landscapes with localized components which interact via reaction-diffusion of signal molecules. This section discusses some of the key contributions using this approach.

Bauer et al.[77] presented one of the first examples of spatially organized in vitro biochemical systems as RNA travelling waves evolving across a viral enzyme loaded capillary bed. Isalan et al.[78] then demonstrated a cell-free transcription-translation framework that mimics the spatial patterning seen during Drosophila embryo morphogenesis. Padirac et al.[79] reported a bottom-up chemical reaction network that generates travelling concentration waves based on a predator-prey model (Fig. 1.3,A). Zadorin et al.[80] showed a nicking enzyme (PEN) toolbox based reaction-diffusion system which propagates an autocatalytic travelling wave with precisely controlled reaction and diffusion rates. Recently, they extended this concept by combining two bistable circuits to induce a French flag pattern of colloidal aggregation[81] (Fig. 1.3,B). However, these circuit op-

erations require modification of component DNA molecules with nicking enzymes and polymerases and can be highly sensitive to reaction conditions.

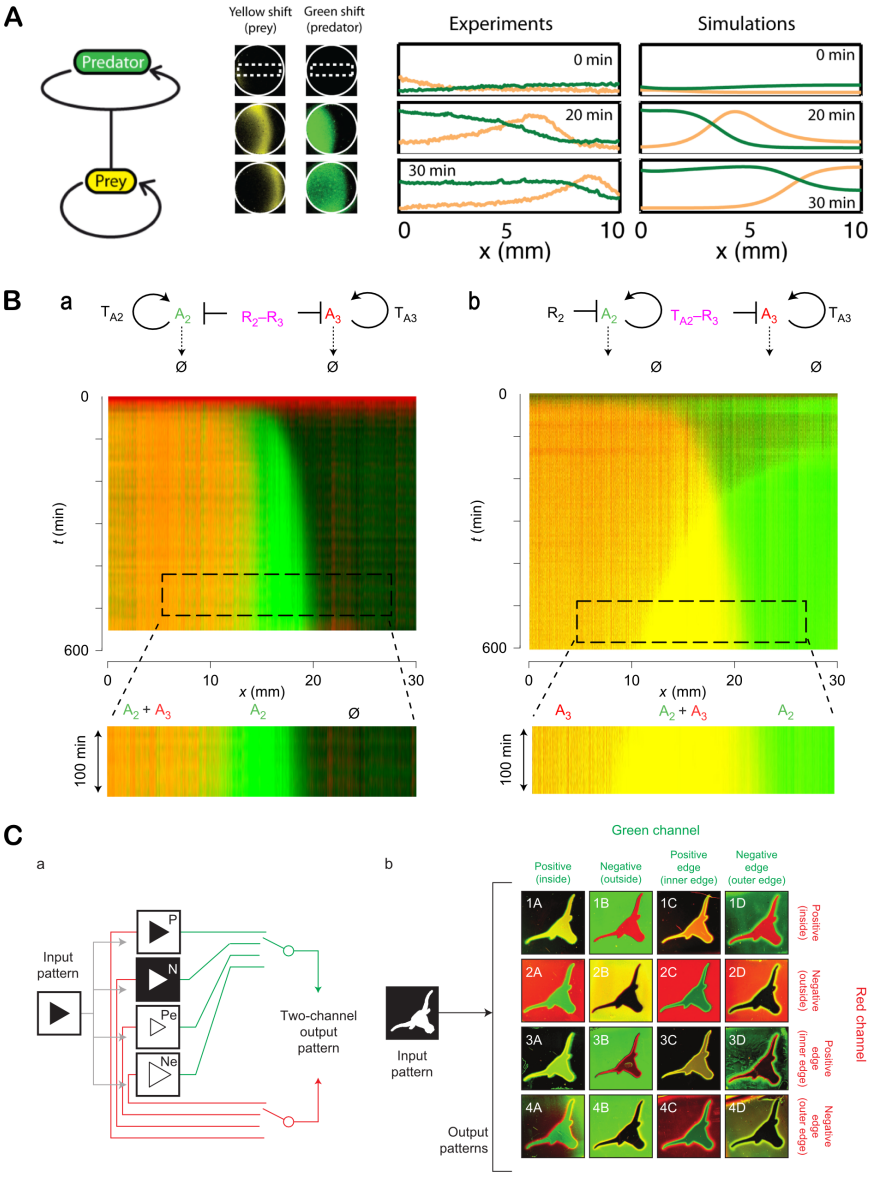

Figure 1.3: Spatially organized reaction-diffusion systems. A: a) Schematic circuit diagram of the predator-prey model(left), A wave of predators follows the wave of preys in a predatorprey molecular network. (left) Time-lapse images of the fluorescence shifts in the yellow channel (corresponding to the prey concentration) and the green channel (corresponding to the predator concentration), taken every 10 min in an 11 mm diameter, 200 m thick circular reactor (middle); Profiles along x of the yellow (prey) and green (predator) fluorescence shifts corresponding to the images on the left, averaged in the white dotted rectangles (right).ref:[79] **B:** The combination of two orthogonal bistable networks produces a French flag pattern of DNA concentration that can be simply reprogrammed. a,b, From top to bottom: network topology, initial morphogen gradient, kymograph and fluorescence shift profiles at steady state.ref:[81] **C:** a) Scheme of the pattern-transformation programs. P, positive image; N, negative image; Pe, positive edge; Ne, negative edge. b) A total of 16 different two-channel output patterns generated from the same input pattern through 16 different pattern-transformation programs.ref:[82]

Scalise et al.[83] developed a reaction-diffusion based theoretical framework for generating arbitrary patterns from a minimal set of localized DNA signals through repeatable transformations of a pattern of chemical concentrations. Dalchau et al.[84] presented a computational framework for programmable spatially organisation of DNA at the centimeter scale, using DNA strand displacement reaction-diffusion systems. Chirieleison et al.[82] demonstrated the first example of macro-scale spatial patterns via programmed reaction-diffusion processes only using DNA strand displacement systems (Fig. 1.3,C). These enzyme-free edge-detection circuits converted a UV light directed binary input pattern into an output which highlights the boundary of the input pattern. The input was activated via UV-directed photo-cleavable bases and the system operation was primarily dependent on simple linear catalytic reactions which aids to more precise programmability of circuit behavior. Zenk et al.[85] presented a continuous release-and-capture motif that can generate stable single and multiplexed spatial patterns on a hydrogel substrate using enzyme-free DNA strand displacement reactions.

Chapter 2

A SPATIALLY LOCALIZED ARCHITECTURE FOR FAST AND MODULAR DNA COMPUTATION AT THE MOLECULAR SCALE

Existing DNA-based molecular circuits majorly rely upon freely floating circuit components in solution. So, design of complex molecular circuits involves extensive cross-verification among the components for minimal non-specific interaction via partial complementarity, increasing code pressure. This puts a practical limitation towards designing more complex molecular systems due to the constraints in the number of orthogonal sequences that can be designed. Although several proposals have been made about the promise of designing DNA-based molecular circuits with spatially localized components, but demonstration and exploration of experimental viability of spatially localized molecular circuits on DNA origami scaffolds is unexplored so far. Building on the theoretical demonstration by Muscat et al.[86], I developed a spatially-localized architecture for building DNA-based molecular circuits which are significantly faster and had repeatable circuit components. The circuit interaction was primarily guided by spatial positioning and there was minimal interaction between complementary domains which were positioned far from each other. Richard Muscat guided me towards initiating the project. Neil Dalchau and Andrew Phillips performed the modeling studies. This work was recently accepted for publication in Nature Nanotechnology and is currently undergoing editorial formatting. The work presented here is the final version of the manuscript submitted for review with a modified supplement file. For a complete version, please check online: "Gourab Chatterjee, Neil Dalchau, Richard A. Muscat, Andrew Phillips, Georg

Seelig.(2017). *A Spatially Localized Architecture for Fast and Modular DNA Computing*."

2.1 Abstract

Cells use spatial constraints to control and accelerate the flow of information in enzyme cascades and signaling networks. Here we show that spatial organization can be a similarly powerful design principle for overcoming limitations of speed and modularity in engineered molecular circuits. We create logic gates and signal transmission lines by spatially arranging reactive DNA hairpins on a DNA origami. Signal propagation is demonstrated across transmission lines of different lengths and orientations, and logic gates are modularly combined into circuits that establish the universality of our approach. Because reactions preferentially occur between neighbors, identical DNA hairpins can be reused across circuits. Co-localization of circuit elements decreases computation time from hours to minutes compared to circuits with diffusible components. Detailed computational models enable predictive circuit design. We anticipate that our approach will motivate the use of spatial constraints in molecular engineering more broadly, bringing embedded molecular control circuits closer to applications.

2.2 Introduction

Human-engineered systems, from ancient irrigation networks to modern semiconductor circuitry, rely on spatial constraints to guide the flux of materials and information. Cells similarly use spatial organization[87], through enzyme scaffolds[88, 89] or organelles[90] to perform complex information processing tasks within a crowded intracellular environment [91, 92]. Such spatial constraints play a pivotal role, by accelerating interactions between components that are closer together, and reducing interference between those that are further apart. Not surprisingly, spatial organization has been recognized as a

potentially powerful engineering principle for the construction of synthetic molecular circuitry. However, in practice, synthetic circuits have so far relied almost exclusively on interactions between diffusible components guided by chemical specificity[93, 94, 95]. As a result, scaling up such circuits for complex and parallel computation rapidly becomes intractable, due to the limited availability of orthogonal components. Here, we demonstrate a novel design paradigm for realizing scalable molecular logic circuits with a minimal set of orthogonal components, using spatial organization rather than sequence specificity as the main organizing principle. DNA nanotechnology provides an ideal framework for exploring the use of spatial constraints in molecular circuit design. First, DNA origami forms a uniquely programmable scaffold for the controlled arrangement of molecular circuit elements[46]. Second, research on DNA-based walking motors corroborates the notion that programmed, multi-step reactions can occur in DNA systems with spatial constraints. Over the last decade such DNA walking motors, mainly powered by enzyme catalysis, have progressed from being able to make a small number of externally triggered steps to autonomously moving along multi-step tracks laid out on a DNA origami[61, 86, 62, 60]. Walking motors could in principle be programmed to perform computation[96, 97, 98]. However, by considering that only information needs to propagate in a computational circuit, rather than a specific motor molecule, we open up a much broader design space for engineering. Third, DNA strand displacement[24, 7] provides a mechanism for the rational design and implementation of complex digital[28, 39] and analog[99] circuits, neural networks[68] and reaction diffusion patterns[82], with quantitatively predictable behaviors. Such DNA strand displacement circuits form a benchmark for success, but also pose a set of challenges that need to be overcome through novel design approaches. In particular, circuit operation is slow at experimentally realistic concentrations. Furthermore, unintentional binding interactions between sequences degrade

performance and increase with circuit size, leading to a lack of modularity in circuit design and execution.

Several theoretical papers have proposed DNA circuit architectures that take advantage of spatial constraints to overcome these limitations of speed and modularity[36, 69, 70, 100]. Limiting interactions to spatially proximal circuit elements should result in faster reactions, since spatial localization allows the effective concentrations of components to be substantially increased, compared to components in solution. Moreover, sequences can be reused across components because proximity rather than chemical specificity controls information flow. Recent experimental work has begun to characterize the kinetics of strand displacement reactions with localized components, providing evidence for an increase in circuit speed due to localization[101, 102], and elementary localized DNA logic gates have also been built[103, 104]. However, an experimental realization of a scalable circuit architecture that exploits the advantages of spatial organization is still lacking.

Here we experimentally demonstrate a modular design strategy – the "DNA domino" architecture – that uses spatial organization to realize fast arbitrary logic at the molecular scale. Domino gates and signal transmission lines (wires) are realized with DNA hairpins laid out on a DNA origami scaffold (Fig. 2.1a, Supplementary Fig. 2.6). In practice, hairpins were localized on the origami scaffold by extending the appropriate origami staple strands with the hairpin sequences. After assembly, origami were purified to remove unincorporated hairpins. The reaction mechanism underlying circuit operation reimagines the hybridization chain reaction (HCR)[35], such that polymerization occurs along designed trajectories on a DNA substrate[36]. All reactions are rationally designed and, unlike most DNA walking motors, no enzyme or ribozyme catalysis is required for operation.

2.3 Localized signal propagation mechanism

To illustrate how information is propagated spatially, we consider the "DNA domino effect" in a minimal two-hairpin wire comprised of an Input and Output hairpin attached to a DNA origami scaffold (Fig. 2.1b). In each reaction step, a hairpin stem is unwound and a toehold that is initially sequestered in the hairpin loop becomes available, to initiate the unwinding of a subsequent hairpin stem. The Input hairpin is opened by binding of an input strand, which enables the capture of a diffusible Fuel hairpin. Requiring a diffusible Fuel ensures that no unwanted reactions can occur between Input and Output hairpins during initial assembly of the origami. Previous theoretical work proposed an alternative fully-localized architecture that does not require a diffusible fuel [69, 70]. While such a localized fuel architecture could enable faster computation, care also needs to be taken to avoid spurious leaks between fully localized components [70]. In practice, the Fuel can be added in large excess over the concentrations of the other components, and thus does not substantially limit reaction speed. The Output hairpin is opened by the Fuel-bound Input hairpin via a fast local interaction. Finally, the activated Output hairpin displaces the quencher-labeled strand from the diffusible Reporter complex, resulting in increased Reporter fluorescence.

To demonstrate the benefits of spatial organization, we experimentally compared signal propagation between Input and Output hairpins, positioned at different distances from each other or on different scaffolds (Fig. 2.1c). We first confirmed that a signal could rapidly propagate across proximally positioned Input and Output hairpins (single spacing) in a two-hairpin wire ($t_{1/2}$ <3 mins). No observable signal transfer was observed without input addition. We then doubled the distance between Input and Output hairpins (double spacing) on the same origami, and showed that separating the hairpins beyond their theoretical maximum reach resulted in minimal signal transfer (Fig. 2.1c,

Supplementary Fig. 2.11). Furthermore, we found that interactions between Input and Output hairpins on two different origamis were significantly slower than single-spaced hairpin interactions on the same origami, and comparable to the double-spaced hairpin interactions. Crucially, decreasing the operating concentration of the origamis did not affect the speed of localized intra-origami signal propagation, but significantly reduced the speed of non-localized inter-origami interactions (Supplementary Fig. 2.12). Finally, we performed kinetics experiments with two-hairpin wires that had undergone 0, 1, 2 or 3 rounds of purification, and found that leak reactions due to unincorporated staples were mostly eliminated after the third round (Supplementary Fig. 2.8).

We quantified the kinetics of domino circuits by constructing detailed computational models and parameterizing them using experimental data (Supplementary Figures not shown here, Supplementary Section 2.10.11). Interactions involving a diffusible molecule and a tethered hairpin were modeled as bimolecular reactions according to mass action kinetics, while interactions between two complexes tethered to the same origami were converted to unimolecular reactions by scaling with a *local concentration*[105, 106, 70]. We used parameter inference techniques to establish a maximum likelihood parameter set (Supplementary Figure not shown here) . By ensuring that equivalent interactions in different circuits were parameterized with the same rate constants, we were able to demonstrate consistency in the quantitative behavior of our circuits. In this way, models were used throughout this study for the design and optimization of circuit behavior.

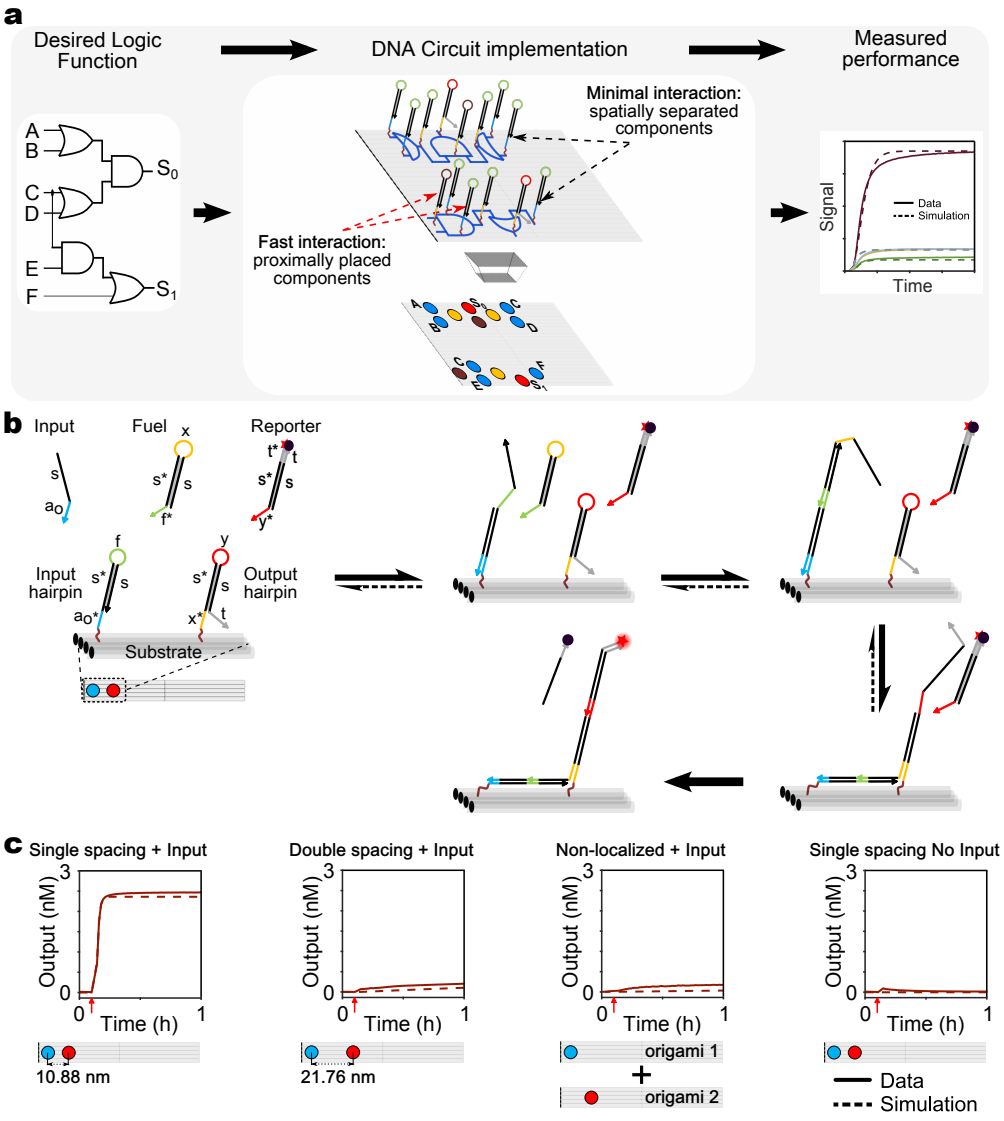

Figure 2.1: Spatial organization controls signal propagation. **a,** High-level abstraction of the circuit design process: An abstract logic circuit (left) is realized using DNA hairpin components arranged on a DNA origami (middle), tested experimentally and compared with model simulation (right). A top view of the localized circuit on origami (middle bottom panel) shows the four basic hairpins reused throughout all circuits in this paper as color-coded circles (Input hairpin (HP): blue; Intermediate hairpin: yellow; Output hairpin: red; Threshold hairpin: brown). **b,** Reaction mechanism for a two hairpin domino (2HP) wire. Arrows denote 3′-ends. Functional domains are indicated by color and labeled in the first panel (s: stem domain; a_0, x, f, y, t: toehold domains; s* represents a domain complementary to s). **c,** Unquenched fluorophore concentration plots (solid lines) and corresponding simulations (dashed lines) demonstrating signal transfer across localized and non-localized versions of a 2HP wire. **Left to Right:** Single-spaced 2HP wire; double-spaced 2HP wire; Input hairpin and Output hairpin on different origami; single-spaced 2HP wire without Input. Reactions were carried out at 25°C with 5 nM Origami, 40 nM Reporter, 100 nM Fuel, 50 nM Input in 1X TAE, 12.5 mM Mg^{++}. Red arrows indicate time points when input strands were added.

2.4 Signal propagation through molecular wires

We created wires of varying lengths and orientations (Supplementary Fig. 2.6 and Fig. 2.14) to allow signal propagation over extended distances, by using Intermediate hairpins (Supplementary Fig. 2.15) as signal relaying components. Multiple identical Intermediate hairpins were positioned at appropriate distances (single spacing) to relay the signal from an Input to an Output hairpin. A schematic of an untriggered eight hairpin domino wire is shown in Fig. 2.2a. We experimentally observed fast and reliable signal propagation through wires with up to 8 hairpins (spanning over 80 nm) along the origami helical axis ($t_{1/2} < 10$ mins.; Fig. 2.2b), with up to 4 hairpins perpendicular to this axis ($t_{1/2} < 6$ mins.; Fig. 2.2c), and with up to 7 hairpins through a 180 degree turn ($t_{1/2} < 10$ mins.; Fig. 2.2d). We observed significantly reduced signal propagation whenever an Intermediate hairpin was intentionally omitted, and found that signals propagated preferentially via neighbouring hairpins (Supplementary Fig. 2.16). Signal completion levels varied approximately inversely with track length (Supplementary Fig. 2.17, Fig. 2.18), likely due to imperfect incorporation of hairpins into the origami (Supplementary Figure not shown here). The non-monotonic decrease in signal can be explained by position-dependent hairpin incorporation efficiency (Supplementary Fig. 2.19). Signal production due to inter-origami interactions increased with the number of hairpins, but even for an eight-hairpin wire was considerably lower than signal production through localized interactions. As noted previously, lowering the origami concentrations significantly reduced inter-origami interactions, with minimal effect on the speed of localized signal propagation (Supplementary Fig. 2.12, 2.13, 2.20, 2.21).

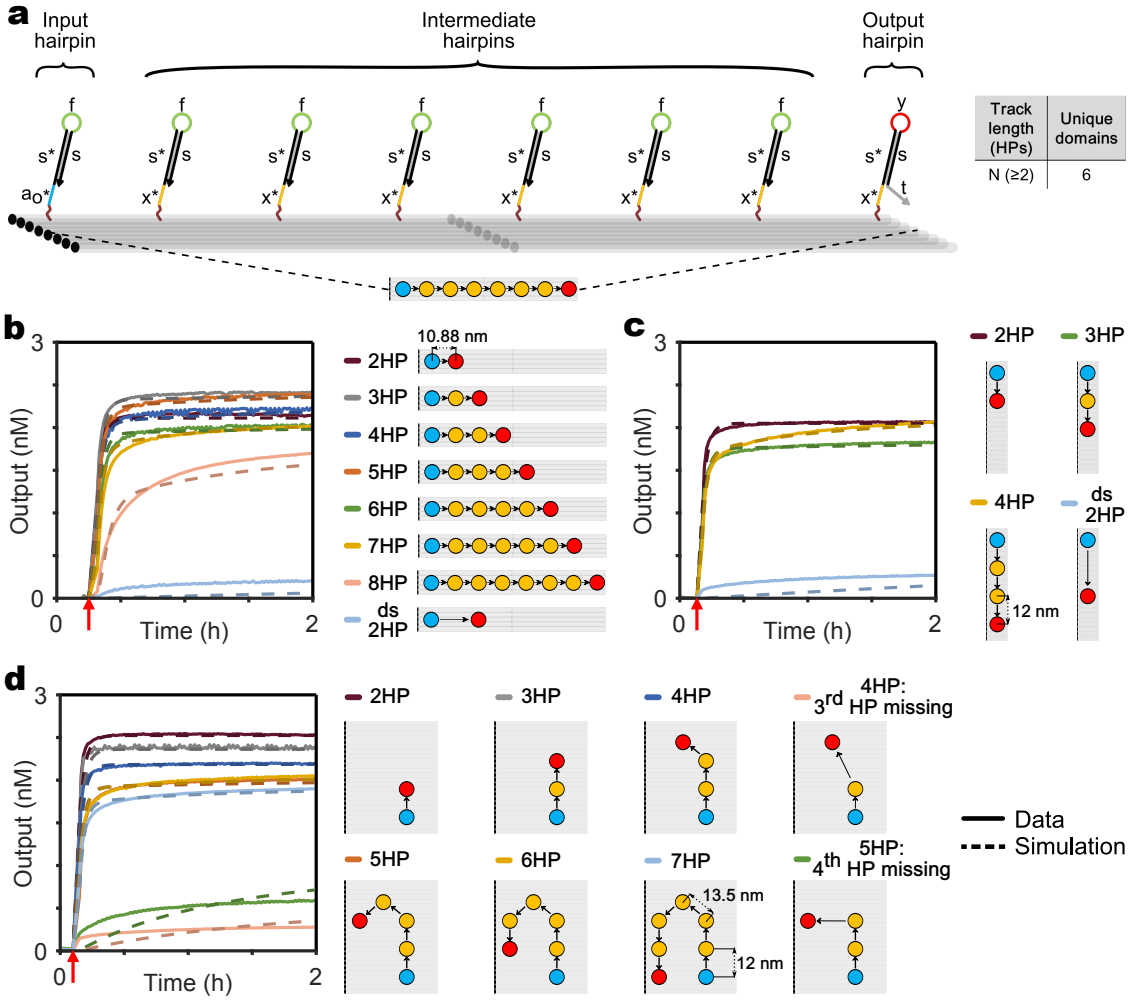

Figure 2.2: Signals propagate along wires of different lengths and orientations. **a,** Schematic representation of an untriggered eight hairpin (8HP) wire along the DNA origami helical axis (domains are labeled with lowercase letters). **Bottom panel:** Top view of the wire with Input hairpin (blue circle), six identical Intermediate hairpins (yellow circles) and Output hairpin (red circle). **Table:** Wires of arbitrary lengths can be built with only six unique domains. **b-d,** Signal propagation along the helical axis (b; 2-8 HP), perpendicular to the helical axis (c; 2-4 HP), and through a 180 degree turn (d; 2-7 HP). **Left:** Unquenched fluorophore concentration plots (solid lines) and simulations (dashed lines). Reactions were carried out at 25°C with 5 nM Origami, 40 nM Reporter, 200 nM Fuel, 50 nM Input in 1X TAE, 12.5 mM Mg^{++}. **Right:** Graphical depiction of all different wires. Hairpin spacing is consistent along the vertical (12 nm), horizontal (10.88 nm) and diagonal (13.5 nm) directions. Black arrows indicate the sequence of signal propagation. Red arrows indicate time points when inputs were added. ds 2HP represents a double-spaced two hairpin wire.

2.5 A wire crossover module

Wires may need to cross at various positions to optimize the spatial layout of localized circuits. A wire crossover module (Fig. 2.3a) is implemented by using orthogonal toehold and hairpin loop sequences for the two different wires at the junction (Fig. 2.3b). Specifically, toehold and hairpin loop sequences in one of the crossing wires are temporarily translated to avoid interference. The translation is initiated by using a different hairpin loop sequence in the hairpin before the junction (Input hairpin of B track, Fig. 2.3b). The translated signal then proceeds across the junction before being reverted to its original form in the hairpin loop of the Intermediate hairpin following the junction (4th hairpin of the B track, Fig. 2.3b). Since the orthogonal toehold and hairpin loop domains are used only at the crossover junctions, they can be reused in all crossovers in a localized circuit, promoting simplicity in circuit design. Experimentally, minimal output signal was observed through the participating wires in absence of the corresponding Inputs, but upon addition of both the Inputs, both the signals successfully crossed over each other at the junction (Fig. 2.3c,d). We also found that the dynamics of each wire of the crossover circuit were consistent with our parameterized model (Fig. 2.3d, Supplementary Figure not shown here).

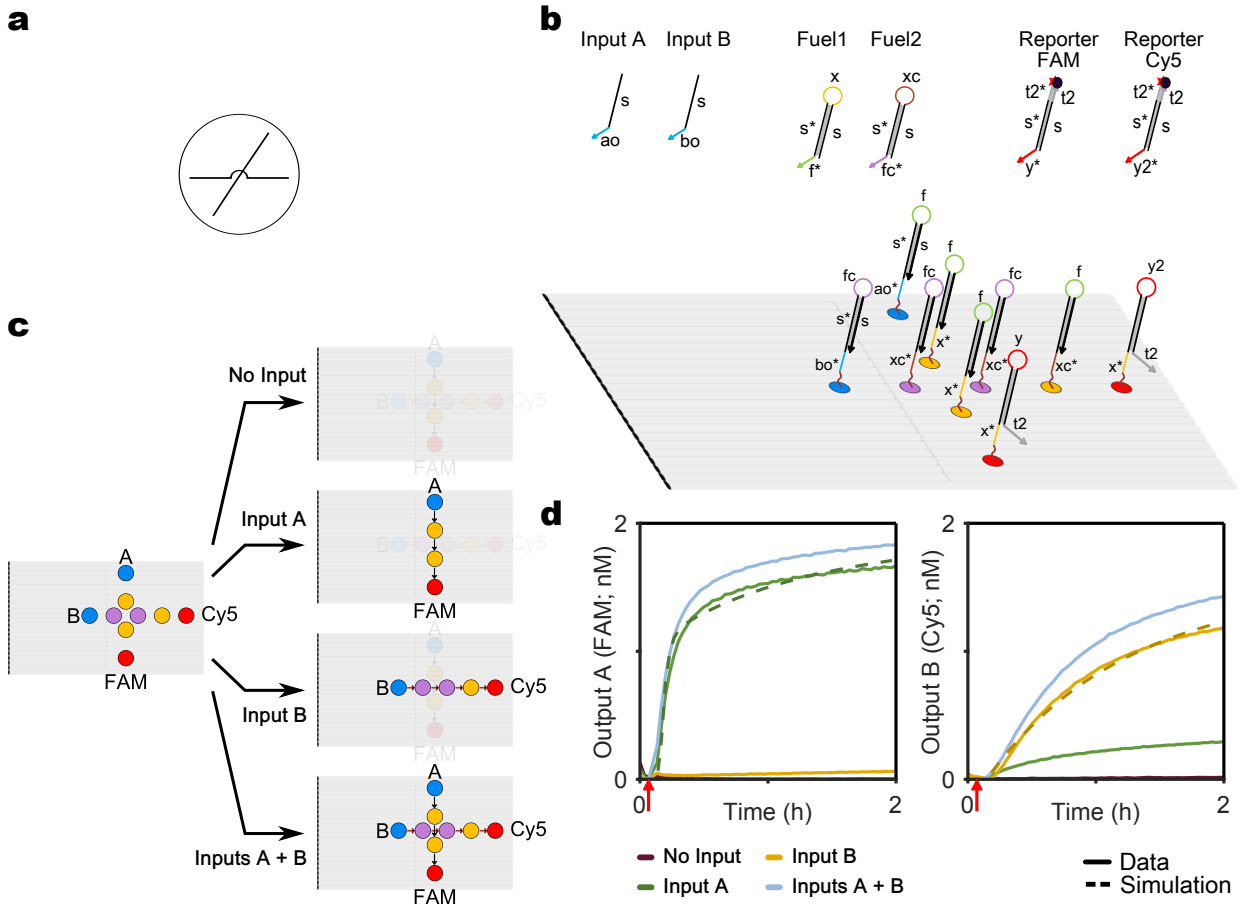

Figure 2.3: Design and implementation of a wire crossover. **a** Wire crossover diagram. **b** Domain-level representation of a wire crossover. Functional domains are indicated by color and labeled with lowercase letters. The two wires use orthogonal toeholds (x*, xc*) and hairpin loop domains (f, fc) at the junction. Matching fuel species are used for each orthogonal wire. **c** Schematic representation of signal transmission for different Input combinations. Input A and Input B trigger wires that activate spectrally distinct reporters, FAM and Cy5, respectively. **d** Signal transfer through wire crossover leading to downstream activation of Reporter FAM (left plot) and Reporter Cy5 (right plot). Colors of the graphs correspond to different cases of Input addition as described in the legend. Reactions were carried out at 25°C with 5 nM Origami, 20 nM Reporter(s), 100 nM Fuel(s), 50 nM Input(s) in 1X TAE, 12.5 mM Mg^{++}. Red arrows indicate when Inputs were added.

2.6 Design and construction of elementary logic gates

As a prerequisite for performing arbitrary logic computation with our domino architecture, we next designed two-input OR and AND gates. The two-input OR domino gate was implemented through a wire fan-in by positioning an Output hairpin close to two orthogonal Input hairpins on the origami (Fig. 2.4a). Because all hairpin components were constrained to have the same stem, input orthogonality was ensured by using distinct toehold sequences. Experimentally, no significant output fluorescence was observed in absence of both Inputs, but addition of either one or both Inputs resulted in high output fluorescence, consistent with OR logic ($t_{1/2} < 5$ mins).

To implement a two-input AND domino gate, we used a thresholding strategy to prevent signal propagation when only one of the inputs is present. Specifically, a "Threshold hairpin" was designed to block signal propagation by outcompeting the Output hairpin. We ensured preferential binding to the Threshold hairpin by shortening the Output hairpin toehold, while keeping the Threshold hairpin toehold at 6 nucleotides (Fig. 2.4b and Supplementary Fig. 2.22). Once the Threshold hairpin is opened, it captures a partially double-stranded "Threshold block", making signal inhibition practically irreversible. Experimentally, the extent of preferential binding to the Threshold hairpin depended on the difference in toehold lengths (Fig. 2.4b), where a 3 nucleotide Output hairpin toehold was found to be optimal. Consequently, all domino logic circuits presented in this study, including the OR gate discussed above, were constructed using Input and Threshold hairpins with 6 nucleotide toeholds, and Intermediate and Output hairpins with 3 nucleotide toeholds.

The two-input AND domino gate was implemented by combining an OR gate with a Threshold hairpin. The Output and Threshold hairpins were positioned at equal distances to two orthogonal Input hairpins (Fig. 2.4c). When only one of the input strands is added,

the Threshold hairpin blocks signal propagation, resulting in low output fluorescence. When both input strands are added, the signal from one of the inputs is blocked, while the signal from the other input successfully propagates to the Output hairpin and generates high output fluorescence ($t_{1/2} < 6$ mins.), consistent with two-input AND logic.

The measurements of the two-input OR, threshold and two-input AND gates were included in the parametrization of our computational models. Kinetic parameters for input and fuel binding were shared between all circuits. However, we used distinct local concentration parameters for the wires and logic circuits, since the spacing between hairpins was slightly different in these two settings. The ratio between the binding rates of the Threshold and the Output hairpin was also calibrated to the experimental data, and was approximately 10 to 1 (Supplementary Figure not shown here). The simulated model behaviors were consistent with the measured kinetics for the two-input OR, threshold and two-input AND gates (Fig. 2.4 and Supplementary Figure not shown here).

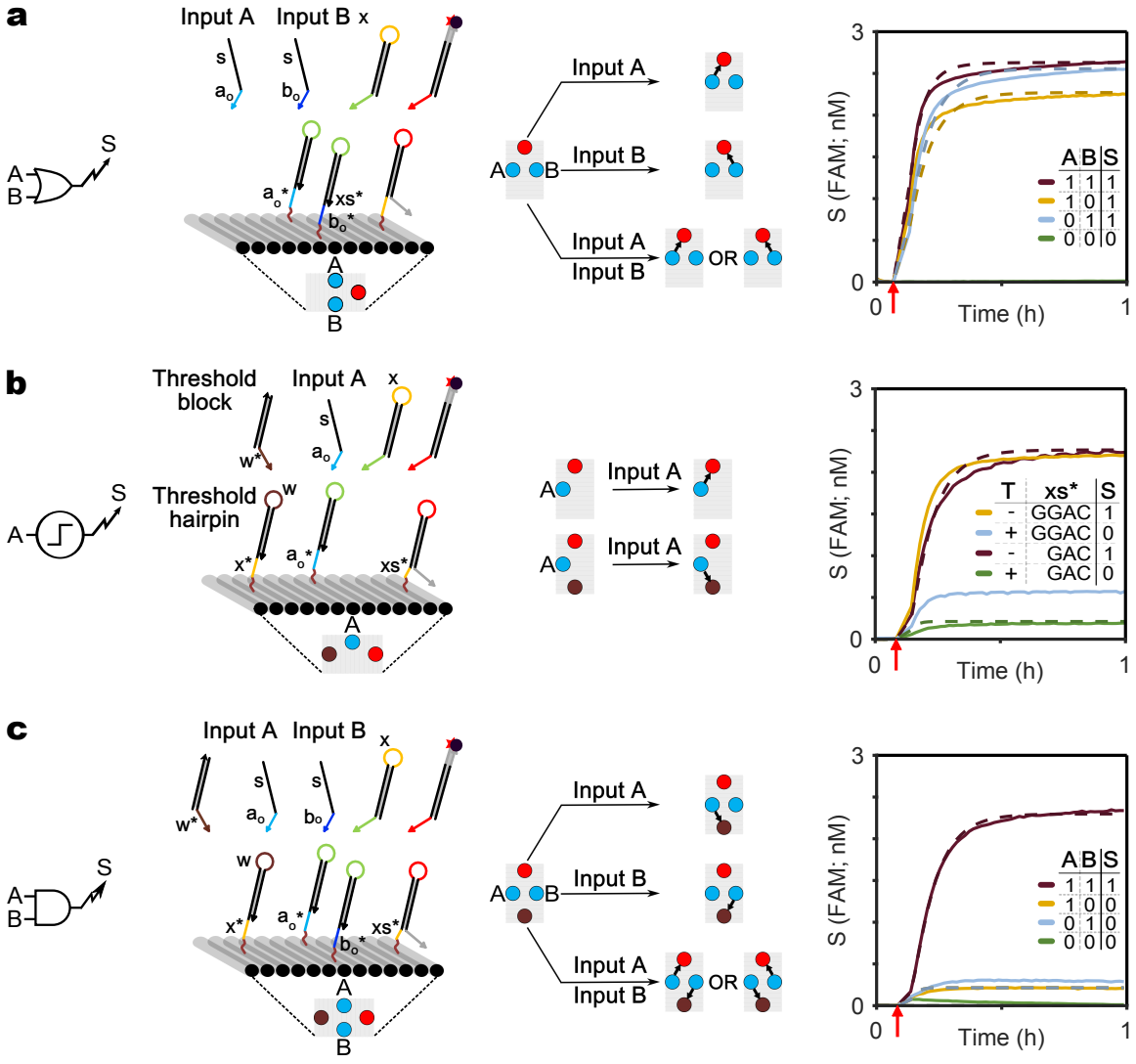

Figure 2.4: Elementary logic gates are realized with localized DNA hairpins. a, Two-input OR; **b,** Thresholding module; **c,** Two-input AND. **For (a-c), left:** Logic gate diagram. **second-to-left:** DNA domino representation and top view projection. All domains are labeled with lowercase letters and Inputs are distinguished by their toeholds (a_0 and b_0, blue). The output toehold domain xs* (yellow, 3 or 4nt) is a truncated version of x* (6nt). **second-to-right:** Graphical summary of circuit operation. For OR and AND gates, the response to different input combinations is depicted. For the threshold module, a circuit with a Threshold hairpin is compared to a circuit without it. Black arrows indicate the (most likely) direction of signal propagation. **right:** Unquenched fluorophore concentration plots (solid lines) and simulations (dashed lines). For AND and OR gates, legends are represented as truth tables, where presence of an input strand (A,B) or output signal (S) is denoted by "1" and their absence is denoted by "0". For the Threshold module, the T column indicates whether the system did (+) or did not (-) include the Threshold hairpin, which contains the x* domain (CTGGAC). The xs* column indicates whether the Output hairpin has a 3nt (GAC) or 4nt (GGAC) toehold. Experimental conditions were as in Fig. 2.1. Red arrows indicate when inputs were added.

2.7 Modular cascading of logic gates to build complex logic circuits

To demonstrate modular circuit design using our domino architecture, we built a three-input AND gate by cascading a pair of two-input AND gates on the same origami. Specifically, we replaced the Output hairpin of an upstream two-input AND gate with an Intermediate hairpin, such that the output of the first gate was relayed to the input of the second (Fig. 5a and Supplementary Figure not shown here). Upon addition of any combination of two input strands, the circuit showed low output fluorescence. When all three input strands were added there was high output fluorescence ($t_{1/2} < 6$ mins.), consistent with three-input AND logic. Furthermore, the experimental data exhibited the expected Boolean logic. We were able to quantitatively predict the dynamics of the three-input AND gate through model simulation, using the parameters obtained from our previously characterized circuits (Fig. 5a).

Next, we positioned two distinct three-input AND gates side by side and triggered them simultaneously, to determine whether multiple circuits on the same origami can function concurrently (Fig. 5b). Both gates used the same Intermediate and Threshold hairpins throughout, along with the universal Fuel, but used distinct toeholds for the Input and Output hairpins to ensure orthogonality. Experimental measurements were consistent with model predictions (Fig. 5b).

To further demonstrate scalability, we constructed a six-input AND gate by connecting the outputs of both three-input AND gates, using an additional two-input AND gate (Fig. 5c and Supplementary Figure not shown here). When all six inputs were added the circuit produced high output signal ($t_{1/2} \sim$12 mins.). Conversely, the circuit produced low output for any combination of five or fewer inputs. While the number of hairpins increased from four for the two-input AND gate, to eighteen for the six-input AND gate, all hairpins used the same conserved set of only five domains, plus a separate domain for each

input and output. Similar to our experiments on wires, we observed attenuation of the output signal with increasing number of hairpins (Supplementary Fig. 2.18). This signal loss can in part be explained with a model assuming a fixed non-zero probability of hairpin omission (Supplementary Figure not shown here). Assuming a hairpin incorporation efficiency of 83% results in the best fit of our model for the logic circuits data, while a fit to the wire data suggests an efficiency of 93%. Our estimates are broadly consistent with a previous experimental study reporting an 87.5% average staple incorporation efficiency in a single-layer origami[67].

To exemplify arbitrary Boolean logic computation using our domino architecture, we built a two-input dual-rail XNOR gate (Fig. 5d and Supplementary Figure not shown here). Dual-rail encoding allows an arbitrary Boolean logic function to be realized using only a combination of AND and OR gates, avoiding the need for NOT gates, which are difficult to implement experimentally[39]. Each input variable A is specified as TRUE by a dedicated signal strand A1, and specified as FALSE by a distinct signal strand A0 (Fig. 5d). Only one of the two strands is present at any given time. Accordingly, our dual rail XNOR gate was implemented as a pair of parallel circuits, computing TRUE and FALSE outputs separately. The complete circuit arranged seventeen hairpins into six two-input AND and OR gates. The experimental data showed signal propagation ($t_{1/2} < 8$ mins.) consistent with predictions from the computational model.

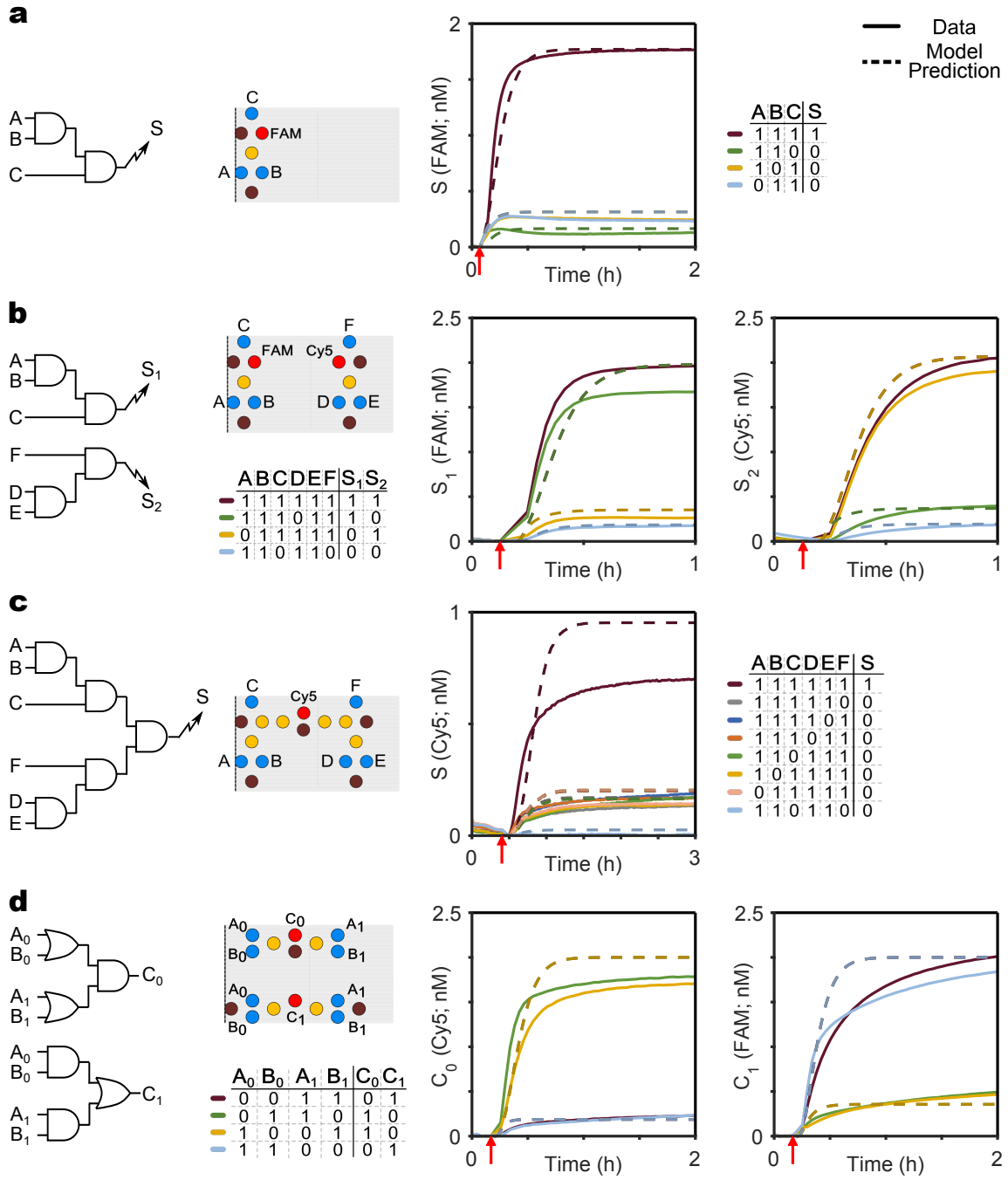

Figure 2.5: Elementary logic gates are combined into multi-input logic circuits. **a,** Three-input AND gate. **b,** Two three-input AND gates in parallel. Spectrally distinct reporters are used to measure the output of the two gates simultaneously. **c,** Six-input AND gate. **d,** Two-input dual-rail XNOR gate. **left:** Logic circuit diagram. **middle:** Top view of the localized DNA circuit. **right:** Unquenched fluorophore concentration plots (solid lines) and model predictions (dashed lines). Legends are represented as truth tables, where presence of an input or Output is denoted by "1" and their absence is denoted by "0". Reactions were carried out at 25°C with 5 nM Origami, 40 nM Reporter(s), 200 nM Fuel, 50 nM Input(s) in 1X TAE, 12.5 mM Mg^{++}. Red arrows indicate when inputs were added.

2.8 Discussion

Overall, the number of unique sequences required for building any complex domino circuit did not depend on the number of constituent gates, but only on the number of inputs and outputs. Moreover if wire crossovers are required, the same crossover toehold and hairpin sequences can be reused for any number of crossover points. Our domino circuits also performed significantly faster than previous systems with diffusible components (Supplementary Table 2.1). For example, a three-input AND domino gate had a half time of 7 min with operating concentration of only 2 nM, compared to 4 hours for an equivalent circuit with diffusible components operated at 100 nM concentration [39].

The modularity of our design approach enabled us to construct a family of cascaded circuits spanning an entire rectangular tile origami. Even larger and more complex circuit designs could be made with bigger and multilayered stiffer origami scaffolds, however three issues would need to be addressed. First, inputs are currently distinguished only by their toehold domains, and in practice the number of sufficiently orthogonal six nucleotide toeholds is small. This limitation can be overcome by incorporating an additional recognition domain in the Input hairpin, to encode input specificity (Supplementary Figure not shown here). Second, we observed signal attenuation with increasing circuit size, likely due to imperfect hairpin incorporation. Such imperfections will become less limiting with continuing improvements in origami assembly protocols. Alternatively, component redundancy could be used to compensate for assembly defects, and signal restoration modules (e.g. a threshold coupled with an amplification step [39]) could be used to restore the signals at the ensemble level once the localized computation has completed. Third, although inter-origami interactions are not currently limiting, they could become significant as circuit size increases. Such interactions could be reduced by using a low concentration of logic-processing origami, followed by a global signal amplification of

the ensemble output. More generally, inter-origami interactions can be further reduced by using immobilizing techniques to tether origami molecules to a surface, or by using closed 3-dimensional origamis with components tethered to the inner faces.

Circuit architectures with localized components may provide a path towards the delivery of DNA circuits to cells, a long-held ambition of dynamic DNA nanotechnology that only recently started to become reality[1, 107, 20]. Not only do localized circuits enable control of stoichiometry during delivery, but increased speed compared to non-localized circuits may be even more pronounced in the densely packed cellular environment. Moreover, localized circuits could be used to increase the complexity of chemical synthesis reactions achievable with DNA-templated chemistry[108, 109] or to enhance the specificity of theranostic DNA robots[10].

2.9 Materials and Methods

2.9.1 Component design

All the hairpins used in this study were designed with a 12 nucleotide stem to provide meta-stability while preventing any unnecessary loss of speed and chemical potential due to branch migration through longer domains. The toehold domains were also chosen to be 6 nucleotide long for optimal strand displacement speed. The domino wires were built with three basic components: Input hairpin, Intermediate hairpin and Output hairpin. In addition, the freely floating components: Input strand, Fuel complex and Reporter complex interacted with the localized components to propagate the signal (Fig. 2.1b). For designing a wire of any length, five unique 6 nucleotide domains (a_0, f, x, y, t) and one 12 nucleotide long domain (s) were designed. All the circuit components use a combination of these six domains as specified in Fig. 2.1b. For the signal cross-over, orthogonal 6 nucleotide sequences (xc,fc) were allocated to the toehold and hairpin loop domains of

participating hairpins as described previously. For designing the 2-Input AND domino gate, one more domain (w) was required for the hairpin loop of Threshold hairpin. The Reporter complex was designed to have an 18 nucleotide long double stranded stem to aid towards its stability at 25°C. Accordingly the Output hairpin was designed to have 6 nucleotide 3′-flanking domain (t). For designing logic circuits with multiple inputs and outputs, Input hairpins with orthogonal 5′-toehold domains (a_0,b_0,c_0,d_0,e_0,f_0) and Output hairpins with orthogonal hairpin loops (y, y2) were designed. The 3′-flanking domains (grey domains) in the Output hairpins were different for the wires (t) and logic circuits (t2). All the other components in the logic circuits were similar to those used for signal transmission lines. For each localized hairpin at a particular position on the origami, the sequence of the origami staple with its 3′-end at that position was extended with the sequence of corresponding hairpin along its 3′-end by a 5 nucleotide polyT linker. The linkers provided conformational flexibility to the hairpins, thus aiding signal propagation on the origami scaffold.

2.9.2 Sequence selection

NUPACK [110] was used to generate a set of orthogonal 6 nucleotide toeholds and 12 nucleotide stem domains. No more than 3 G's, C's, A's or T's were allowed consecutively and the ensemble defect was set to 1 percent. For different circuits, corresponding number of domains were selected from the master pool to generate individual component sequences. These sequences were then verified by NUPACK to detect possible non-intended interactions and the domains were further optimized if any significant interaction was detected.

2.9.3 Preparation of a localized circuit

We used a twist-corrected version of the rectangular tile origami[46] as a scaffold for our study. Twist-correction by base deletion at every third turn on the helical axes has been shown to reduce global twist, thus providing greater predictability in circuit design and improved assembly. We didn't add any edge staples to prevent origami edge stacking while annealing [46]. For origami preparation, standard desalted DNA staple strands were batch ordered in 96 well plates at stock concentrations of 400 μM in RNase-free water from Integrated DNA Technologies (IDT) and m13mp18 single stranded template DNA was ordered from Bayou Biolabs. Modified staple strands with component hairpin sequences at the 3'-end, Fuel complex, Input strands, and Fluorophore-labeled and quencher labeled strands for different Reporter complexes were ordered with HPLC purification from IDT. In addition, for each Output hairpin, an Output opening strand (OOS): complementary to the 5'-toehold and the adjacent stem domain; and for each Reporter complex, a Reporter opening strand (PO): complementary to the fluorophore-labeled strand, was ordered with HPLC purification from IDT and the lyophilized samples were re-suspended with Tris-EDTA buffer (TE: Nuclease free, pH 8.0) to stock concentrations of 100 μM and stored at -20°C. Diluted aliquots were further prepared for each of the hairpin staples, the corresponding unmodified staples and other strands as and when needed for regular use, and were stored temporarily at 4°C. Three master layouts were prepared with the origami scaffold: one for the wires (Supplementary Information Fig. 2.6a), one for the logic circuits (excluding dual rail XNOR) (Supplementary Information Fig. 2.6b), and one for the dual rail two-input XNOR circuit (Supplementary Information Fig. 2.6c). All the circuit operations explained in the study were performed using subsets of these three blueprints. For each blueprint, 4 μM master stocks (one each for top half and bottom half of the origami) of staples were prepared excluding the sta-

ples in the blueprint. For preparing a specific wire or logic gate , 1X m13mp18 template DNA was mixed with 5X of the staple master stocks, 10X of the corresponding modified staples with hairpins and 10X of unmodified staples for the rest of the sites for that blueprint. These components were combined in Tris-Acetate EDTA buffer with 12.5 mM Mg^{++} (1X TAE/Mg^{++}: 40 mM Tris base, 20 mM acetic acid, 2 mM EDTA and 12.5 mM magnesium acetate, adjusted to pH 8.0); 1X = 60 nM. The reaction mix was then annealed by incubation at 95°C for 2 minutes, slow cooling to 60°C at 0.1°C every 12 seconds, incubation at 60°C for 12 minutes, slow cooling to 25°C at 0.1°C every 12 seconds, and hold at 4°C for up to 24 hours (Annealing Protocol 1). Stock solutions of 10 μM Fuel complex was prepared in 1X TAE/Mg^{++} and was annealed by heating it to 95°C for 2 minutes and slowly cooling to room temperature at 0.1°C every 6 seconds (Annealing Protocol 2). The Reporter complexes were annealed following Annealing Protocol 2 after mixing fluorophore-labeled strand and quencher-labeled strand at molar ratios of 1:1.2 in 1X TAE/Mg^{++}.

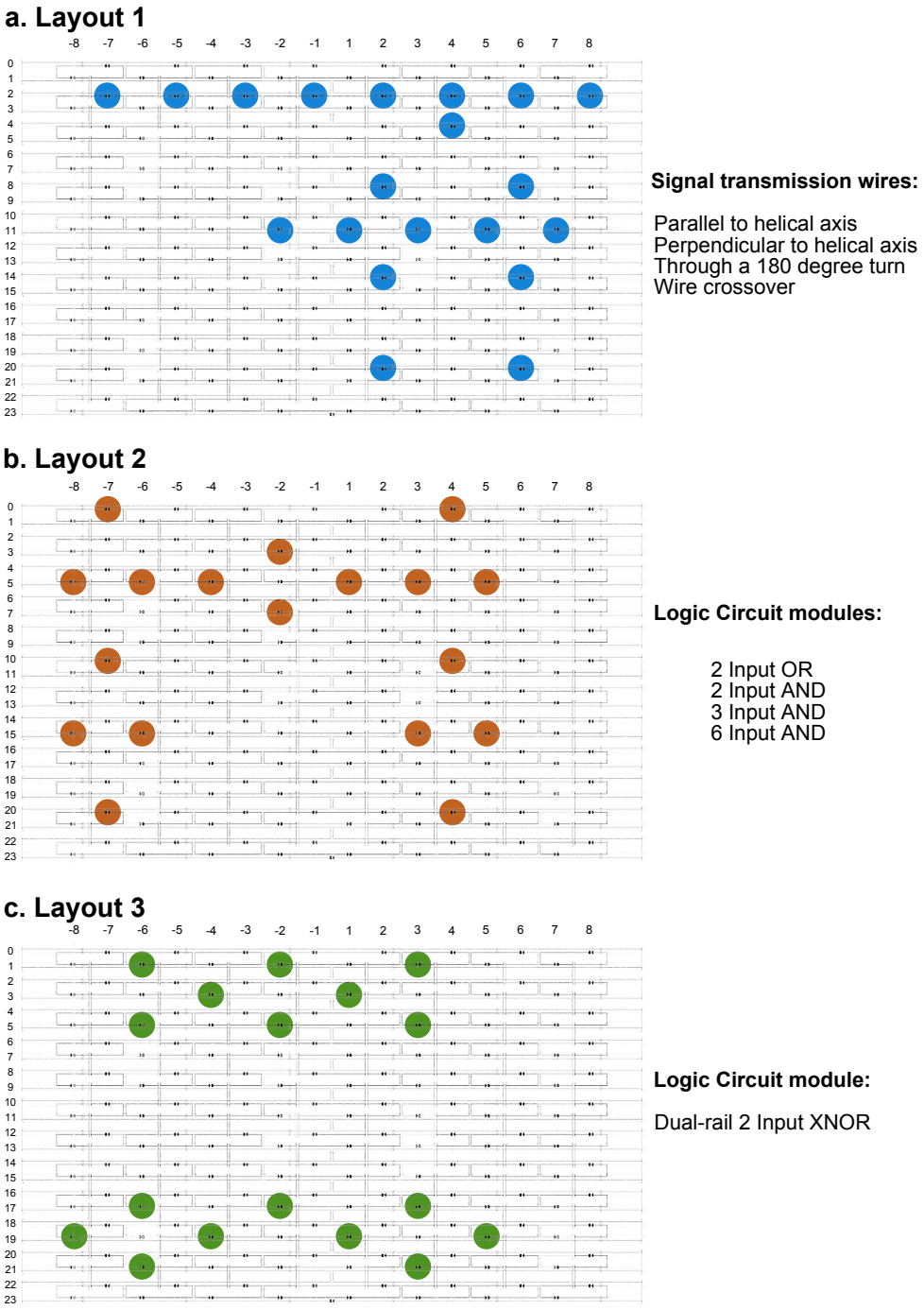

Figure 2.6: Layouts for different circuits on the origami scaffold. Staple modification sites on the origami scaffold are indicated in color The different circuits built on each layout are indicated on the right. The row and column annotation used to describe the modification sites at the 3′-end of the staples are mentioned on the left and top of the origami schematic diagrams respectively. A modification site is named as "R(row_value)C(column_value)": for example, the leftmost modification site of Layout 1 is "R2C-7". The staple strand which has its 3′-end at that site was called "R2C-7" staple.

2.9.4 Purification of circuit components

Annealed origamis were purified to remove excess staple strands through size exclusion chromatography using Sephacryl S300-HR resin (GE Healthcare Life Sciences). The Sephacryl S300-HR resin is commercially pre-equilibrated in 20% ethanol. Aliquots of Sephacryl S300-HR were collected in 50 ml falcon tubes and centrifuged at 1000 g for 5 minutes in 4°C. The supernatants containing ethanol were discarded and the resin pellets were equilibrated three times with distilled water and three times with 1X TAE/Mg^{++} by re-suspending the pellets with solvents to 50 ml by shaking, centrifugation at 1000 g for 5 minutes in 4°C, and discarding the supernatants. After the supernatants were discarded in the final round, the resin pellets were re-suspended with equal volumes of 1X TAE/Mg^{++} and stored at 4°C. For preparing each size-exclusion column, 500 μl of re-suspended resin was added to 0.8 ml Micro Bio-Spin^{TM} Chromatography column (Bio-Rad Laboratories) with collection tube and centrifuged at 1000 g for 5 minutes in room temperature. The flow-through was discarded and an additional 500 μl of resin was added to the column before another centrifugation at 1000 g for 5 minutes at room temperature. Three such columns were prepared for purification of up to 50 μl of each origami construct. The resultant columns were placed on fresh sterile 1.7 ml Eppendorf tubes and up to 50 μl of annealed origami was loaded on each column for the 1^{st} round of purification. Each column was centrifuged at 1000 g for 5 minutes at room temperature, and the flow-through was collected and loaded onto a fresh column for the 2^{nd} round of centrifugation. After repeating the process through a 3^{rd} round, the flow-through for each origami sample was collected for experiments. Supplementary Information Fig. 2.7 shows a 1% Agarose Gel analysis demonstrating the efficiency of the purification protocol. We observe minimal loss of origami with almost complete purification of any excess staples after three rounds of purification. For the domino wires, the annealed Reporter

complex was further run through 10% Polyacrylamide gel electrophoresis (PAGE) with 12% glycerol as loading agent, to remove the excess quencher-labeled strand. The band corresponding to the full Reporter Complex was visualized using black light and cut out and suspended in 1X TAE/Mg^{++} for 24 hours at room temperature. The resultant solvent was extracted and stored at 4°C for kinetics experiments.

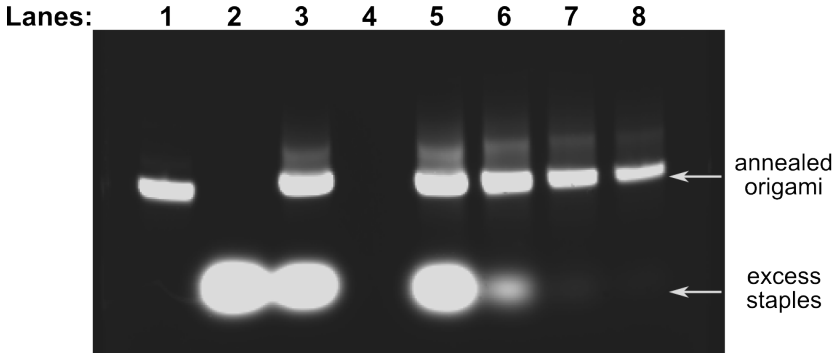

Figure 2.7: Origami purification efficiency with Sephacryl S300-HR resin. Grayscale image of 1% Agarose gel stained with SyBr Gold; **Lane 1:** m13mp18 template DNA (1X); **Lane 2:** Origami staple stock mix (5X); **Lane 3 and 5:** Annealed unpurified origami (1X); Lane 6: Origami after 1^{st} round of purification (1X); **Lane 7:** Origami after 2^{nd} round of purification (0.9X); **Lane 8:** Origami after 3^{rd} round of purification (0.81X). 1X = 50 nM; 5 μl of the samples at mentioned concentrations were added to each well.

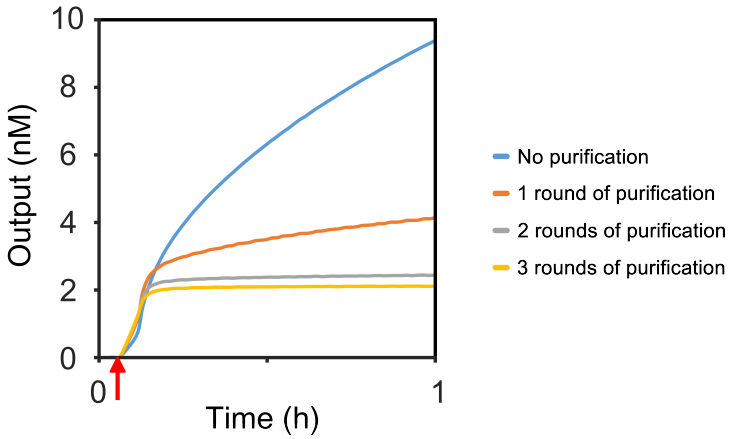

Figure 2.8: Signal transmission through purified vs. unpurified two hairpin wire. Unquenched fluorophore concentrations reflecting signal transfer across a two hairpin wire parallel to the helical axis of the origami, at different stages of the purification process after annealing. Plots of different colors correspond to wires which were triggered either without any purification (blue), or after subjecting through 1 (orange), 2 (gray) and 3 (yellow) rounds of bead purification as described in the Methods section. Reactions were carried out at 25°C with 5 nM origami, 40 nM Reporter, 200 nM Fuel, 50 nM Input in 1X TAE/Mg^{++}. Red arrow indicates time point when input strands were added.

2.9.5 Fluorescence kinetics experiments

Kinetics experiments were performed on a spectrofluorometer (Horiba Scientific: Fluorolog®-3 and FluoroMax®-4) with 0.875 ml Fluorometer Micro Square Cells with polytetrafluoroethylene (PTFE) stoppers (Starna: 23-5.45-S0G-5) and cuvette adaptors (Starna: FCA5). A maximum of four samples were tested for each set of measurements using a 5 nm slit width for both excitation and emission monochromators and an integration time of 10 seconds. Excitation and emission wavelengths of different fluorophores used in various experiments were as follows: FAM (495 nm / 520 nm), Cy5 (648 nm / 668 nm). For experiments using a single Reporter, measurements were taken every 60 seconds, while for experiments using two Reporters, measurements were taken every 120 or 150 seconds. Before an experiment, the cuvettes were cleaned by washing 5 times with distilled water, once with 70% ethanol, and another 5 times with distilled water. The excess residual water was dried out of the cuvettes with airflow. Then, generally all the circuit components except the Input strand(s) were mixed and added to the cuvettes and an initial steady state signal for each sample was measured as baseline. After that, the experiment was paused, for addition of Input strand(s) and subsequent mixing by gentle vortex or inverted shaking. The cuvettes were then put back to the fluorometer, before the experiment was resumed. After the completion of data collection for circuit performance, an excess (400 nM) of corresponding Output hairpin opening strand (OOS) was added to trigger the unreacted Output hairpin. The resultant final output signal was representative of the total number of output hairpins and was taken as a close approximation of the total number of origami molecules present in the solution for modeling studies.

2.9.6 Data representation

Arbitrary fluorescence units (S/R values) obtained from the spectrophotometer were first corrected by subtracting the baseline signal values for each sample, as discussed in the previous section. The baseline corrected signal was then converted to the concentrations of the corresponding unquenched fluorophore strands using a calibration curve of each Reporter complex (Fig. 2.10. Because we observed small variations in fluorescence signal between different cuvette positions, calibrations were performed for each position independently. To construct a calibration curve, a pre-determined volume of annealed Reporter complex stock was re-suspended in 1X TAE/Mg^{++}, added to the cuvette and an initial baseline signal was recorded for each cuvette. That was followed by stepwise addition of known concentrations of Reporter triggering (Probe opening: PO) strands. After each trigger strand addition, the increase in signal was recorded till a steady state value was reached. The baseline-corrected signal values were then plotted against the PO strand concentrations to obtain a calibration curve. The signal values were linearly proportional to the fluorophore concentrations and the slope of a linear fit was recorded as the signal-to-concentration "conversion factor" for that cuvette position and Reporter. Supplementary Information Fig. 2.9 shows an example calibration curve for one of the Reporters used in this study. Finally, an excess of PO strand was added to the solution to trigger all the Reporter complexes, and the final increase in signal was divided by the conversion factor to get the actual concentration of the Reporter complex in the solution, and in turn the actual concentration of the Reporter complex stock. Importantly, these conversion factors were used to translate the increase in output signal due to signal propagation through a circuit using the corresponding Reporter complex as output. Fresh calibration curves were constructed on event of a change in external experimental conditions like different cuvettes, new xenon lamp, different batch of Reporter strands, etc. to maintain

accuracy and consistency across different experiments.

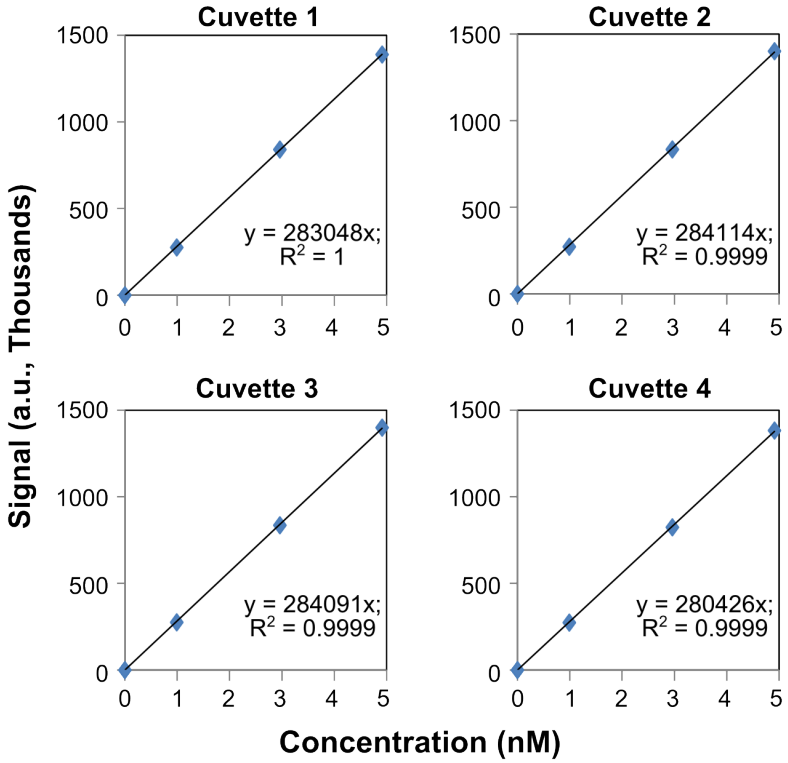

Figure 2.9: Example Calibration plots for Data normalization. The plots represent increase in fluorescent signal (blue square dots) due to unquenching of fluorophores in Reporter complexes upon addition of fixed concentrations of PO strands (1, 3 and 5 nM) for each cuvette. The initial baseline signal of the Reporter complex is used as the reference value for each case (zero signal value). The equations at the Inset represent the linear fits of the dots (with R-squared values) and the slopes of the linear plots are the "Conversion factors" used to convert fluorescence units to concentration values for a specific Reporter in actual experiments.

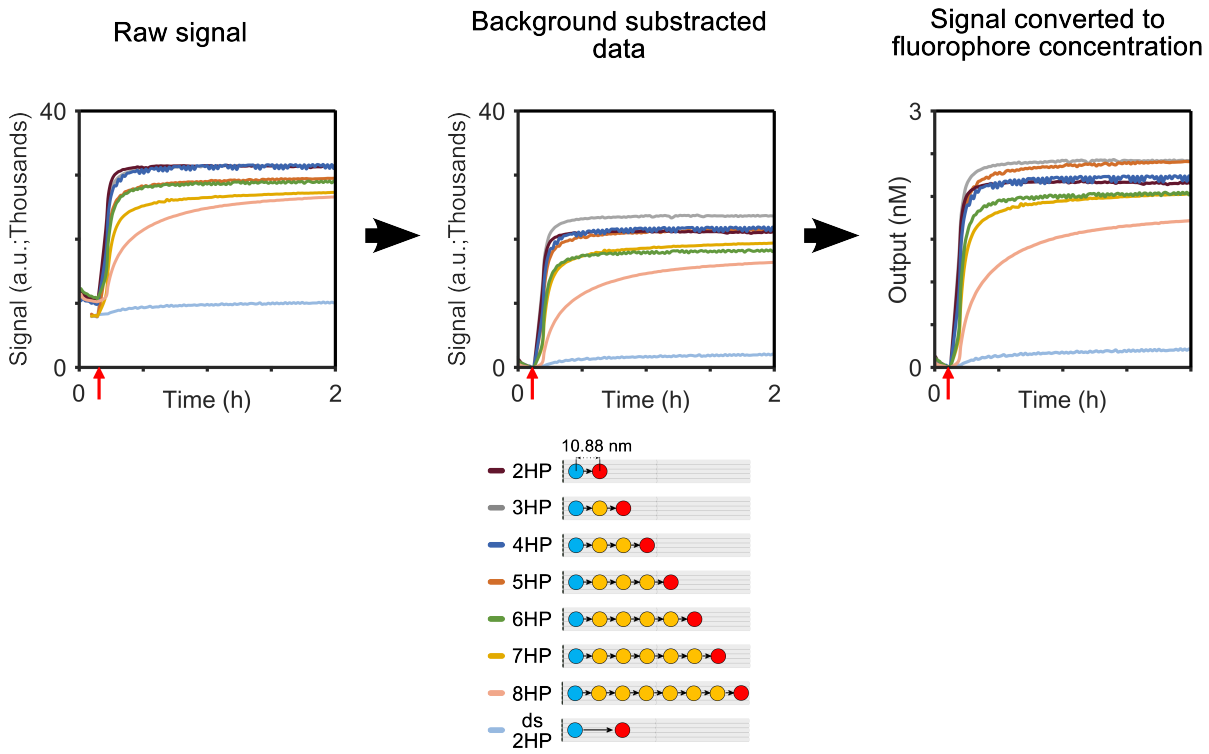

Figure 2.10: Process workflow to convert raw fluorescence signal data to unquenched fluorophore concentration. **(Left)** Plots showing the fluorescence signal values (arbitrary units; a.u.) obtained after triggering signal transmission on two to eight hairpin wires parallel to the origami helical axis with the spectrophotometer; **(Middle)** The baseline corrected plots for the corresponding wires; and **(Right)** The final plots demonstrating signal transmission through these wires with respect to unquenched fluorophore concentrations, as described in the Methods section. The colors of the plot correspond to different wires as schematically represented in the legend.

2.9.7 Agarose and polyacrylamide gel electrophoresis (PAGE).

For analyzing the purification efficiency using Sephacryl S300-HR resin purification method, 1% Agarose gel was prepared by mixing 1 g of Ultrapure TM Agarose (Thermo Fisher Scientific; Catalog#: 16500500) in 100 ml of 1X TAE/Mg^{++}. The solution was then heated to boil and cooled down to 50-60°C to dissolve the Agarose before pouring it to the gel tray to solidify the gel. The solidified gel was placed in the gel tray in a container with ice such that the side and bottom walls of the gel tray are always in contact with ice. Pre-cooled 1X TAE/Mg^{++} was added as running buffer till the gel was completely submerged in the tray. This prevents over-heating of the gel and the buffer and minimizes dissociation of the origamis while running the gel. Origami samples were mixed with appropriate volumes of 80% glycerol to achieve final concentrations of 12% glycerol by volume, which acted as a loading agent. The gel was then run at 100 V for 1 hour and stained with SYBR Gold (Thermo Fisher Scientific; Catalog No.: S11494) for 15 minutes before imaging. Gel Imaging was performed using Typhoon FLA 9000 Gel Imaging Scanner (GE Healthcare Life Sciences) at 50 μm resolution using the SYBR Gold Nucleic Acid stain filter settings. For purifying the Reporter complex used in signal transmission experiments with wires, 10% Polyacrylamide gel was prepared by mixing 5 ml 19:1 40% acrylamide/bis, 2 ml 10X TBE/Mg^{++}, and deionized water to 20 ml. Then 150 μl APS and 15 μl TEMED were added to accelerate the polymerization of acrylamide. Annealed Reporter complexes were mixed with 80% Glycerol to achieve final concentrations of 12% glycerol by volume and loaded to the wells of the gel (upto 60 μl of sample per well). PAGE gels were run in 1X TBE/Mg^{++} at 120 V for 40 minutes to separate the excess quencher-labeled strands from the annealed Reporter complexes and then the Reporter complexes were extracted as described before.

2.10 Supplementary information

2.10.1 Spacing between hairpins on origami

The relative distances between adjacent hairpins and positions of circuit components on the origami scaffold were optimized based on the underlying hairpin design with 12 nucleotide stem and 6 nucleotide long toeholds and hairpin loops. The twist-corrected rectangular tile origami scaffold has staple endings pointing upward from the origami surface at every three helical turns, i.e. every 32 bases (˜10.88 nm) along a helix. Sites are spatially shifted by 1.5 helical turns between adjacent rows. For a two hairpin wire, the semi-stiff DNA polymer formed after interaction between Input, Input hairpin and a Fuel complex consisted of a 36 base pair long nicked double stranded region (˜12.24 nm) followed by a toehold used for binding to the Output toehold. We performed molecular dynamics simulations observing 60,000 steps using the oxDNA2 model [111, 112] with salt concentration [Na+] = 1.0 M at 25°C. For each configuration, we calculated the relative distances between the first and the last nucleotide of the double stranded region, and the nucleotides in the exposed hairpin loop domain of the Fuel. Fig. 2.11 shows histogram plots demonstrating the results. For constructing domino wires along the helical axes, we chose staple modification sites every 32 bases apart (˜10.88 nm), which falls under the interaction range as seen by the oxDNA simulations. Similarly, perpendicular to the helical axes we found that the most optimal separation distances between staple modification sites were 6 helices apart (˜12 nm considering no gap between helices, as the repulsive forces between helices may be significantly stabilized by divalent magnesium ions in solution; or ˜16.2 nm, if we consider 0.7 nm inter-helical gaps). For constructing the domino wire with a 180 degree turn, we chose staple modification sites at ˜13.5 nm distance at the turn (See, Layout 1; Fig. 2.6), for the most optimal geometry allowing predictable signal

propagation through the turn across optimal node distances and allowable turn angles.

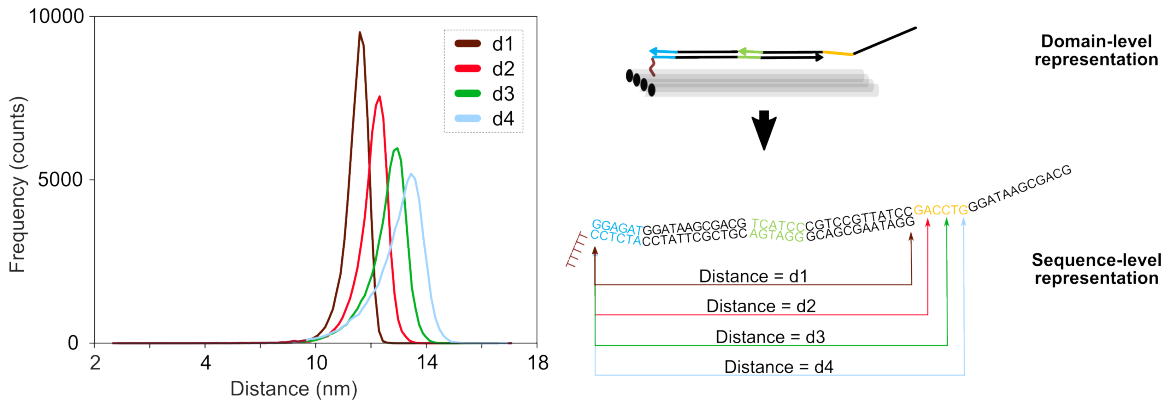

Figure 2.11: OxDNA simulation of maximum reach of a wire node. Schematic diagram on the top right shows the domain-level description of an activated Input hairpin ready for interaction with the next available hairpin on an origami scaffold. The diagram on the bottom right shows the actual sequence-level representation of the wire with corresponding domains coded in same color. We performed Molecular Dynamics simulations using oxDNA to simulate the movement of this construct tethered to a surface by the PolyT domain (brown), and observed the distances between the first 'C' of the Input hairpin adjacent to the poly-T domains: and the 5'-'C' of the stem adjacent to the hairpin loop of the Fuel (brown plot), the 2nd nucleotide 'A' (red plot) ; the 4th nucleotide 'C' (green plot); and the 6th nucleotide 'G' (light blue plot) of the exposed hairpin loop of Fuel complex respectively. The plot on the left shows histograms of these distances for 60793 observations.

2.10.2 *Effect of origami concentration on localized circuit dynamics*

We assembled single spacing and double spacing two hairpin domino wires and tested signal propagation through the wires with 5 nM and 1 nM origami concentrations. There was minimal localized signal propagation if hairpins were at double spacing. We hypothesized that the basal signal increase is primarily due to bimolecular interorigami interactions. Decreasing the origami concentration in the reaction should have minimal effect on the speed of localized unimolecular interactions across a single-spaced two hairpin wire, but the speed of bimolecular interorigami interactions should ideally decrease quadratically with origami concentration. We observed effects consistent with our hypothesis in our experiments as described in Fig. 2.12.

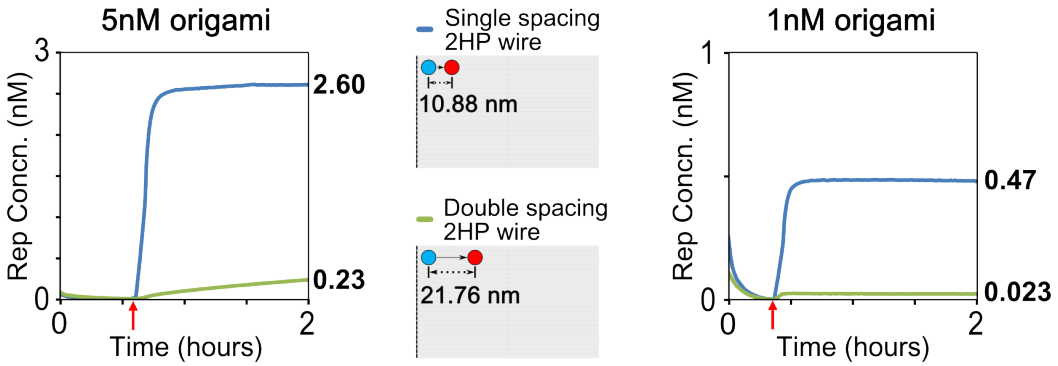

Figure 2.12: Effect of origami concentration on inter-origami interactions. The plots on left and right show concentrations of unquenched fluorophores for reactions starting with 5 nM and 1 nM origami respectively. Blue and green plots correspond to signal transfer through single spacing and double spacing two hairpin wires, respectively. The numbers on the right of each plot denote the unquenched fluorophore concentrations (in nM) for each case after 2 hours. Red arrows below the time axes indicate time points when the experiment was paused for Input addition. Reactions were performed with 200 nM Fuel, 50 nM Input, 40 nM Reporter in 1X TAE/12.5 mM Mg^{++} at 25°C.

In order to quantify how the origami concentration influences the time of circuit completion, we calculated the half-time of signal increase for two hairpin wires. Applying

such a calculation directly to the measurement data is sensitive to the time at which the circuit was triggered by the input strand, but also any experimental noise in the values immediately following circuit triggering. As our experimental procedure did not permit continuous monitoring of the sample during input addition, we used our computational modeling procedure (please refer to the online version of the paper) to determine the input addition time and subsequently provide a more accurate calculation of the circuit half-completion time. The parameters inferred from model parameterization (please refer to the online version of the paper) were used to simulate two hairpin tracks at 5 nM and 1 nM origami concentration, but to ensure that the simulations were an accurate depiction of the measured dynamics, some of the model parameters were re-calibrated (Fig. 2.13). Using the model simulations, we calculated the circuit half-completion times to be 1.52 min for the 5 nM origami concentration data and 1.45 min for the 1 nM origami concentration. As such, the difference in completion times was negligible. The model was also re-simulated in the absence of inter-origami interactions (kl = 0) to see whether the observed increase in the 5 nM case explains the longer completion time (data not shown). This produced values of 1.37 min (5 nM) and 1.35 min (1 nM), suggesting at least part of the discrepancy was due to the impact of interorigami interactions.

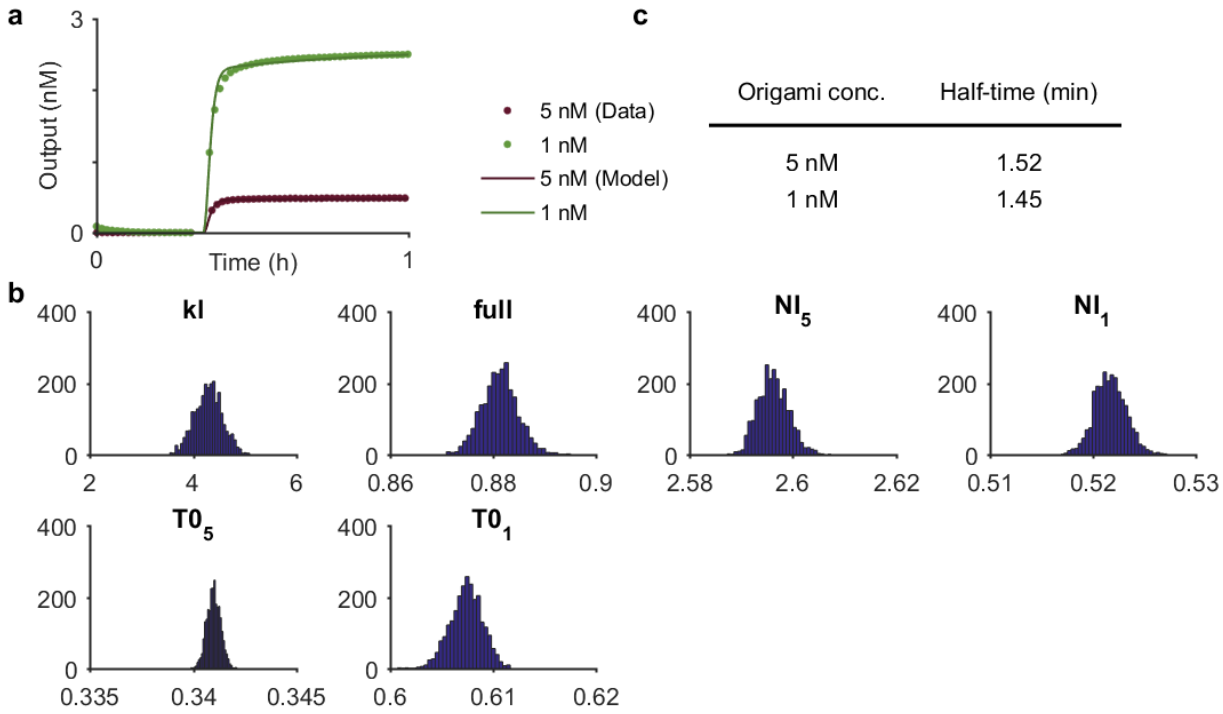

Figure 2.13: Model calibration for quantifying the effect of origami concentration on circuit completion. **(a)** Comparison of model dynamics at optimal parameter values against measured data. Here, the solid lines (model) overlap the measured data almost perfectly, obscuring their visibility. **(b)** Marginal posterior parameter distributions for parameters that were re-calibrated in this analysis. kl is the rate of interorigami interactions, full is the fraction of fully formed two hairpin tracks, NI_k (for k = 1,5) is the concentration of origamis that have an input hairpin incorporated, and $T0_k$ is the time of input trigger addition. Note that the plot in panel a aligns the two traces to use the same input time, $T0_5$. **(c)** Comparison of the computed half-time of circuit completion, for 5 nM and 1 nM origami concentrations.

2.10.3 Allowable turning angles between successive hairpins

To make use of the full 2-dimensional space of a DNA origami scaffold, signal propagation must be able to deviate from straight lines, which necessitates some degree of DNA bending. To determine the extent of the allowable turn angles, we again used molecular dynamics simulations from oxDNA, with details as described above. For a signal to propagate around a bend using our domino architecture (Fig. 2.2d), an Intermediate hairpin that has bound an upstream opened Input or Intermediate hairpin must bend at a junction of two double-stranded segments. Since this is approximately equivalent to a nicked double-stranded molecule, we used the simulations of a nicked double-stranded molecule above to assess the allowable turning angles of our localized molecular circuits. The angle of deviation was computed for each of the 60,000 simulation time steps as follows. For each double-stranded segment, the mean position of each pair of nucleotides was determined, forming an approximation of a central axis. Then, we computed the vectors $\vec{s_1}$ and $\vec{s_2}$ that minimize the mean square orthogonal distance from each nucleotide pair (Fig. 2.14a). The angle of deviation was then computed as:

$$\theta = \cos^{-1}\left(\frac{\vec{s_1}\vec{s_2}}{|\vec{s_1}||\vec{s_2}|}\right) \tag{2.1}$$

As a technical note, it was important to ensure that the segment axial vectors were both aligned according to the same direction along the whole molecule. We implemented this by comparing the largest X, Y or Z component of the vector with the corresponding components of the nucleotides, and flipping the vectors as necessary. Without doing this, the computed turn angle could erroneously return 180-θ instead of θ. It is important to note the structural details of the formation of a wire between two hairpins on the origami scaffold to assess the behavior of signal propagation using the domino circuit design.

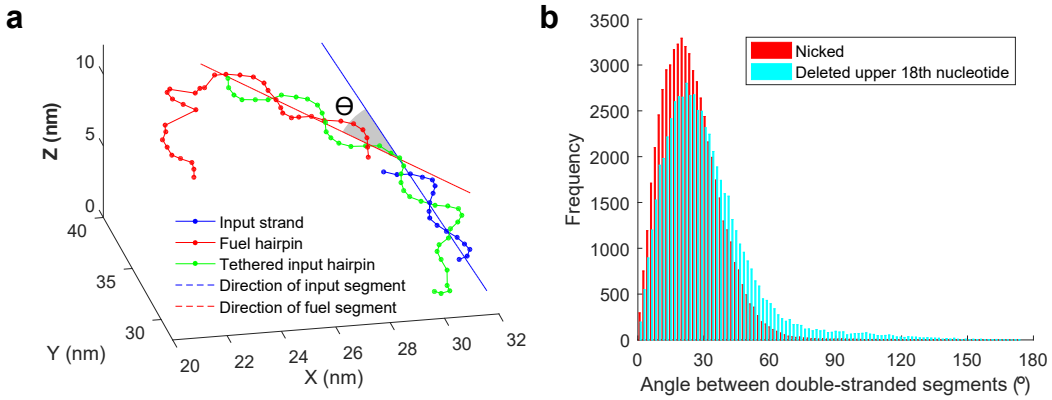

Figure 2.14: oxDNA simulation of the angle of deviation of nicked double-stranded DNA. (a) Example output from oxDNA during a simulation of nicked double-stranded DNA. Each circle represents a single nucleotide contained within the input strand (blue), the opened fuel hairpin (red) or the opened tethered hairpin (green). In this example, the 18th nucleotide of the input strand has been deleted. The thin solid straight lines indicate the average direction vectors of the double-stranded segments either side of the nick, and the angle of deviation (θ) is also indicated. **(b)** The histogram summarizes the distribution of deviation angles for nicked DNA molecules in an oxDNA simulation of 60,000 steps. Compared are nicked double-stranded DNA and a molecule in which the 18th nucleotide of the input strand has been removed.

When the semi-stiff nicked double stranded wire node interacts with the next available hairpin (Fig. 2.1b, 3rd panel), the junction where the next hairpin forms a part of the wire is nicked, but the polyT linker at the 5′ end of the second hairpin prevents any base stacking between the nucleotides around the nick. The loss of base stacking at this nick can affect the bending of a double stranded complex from that junction by making it more flexible. To assess this, we carried out oxDNA molecular dynamics simulations after removing the 18th nucleotide from the upper strand of the first segment (blue colored Input strand, Fig. 2.14a). In addition to calculating the distribution of angles for nicked double-stranded wire node (Fig. 2.14b), we also applied the calculation to simulations with the duplex with base deletion. As expected, there was a minor shift of distribution with slightly more affinity for the duplex with base deletion bending over higher angles

(>60 degrees) at the junction. But, the likelihood that the wires turn over high angles were significantly low. While preparing all our circuit layouts, we carefully positioned the hairpins on the scaffold such that the signal transmission wires formed didn't experience significant strain while bending over high angles to reach to the next available hairpin.

2.10.4 A three hairpin domino wire

A three hairpin domino wire comprises of an Input hairpin, an Intermediate hairpin and an Output hairpin, positioned at equal distances (single spacing) on the origami scaffold. The Intermediate hairpin is structurally similar to the Input hairpin, but with the 5′-toehold domain being complementary to the hairpin loop of the Fuel rather than to the toehold of the single-stranded input. Thus an Intermediate hairpin is triggered by an opened Fuel. The hairpin loop of the Intermediate hairpin is complementary to the 3′-toehold of the Fuel. Fig. 2.15 schematically demonstrates the reaction mechanism for signal propagation along a three hairpin domino wire.

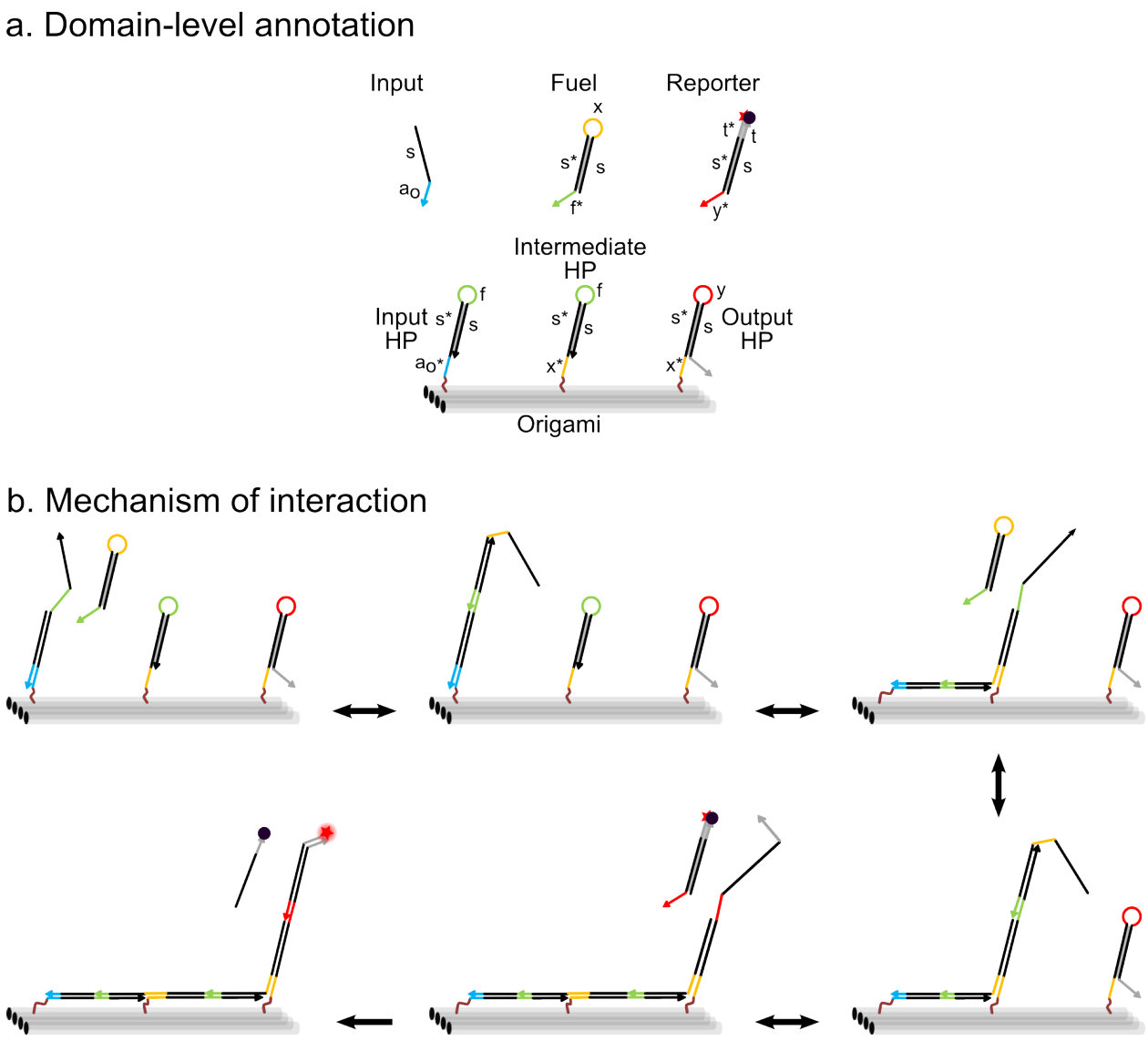

Figure 2.15: A three hairpin domino wire. a) Domain-level schematic representation of the localized and non-localized components involved in a three hairpin domino wire: the most basic but comprehensive module in our study. **b**) Stepwise illustration of the mechanism of components interaction from an activated Input hairpin (top left) to unquenching of the fluorophore (bottom left). Each black thick arrow between panels represents a strand displacement reaction.

2.10.5 Predictable localized interactions between adjacent hairpins

Localized signal propagation between an Input hairpin and an Output hairpin was found to be highly predictable based on the relative distances of separation (i.e. spacing) between the two hairpins. We next asked whether longer wires missing Intermediate hairpins would behave with similar predictability (Fig. 2.16). We observed a minimally higher signal with an Output hairpin at double spacing, than with an Output hairpin at triple spacing. The latter signal was comparable to the signal due to interorigami interactions (Fig. 2.1c, 3rd panel). This may occur due to the fact that semi-stiff nicked double stranded wire formed between the first two hairpins may have a tendency to direct the activated hairpin loop domain of the Fuel and push it a bit forward to reach for a hairpin along its pre-existing direction. To test any unpredictable signal propagation across unintended paths, we tested how a pre-formed wire propagates signal based on the position of the next available hairpin. We positioned an Input hairpin and an Intermediate hairpin adjacent to each other at theoretical predicted distances (single spacing), and then positioned two different Output hairpins, each capable of triggering an orthogonal Reporter. One of the Output hairpins was positioned at a single spacing, while the other was positioned at a double spacing distance from the Intermediate hairpin. We showed that signal propagation was always preferred across adjacent hairpins separated by single spacing. This supports the overall robustness and predictability of the domino circuit design principles presented in this study, such that signal propagation through the wires occur sequentially between adjacent hairpins, and there was very minimal signal propagation through unintended paths across skipped hairpins in a properly formed circuit.

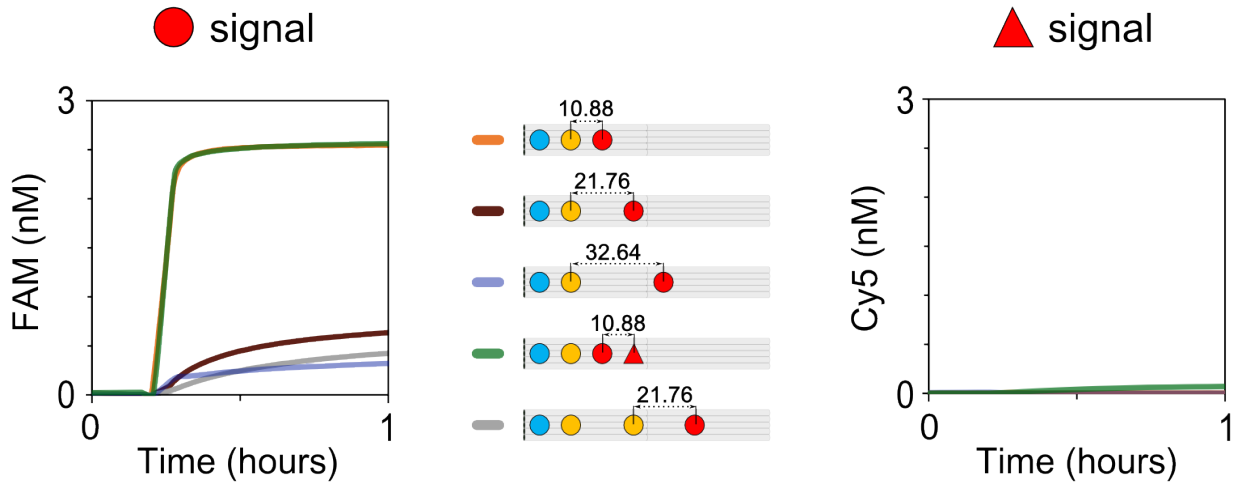

Figure 2.16: Preferential signal transfer across hairpins separated by single spacing. Different multi-hairpin wires were prepared to test whether formation of a wire between two hairpins at the upstream region affects the maximal reach of the successive hairpins. All the constructs tested in this experiment had an Input hairpin and a single-spaced Intermediate hairpin at the upstream region, followed by hairpins positioned at different distances from the upstream Intermediate hairpins, as shown in the figure legend. The calculated distances between different hairpins (in nm) for each unique case is indicated. The graphs on the left and right show unquenched fluorophore concentrations due to signal propagation through Output hairpin 1 (red circle) and Output hairpin 2 (red triangle) in: a three hairpin single-spaced wire (orange), a three hairpin wire where the Output hairpin is placed at double spacing (brown) and triple spacing (light blue) from the Intermediate hairpin, a three hairpin wire with Output hairpin 1 at single spacing and Output hairpin 2 at double spacing from the Intermediate hairpin (green) and a six hairpin wire with 3rd and 5th hairpin missing (grey). Red arrows at the time axes indicate time points when the Input was added. Reactions were carried out with 5 nM origami, 40 nM Reporters, 200 nM Fuel, 50 nM Input in 1X TAE/Mg^{++}.

2.10.6 Signal loss

The efficiency of incorporation of individual staples may vary depending on the annealing protocol, staple sequences, position of the staple in the scaffold, and/or structural and conformational intermediate states that the origami attains during annealing [113, 114]. Imperfect incorporation of staples that are modified with hairpins will directly and negatively affect domino circuit performance.

Experimentally, we observed a gradual but non-monotonic decrease in the extent of signal propagation for wires of increasing lengths (Fig. 2.2b). These results are consistent with the hypothesis that hairpins are missing with a non-zero probability and that signals can only propagate efficiently if all hairpins are present in a given wire. We used 5 nM annealed origami for all experiments presented in Fig. 2.2b and triggered the signal propagation with an excess of 50 nM Inputs. Since the origami were the limiting reagent, the final steady state signals observed were representative of the concentrations of functional origami in each case.

To estimate the percentage of perfect wires as a function of wire lengths we repeated signal propagation experiments with two to eight hairpin wires but using only 1 nM Input (Fig. 2.17, right column). In these experiments the Input strands were limiting and the final steady state signals are thus representative of the ratio of properly formed to misformed origamis. Inputs interact with the Input hairpins irrespective of whether they are part of properly formed or misformed origamis. As an example, the final steady state signal (at t = 10 hours) for a four hairpin wire was 0.82 nM, meaning that 82% of the total origamis were properly formed in this case. Overall we observed gradual signal loss with increasing number of hairpins (Fig. 2.18), with some abnormalities (three hairpin wire and eight hairpin wire) which may be due to variation in hairpin incorporation efficiencies across different positions. When the signal values when normalized to the maximum

signal obtained in each case (Fig. 2.17, bottom row), we saw the expected gradual delay in signal propagation with increasing number of hairpins.

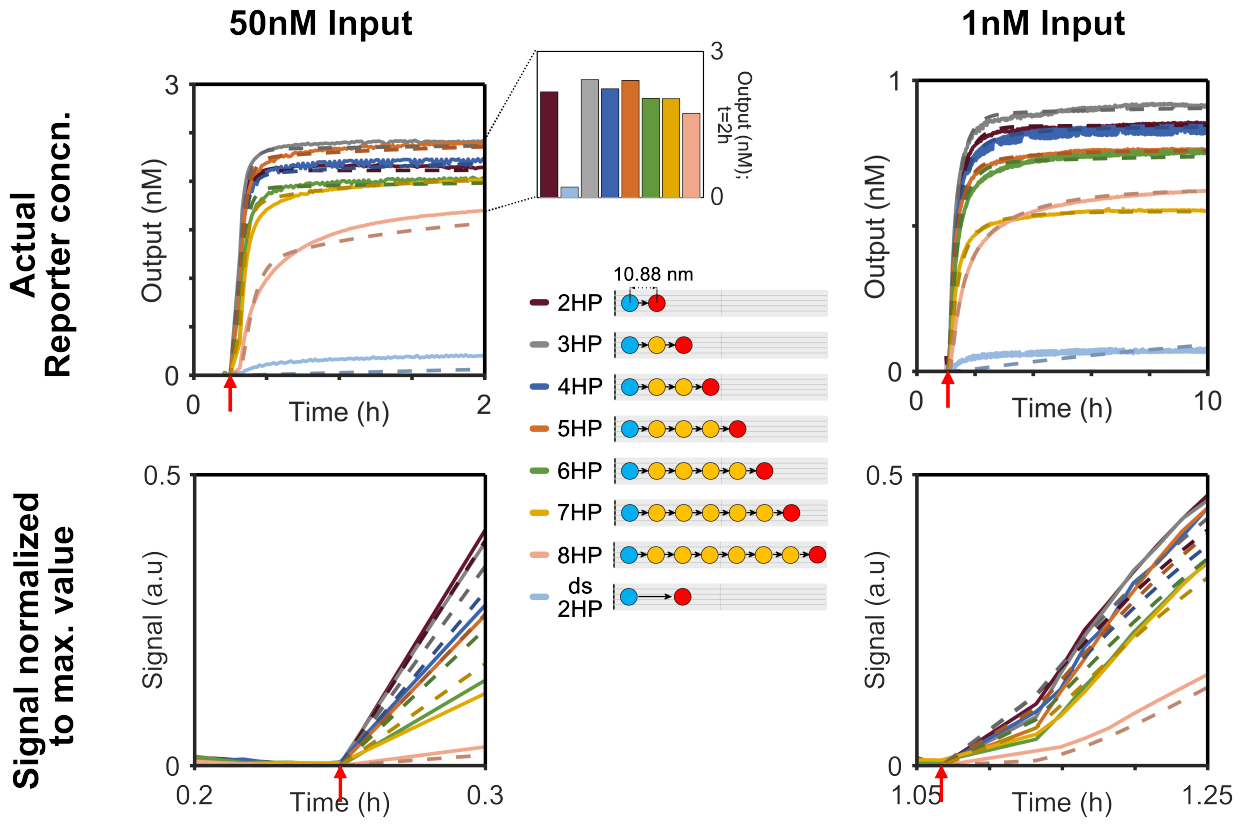

Figure 2.17: Signal propagation across two to eight hairpin wires with varying Input concentrations. Top row: Unquenched fluorophore concentrations reflecting signal transfer across two to eight hairpin wires parallel to the helical axis of the origami upon addition of 50 nM (left, Same as Fig. 2.2b) and 1 nM Input (right). Plots of different colors correspond to wires of different lengths and number of hairpins, and are graphically explained in the legend. "ds 2HP" represents a double-spaced two hairpin wire. Inset shows the unquenched fluorophore concentrations due to signal transfer across two to eight hairpin wires at time=2 hours. The bar colors are correlative to the plots. **Bottom row**: Normalized plots obtained by dividing each data point for a specific wire to the maximum signal for that wire. Red arrows at the time axes indicate time points when the Input was added. Reactions were carried out at 25°C with 5 nM origami, 40 nM Reporter, 200 nM Fuel in 1X TAE/Mg^{++}.

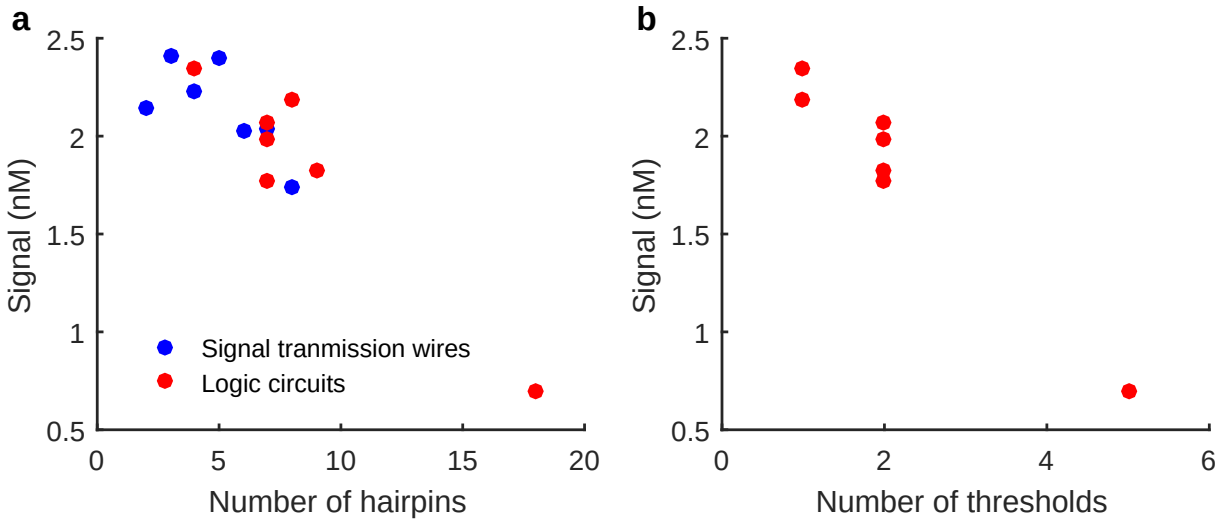

Figure 2.18: Completion levels decrease with increasing number of components. This figure summarizes the signal completion levels from a range of domino wires and logic circuits, when the circuit has all inputs required to produce the output signal. The completion levels are compared against (**a**) the number of hairpins in each circuit, and (**b**) the total number of threshold hairpins used in the circuit.

2.10.7 *Positional dependence of signal transfer*

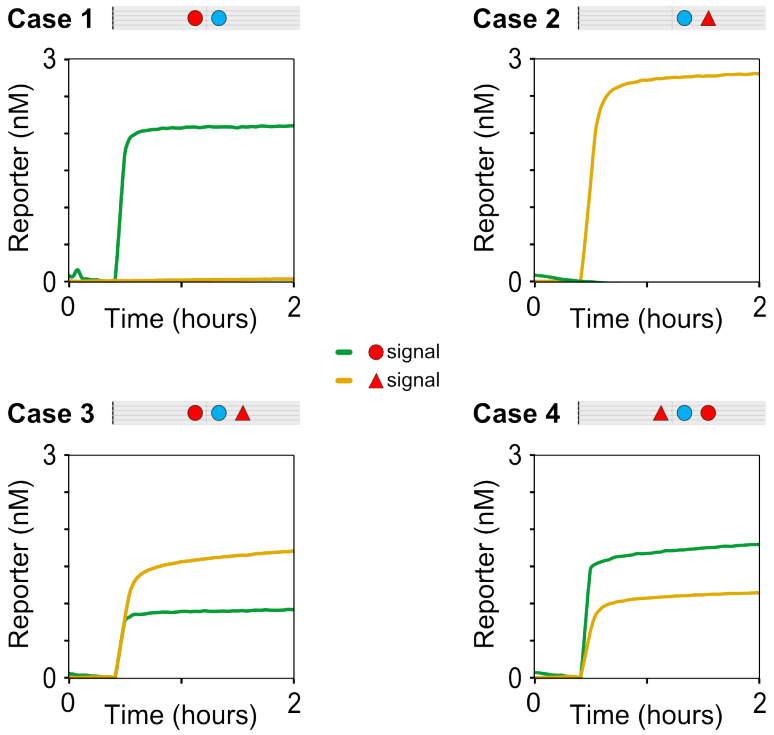

Figure 2.19: Positional dependence of signal transfer on origami. Signal propagation across a two hairpin domino wire, with the output hairpin in different positions along a helical axis. The hairpin position is given by row and column number according to (Fig. 2.6), where R2C1 denotes a hairpin at row 2 and column 1. **Case 1:** Origami with Input hairpin (HP) (blue circle) on R2C2 and Output HP1 (red circle) on R2C-1; **Case 2:** Origami with Input HP on R2C2 and Output HP2 (red triangle) on R2C4; **Case 3**: Origami with Input HP on R2C2, Output HP1 on R2C-1 and Output HP2 on R2c4; **Case 4:** Origami with Input HP on R2C2, Output HP1 on R2c4 and Output HP2 on R2c-1. Output HP1 and Output HP2 had orthogonal hairpin loops triggering separate Reporters (Reporter1 with FAM and Reporter2 with Cy5 fluorophores). The green plots denote signal increase due to signal propagation through Output HP1 and the yellow plots denote signal increase due to signal propagation through Output HP2. Reactions were carried out with 5 nM origami, 40 nM Reporter1, 40 nM Reporter2, 100 nM Fuel, 50 nM Input in 1X TAE/Mg^{++} at 25°C.

2.10.8 Interorigami interactions with multi-hairpin wires

Wires with multiple Output hairpins To observe the effect of inter-origami interactions, we tested signal propagation through four origami constructs (Case 1-4). Case 1 represents a localized two hairpin domino wire, Constructs in Cases 2, 3 and 4 were intentionally designed such that the Input hairpin and Output hairpin(s) cannot interact with each other locally; signals can only propagate through interorigami interactions. Case 2, 3 and 4 had 2, 3 and 4 Output hairpins per origami molecule respectively and were used to quantify the effect of the number of hairpins present in an origami as "contact points" for interorigami interactions. Fig. 2.20 demonstrates signal propagation through these constructs with initial origami concentrations of 5 nM (left plot) and 1 nM (right plot). For unimolecular localized interactions across a localized two hairpin domino wire (Case 1), we saw fast and robust signal transfer ($t_{1/2}$ <3 mins.) with speeds remaining unaffected with lower concentrations of origami. Signal transfer was significantly lower when the Input hairpin and Output hairpin were spatially separated to different edges of the origami (Case 2). Moreover, the extent of signal propagation was drastically reduced for lower initial origami concentration (1 nM), consistent with signal propagation through bimolecular inter-origami interactions. The rate of signal transfer was found to be proportional to the number of Output hairpins present per origami molecule (Cases 2-4).

Figure 2.20: Effect of hairpin density and origami concentrations on interorigami interactions. Left and right graphs show concentrations of unquenched fluorophores for reactions starting with 5 nM and 1 nM origami respectively. Blue plots denote two hairpin domino wires (positive control) - Case 1; brown, green and purple plots denote non-localized signal transfer between origamis having 1 Input hairpin and 1 (case 2), 2 (case 3) and 3 (case 4) Output hairpins respectively. The numbers on the right of each plot denote the unquenched fluorophore concentrations of each cases after 4 hours. Red arrows below the time axes indicate time points when the Input was added. Reactions were carried out with 40 nM Reporter, 100 nM Fuel, 50 nM Input in 1X TAE/Mg^{++} at 25°C.

Eight hairpin wire: Different cases of interorigami interactions To further analyze inter-origami interactions in a multiple hairpin wire, we constructed variants of the eight hairpin domino wire along the helical axis (Fig. 2.2a). Specifically, we tested the effects of multiple Intermediate hairpins on an origami molecule on inter-origami interactions and the effect of presence of an Input hairpin or an Output hairpin. This experiment was performed to resemble possible scenarios in our experiments where a minute portion of the annealed origamis may have one or more of the hairpins missing. We tested four possible cases of inter-origami interactions as described in Fig. 2.21. Compared to the localized signal propagation in a fully formed eight hairpin wire, the interorigami interactions were significantly slower, as expected. When one of the origami (bottom origami in each case) had six Intermediate hairpins with an Output hairpin (Case 1 and 2), interorigami interactions were more significant than in situations where one origami had only an Output hairpin (Case 3 and 4). This suggests that , all the Intermediate hairpins and the Output hairpins can act as "contact points" to for an interorigami interaction. Also, interorigami interactions may be faster through an Intermediate hairpin than an Output hairpin, owing to the possibility that the 3′ flanking domain (t) of the Output hairpin can block its 5′ toehold due to partial complementarity. The minor decrease in signal in Case 2 compared to Case 1, and Case 4 compared to Case 3 can be due to the fact that: a) In these cases there were significantly more number of participating hairpins leading to more paths of interorigami interactions, and possible delays in signal transfer to an Output hairpin, and/or b) In these cases localized signal propagation happened before a signal propagated through interorigami interactions, thereby causing a minor delay.

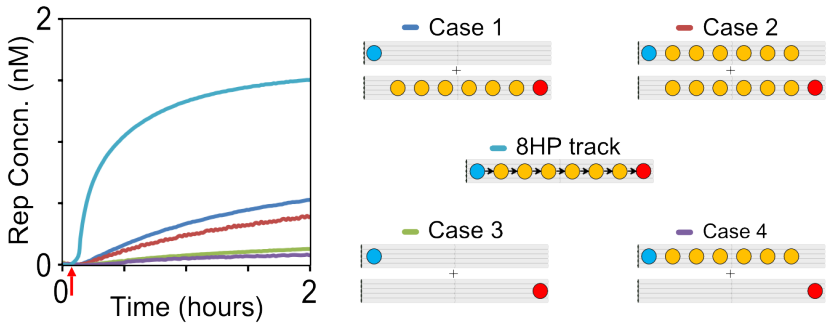

Figure 2.21: Inter-origami interactions in an eight hairpin domino wire. Light blue plot (8HP track) denotes an eight hairpin domino wire (positive control) ; Case 1 (dark blue plot) denotes non-localized signal transfer between equimolar concentrations of origamis with only one Input hairpin, and origamis with six Intermediate hairpins and one Output hairpin; Case 2 (brown plot) denotes non-localized signal transfer between equimolar concentrations of origamis with one Input hairpin and six Intermediate hairpins, and origamis with six Intermediate hairpins and one Output hairpin; Case 3 (green plot) denotes non-localized signal transfer between equimolar concentrations of origamis with one Input hairpin, and origamis with one Output hairpin; and Case 4 (purple plot) denotes non-localized signal transfer between equimolar concentrations of origamis with one Input hairpin and six Intermediate hairpins, and origamis with one Output hairpin. Red arrows below the time axes indicate time points when the Input was added. Unless specified, reactions were carried out with 5 nM origami, 40 nM Reporter, 200 nM Fuel, 50 nM Input in 1X TAE, 12.5 mM Mg^{++}.

2.10.9 Mechanism of thresholding

A Thresholding module consists of an Output hairpin and a Threshold hairpin both positioned at equal distances from an Input hairpin, on the origami scaffold. The Threshold hairpin is similar to an Intermediate hairpin, but with a hairpin loop (w) which is non-reactive to the toehold of the Fuel, but instead interacted with a partially-double stranded complex, "Threshold block". The Output hairpin is modified by shortening its 5'-toehold from the 5'-end by two or three nucleotides (xs*) for our thresholding analysis experiments (Fig. 2.4b). Upon addition of an Input strand, the Input hairpin interacted with the Fuel complex and exposed the previously sequestered hairpin loop domain. At this stage, the exposed domain preferentially interacted with the Threshold hairpin through an enthalpy-driven strand displacement reaction via its 6 nucleotide toehold, compared to the shorter toehold of the corresponding Output hairpin. The preferential binding to the Threshold hairpin depended upon the difference in lengths of interacting toeholds. Upon interaction between the Input hairpin and the Threshold hairpin, the exposed hairpin loop of the Threshold hairpin was irreversibly blocked by the Threshold block, to prevent any reverse reaction that may happen due to closing back of the Threshold hairpin. This resulted in favorable thresholding and ultimately effective truncation of signal transfer as per design. Fig. 2.22 schematically demonstrates the stepwise operation of a Thresholding module. Based on our Thresholding analysis, we chose a toehold length of 3 nucleotides for the Output hairpins (xs*) for all the logic circuit modules demonstrated in this study.

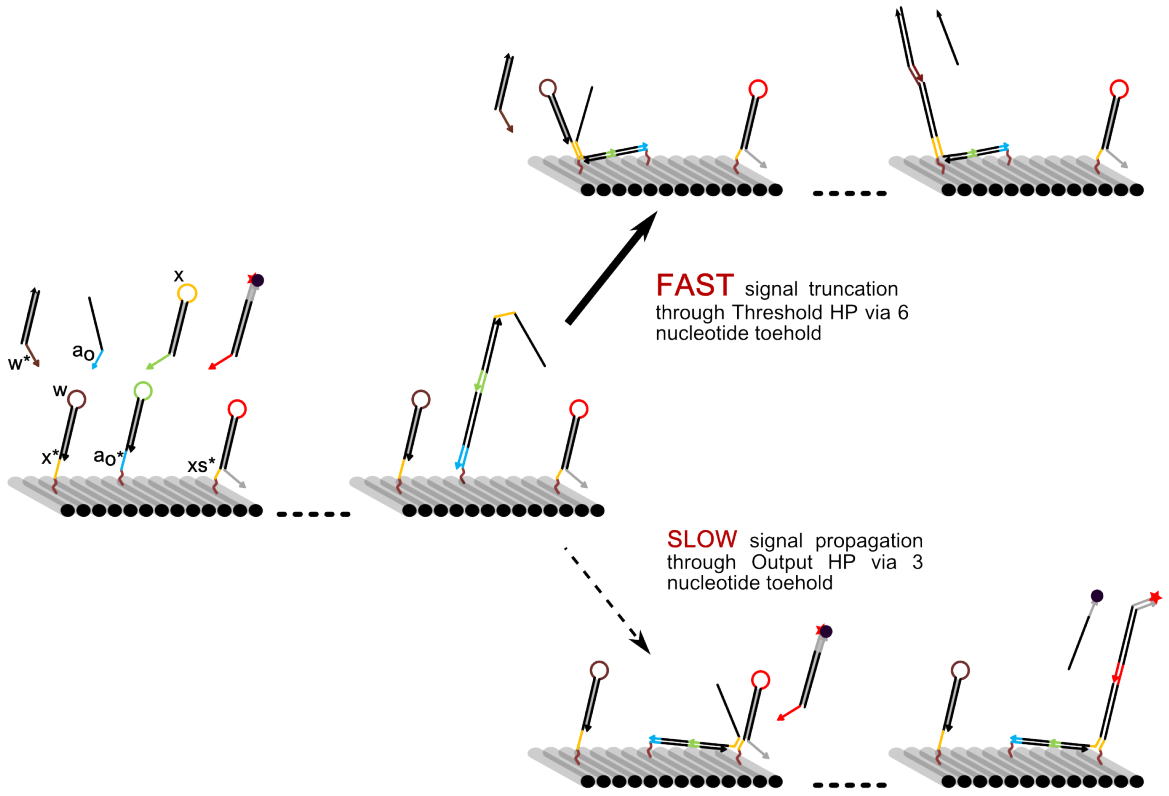

Figure 2.22: Mechanism of Thresholding. Detailed stepwise operation of signal thresholding upon Input addition through a Thresholding module. The thick solid arrow denotes fast and preferential interaction of the Intermediate complex with the Threshold hairpin via its 6 nucleotide toehold, compared to the slow and less probable signal propagation through Output hairpin via its 3 nucleotide toehold (thin dotted arrow).

2.10.10 Performance comparison

The previous study by Qian et al.[**?**] with diffusible components, demonstrates the state-of-the-art in the field of complex DNA logic circuits. This section highlights some advantages of the DNA domino architecture over the current state-of-the-art system by comparing some key features.

Key differences between systems: 5 nt. toehold sequences, non-hairpin constructs (Qian et al.) vs. 6/3 nt. toehold sequences, hairpin constructs (our study); 20°C experiments (Qian et al.) vs. 25°C experiments (our study); 150 nM Reporter (Qian et al.) vs. 40 nM Reporter (our study); 100 nM Input (Qian et al.) vs. 50 nM Input (our study).

Table 2.1: Domino Circuits vs. Current state-of-the-art

Category	**Qian et al. (2011)**	**This study**
Operating concentration of Gate component	100 nM	˜2 nM
3 Input AND GATE (2 AND Gates in series): $T_{1/2}$	>4 hours (Fig. S5B)	<7 minutes
4 layered gate (4-layered OR Gate with one input (x_2) vs. 4 hairpin domino wire): $T_{1/2}$	>2 hours (Fig. S6)	<5 minutes
Number of unique domains required for a 2 Gate circuit (3 Input AND GATE)	11 [**3*(no. of Gates) + (no. of inputs) + (no. of outputs) + 1**]	9 [**(no. of inputs) + (no. of outputs) + 5**]
Number of unique domains required for a 4 Gate circuit (4 Input OR GATE)	19	10 (not shown here)

2.10.11 Energy calculations

The thermodynamic driving force was analyzed for interactions between circuit components at each step of a two hairpin wire by calculating the net change in standard Gibb's free energy ($\Delta\Delta G^\circ$), using both NUPACK and our parameterized model (Table 2.2). Using NUPACK, the free energy of secondary structure formation (ΔG°) was first computed for the individual circuit components, before subsequently computing the intermediate state secondary structures. The thermodynamic driving force at each step of signal transmission can be approximated to be the difference of free energy values between the product(s) and the reactant(s) after being corrected for any entropic change. We included possible entropy loss due to association of two molecules in the form of initiation entropy of 6.4 cal/mol/K per association[37] at 25°C or 298 K. Using the model that includes hairpin closing (Section **??**), we calculated the equilibrium rate constant (K_{eq}) for each reversible step of signal transmission as the ratio of the forward and reverse reaction rates. As the Reporter binding step was irreversible, an equilibrium rate constant could not be calculated in this case. The net standard free energy change ($\Delta\Delta G^\circ$) was then calculated from the equilibrium rate constant values according to

$$\Delta\Delta G^\circ = -RT \ln K_{eq} \tag{2.2}$$

where R is the gas constant and T is the reaction temperature in Kelvin.

Table 2.2: Thermodynamics of signal transmission through a two hairpin wire

Step	$\Delta\Delta G^\circ$ **calculated from model (kcal/mol)**	$\Delta\Delta G^\circ$ **calculated from NUPACK (kcal/mol)**
Input binding	-7.7	-10.98
Fuel binding	-7.68	-10.69
Output hairpin binding	-6.48	-9.35
Reporter binding (quencher strand release)	–	-7.83

2.10.12 Sequences of staples and domino circuit components

The complete set of staple sequences and the sequence of m13mp18 viral template DNA can be found in the online version of this paper. Alternatively, it can be found from the following link: http://www.bayoubiolabs.com/biochemicat/vectors/pUCM13/.

Table 2.3: Staples modified for domino wires

Direction of wires	Staples	Sequences of staples
Parallel to helical axis	R2c-7	TTGACCCCCTTGCAGGGAGTTAAAACAGCTTG
	R2c-5	AGAGGCAATCGTCACCCTCAGCATATCAGC
	R2c-3	TGCCACTAGAACGAGGGTAGCAACGGCTCCAA
	R2c-1	ACAGGAGTGCGTCATACATGGCTTATTTTTTC
	R2c2	CGGCATTTCTTTTCATAATCAAATTACCGT
	R2c4	CCTTTAGCCCACCACCGGAACCGCTAAAGCCA
	R2c6	ACCGTAATCACCCTCAGAACCGCCCCTTGATA
	R2c8	GAAACGTCCCCTCAGAGCCGCCAGACAGGA
Perpendicular to helical axis	R2c2	CGGCATTTCTTTTCATAATCAAATTACCGT
	R8c2	CAAGATTACTGAATCTTACCAACGAGATAA
	R14c2	AATCGTCGAACATAGCGATAGCTGATAAAT
	R20c2	GCGAACTGAACGAACCACCAGCACGTCAAT
Through a 180 degree turn	R20c6	CCTGAAAGAGTGCCACGCTGAGAGAAAGGAAT
	R14c6	ACCTTTTTAGGTCTGAGAGACTACAAATATAT
	R8c6	TCTAAGAACAGCCATATTATTTATAGACGGGA
	R2c6	ACCGTAATCACCCTCAGAACCGCCCCTTGATA
	R4c4	ACACCACGGGTAAATATTGACGGACAAGTTTG
	R8c2	CAAGATTACTGAATCTTACCAACGAGATAA
	R14c2	AATCGTCGAACATAGCGATAGCTGATAAAT
	R20c2	GCGAACTGAACGAACCACCAGCACGTCAAT
Wire crossover	R20c2	GCGAACTGAACGAACCACCAGCACGTCAAT
	R14c2	AATCGTCGAACATAGCGATAGCTGATAAAT
	R8c2	CAAGATTACTGAATCTTACCAACGAGATAA
	R2c2	CGGCATTTCTTTTCATAATCAAATTACCGT
	R11c-2	AATGCTTTCAAAAATCAGGTCTGTAGCTCA
	R11c1	GTCTGGAATTAAATATGCAACTAAAAATAATA
	R11c3	GCGTCTTTCGGGAGGTTTTGAAGCTAGAAACC
	R11c5	AAATAAACGCGAGGCGTTTTAGTATCATTC
	R11c7	AAATAAGAAGATATAGAAGGCTTAACCGCACT

Table 2.4: Circuit components for domino wires

Component	Domains (5′-3′)	Sequence (5′-3′)
Input hairpin (blue circle, Fig. 2.2a)	polyT ao* s* f s	TTTTT CCTCTA CCTATTCGCTGC AGTAGG GCAGCGAATAGG
Intermediate hairpin (yellow circle, Fig. 2.2a)	polyT x* s* f s	TTTTT CTGGAC CCTATTCGCTGC AGTAGG GCAGCGAATAGG
Output hairpin 1 (red circle, Fig. 2.2a)	polyT x* s* y s t	TTTTT CTGGAC CCTATTCGCTGC CAATCA GCAGCGAATAGG ACCAAG
Output hairpin 2 (red triangle, Fig. 2.19, 2.16)	polyT x* s* y2 s t	TTTTT CTGGAC CCTATTCGCTGC CTCATT GCAGCGAATAGG ACCAAG
Fuel	s x s* f*	GCAGCGAATAGG GTCCAG CCTATTCGCTGC CCTACT
Input-A	s ao	GCAGCGAATAGG TAGAGG
Reporter 1 fluorophore strand	FAM t* s* y*	/56-FAM/ CTTGGT CCTATTCGCTGC TGATTG
Reporter 1 quencher strand	s t FQ	GCAGCGAATAGG ACCAAG /3IABkFQ/
Reporter 2 fluorophore strand	Cy5 t* s* y2*	/5Cy5/ CTTGGT CCTATTCGCTGC AATGAG
Reporter 2 quencher strand	s t RQ	GCAGCGAATAGG ACCAAG /3IAbRQSp/

Table 2.5: Circuit components for wire crossover module

Component	Domains (5′-3′)	Sequence (5′-3′)
Input hairpin A (blue circle: A, Fig. 2.3)	polyT ao* s* f s	TTTTT CCTCTA CCTATTCGCTGC AGTAGG GCAGCGAATAGG
Input hairpin B (blue circle: B, Fig. 2.3)	polyT bo* s* fc s	TTTTT AGTGCT CCTATTCGCTGC TGACGT GCAGCGAATAGG
Intermediate hairpin x:f (yellow circle in A track, Fig. 2.3)	polyT x* s* f s	TTTTT CTGGAC CCTATTCGCTGC AGTAGG GCAGCGAATAGG
Intermediate hairpin xc:fc (purple circle in B track, Fig. 2.3)	polyT xc* s* fc s	TTTTT TTAGCG CCTATTCGCTGC TGACGT GCAGCGAATAGG
Intermediate hairpin xc:f (yellow circle in B track, Fig. 2.3)	polyT xc* s* f s	TTTTT TTAGCG CCTATTCGCTGC AGTAGG GCAGCGAATAGG
Output hairpin FAM (red circle: FAM, Fig. 2.3)	polyT x* s* y s t2	TTTTT CTGGAC CCTATTCGCTGC CAATCA GCAGCGAATAGG ACTTTG
Output hairpin Cy5 (red circle: Cy5, Fig. 2.3)	polyT x* s* y2 s t2	TTTTT CTGGAC CCTATTCGCTGC CTCATT GCAGCGAATAGG ACTTTG
Fuel1	s x s* f*	GCAGCGAATAGG GTCCAG CCTATTCGCTGC CCTACT
Fuel2	s xc s* fc*	GCAGCGAATAGG CGCTAA CCTATTCGCTGC ACGTCA
InputA	s ao	GCAGCGAATAGG TAGAGG
InputB	s bo	GCAGCGAATAGG AGCACT
ReporterFAM fluorophore strand	FAM t2* s* y*	/56-FAM/ CAAAGT CCTATTCGCTGC TGATTG
ReporterFAM quencher strand	s t2 FQ	GCAGCGAATAGG ACTTTG /3IABkFQ/
ReporterCy5 fluorophore strand	Cy5 t2* s* y2*	/5Cy5/ CAAAGT CCTATTCGCTGC AATGAG
ReporterCy5 quencher strand	s t2 RQ	GCAGCGAATAGG ACTTTG /3IAbRQSp/

Table 2.6: Staples modified for two-input OR, two-input AND, three-input AND, six-input AND domino gates

Staples	Sequences of staples
R20c-7	CCACGCTGTGAGTGAGCTAACTCAGTGTGAAA
R15c-8	AGTAGTAGGTGAGAAAGGCCGGACCGTTCT
R15c-6	AGGCAAGGGCCTGAGTAATGTGTAGGGTAGCT
R10c-7	AACCTGTTGAGAGTACCTTTAATTAAAGACTT
R5c-8	GCTGAGGCAGCGATTATACCAAATCGCCTG
R5c-6	TTGCGGGAAAGAATACACTAAAACCCTGCTCC
R0c-7	ATACCGATTTTCCAGACGTTAGTAACCAGTAC
R5c-4	CAGCATCGCGAAGGCACCAACCTAGCAGACGG
R3c-2	AACTAAAAATCTCCAAAAAAAAGGCTACAG
R7c-2	GAAAGAGGGCTGGCTGACCTTCCGTTAATA
R5c1	GGCGCATAGACAGATGAACGGTGTCAGCGCCA
R5c3	AACCAGAGGTCAGACTGTAGCGCGCGATTGAG
R0c4	GAATGGAACCTTGAGTAACAGTGCTATAGCCC
R5c5	GAGCCGCCAGTAGCGACAGAATAATTATTC
R10c4	TCAGCTAAATCGGCTGTCTTTCCTCGAACCTC
R15c3	ATGCGTTAGAAATACCGACCGTGTTAGATTAA
R15c5	CAACGCTATTTCATCTTCTGACATTTATCA
R20c4	ATATTTTTTGAGGCGGTCAGTATTTTTAGGAG

Table 2.7: Circuit components for two-input OR, two-input AND, three-input AND, six-input AND domino gates

Component	Domains (5′-3′)	Sequence (5′-3′)
Input hairpin-A	polyT ao* s* f s	TTTTT CCTCTA CCTATTCGCTGC AGTAGG GCAGCGAATAGG
Input hairpin-B	polyT bo* s* f s	TTTTT AGTGCT CCTATTCGCTGC AGTAGG GCAGCGAATAGG
Input hairpin-C	polyT co* s* f s	TTTTT CTCGTT CCTATTCGCTGC AGTAGG GCAGCGAATAGG
Input hairpin-D	polyT do* s* f s	TTTTT ACTAAT CCTATTCGCTGC AGTAGG GCAGCGAATAGG
Input hairpin-E	polyT eo* s* f s	TTTTT TTAGCG CCTATTCGCTGC AGTAGG GCAGCGAATAGG
Input hairpin-F	polyT fo* s* f s	TTTTT AATGAG CCTATTCGCTGC AGTAGG GCAGCGAATAGG
Threshold hairpin	polyT x* s* w s	TTTTT CTGGAC CCTATTCGCTGC ACGTCA GCAGCGAATAGG
Intermediate hairpin	polyT xs* s* f s	TTTTT GAC CCTATTCGCTGC AGTAGG GCAGCGAATAGG
Output hairpin 1 (FAM)	polyT xs* s* y s t2	TTTTT GAC CCTATTCGCTGC CAATCA GCAGCGAATAGG ACTTTG
Output hairpin 2 (Cy5)	polyT xs* s* y2 s t2	TTTTT GAC CCTATTCGCTGC CTCATT GCAGCGAATAGG ACTTTG
Fuel	s x s* f*	GCAGCGAATAGG GTCCAG CCTATTCGCTGC CCTACT
Input-A	s ao	GCAGCGAATAGG TAGAGG
Input-B	s bo	GCAGCGAATAGG AGCACT
Input-C	s co	GCAGCGAATAGG AACGAG
Input-D	s do	GCAGCGAATAGG ATTAGT
Input-E	s eo	GCAGCGAATAGG CGCTAA
Input-F	s fo	GCAGCGAATAGG CTCATT
Threshold block strand1	s* w*	CCTATTCGCTGC TGACGT
Threshold block strand2	s	GCAGCGAATAGG
Reporter 1 (FAM) fluorophore strand	FAM t2* s* y*	/56-FAM/ CAAAGT CCTATTCGCTGC TGATTG
Reporter 1 (FAM) quencher strand	s t2 FQ	GCAGCGAATAGG ACTTTG /3IABkFQ/
Reporter 2 (Cy5) fluorophore strand	Cy5 t2* s* y2*	/5Cy5/ CAAAGT CCTATTCGCTGC AATGAG
Reporter 2 (Cy5) quencher strand	s t2 RQ	GCAGCGAATAGG ACTTTG /3IAbRQSp/

Table 2.8: Staples modified for dual rail two-input XNOR domino gate

Staples	Sequences of staples
R1c-6	TGTACCGTAACACTGAGTTTCGTCAATGAATT
R1c-2	GAACCGCCACCCTCAGAGCCACCAAAGGAAC
R1c3	GGAATAGGTGTATCACCGTACTCATTTAACGG
R3c-4	ACAGTTTCTTTAATTGTATCGGTTGCGAAAGA
R3c1	GAAGTTTCGAGGACTAAAGACTTTTATTAGCG
R5c-6	TTGCGGGAAAGAATACACTAAAACCCTGCTCC
R5c-2	AGGCTTTCATTAAACGGGTAAACCAACTTT
R5c3	AACCAGAGGTCAGACTGTAGCGCGCGATTGAG
R17c-6	ATTTTTGAAATTGTAAACGTTAATTAGCCAGC
R17c-2	TCGATGATGTACCCCGGTTGATAAACGGCG
R17c3	GACGCTGAGAGTGAATAACCTTGCTTTACATC
R19c-8	ATAATTCTGGTGCCGGAAACCAACTGTTGG
R19c-4	ACCCGTCGGGGGACGACGACAGTATGTGCTGC
R19c1	TGCCAAGCACGACGTTGTAAAACGAGTATTAG
R19c5	TTGAATAGGAAGGGTTAGAACCTTTAAAAG
R21c-6	TACGCCAGGTCATAGCTGTTTCCTCATTAATT
R21c3	ATCCTTTGACTAATAGATTAGAGCGAAGATAA

Table 2.9: Circuit components for dual rail two-input XNOR domino gate

Component	Domains (5′-3′)	Sequence (5′-3′)
Input hairpin-Ao	polyT ao* s* f s	TTTTT CCTCTA CCTATTCGCTGC AGTAGG GCAGCGAATAGG
Input hairpin-Bo	polyT bo* s* f s	TTTTT AGTGCT CCTATTCGCTGC AGTAGG GCAGCGAATAGG
Input hairpin-A1	polyT do* s* f s	TTTTT ACTAAT CCTATTCGCTGC AGTAGG GCAGCGAATAGG
Input hairpin-B1	polyT eo* s* f s	TTTTT TTAGCG CCTATTCGCTGC AGTAGG GCAGCGAATAGG
Intermediate hairpin	polyT xs* s* f s	TTTTT GAC CCTATTCGCTGC AGTAGG GCAGCGAATAGG
Threshold hairpin	polyT x* s* w s	TTTTT CTGGAC CCTATTCGCTGC ACGTCA GCAGCGAATAGG
Output hairpin-Co	polyT xs* s* y2 s t2	TTTTT GAC CCTATTCGCTGC CTCATT GCAGCGAATAGG ACTTTG
Output hairpin-C1	polyT xs* s* y s t2	TTTTT GAC CCTATTCGCTGC CAATCA GCAGCGAATAGG ACTTTG
Fuel	s x s* f*	GCAGCGAATAGG GTCCAG CCTATTCGCTGC CCTACT
Input-Ao	s ao	GCAGCGAATAGG TAGAGG
Input-Bo	s bo	GCAGCGAATAGG AGCACT
Input-A1	s do	GCAGCGAATAGG ATTAGT
Input-B1	s eo	GCAGCGAATAGG CGCTAA
Threshold block strand1	s* w*	CCTATTCGCTGC TGACGT
Threshold block strand2	s	GCAGCGAATAGG
Reporter-Co fluorophore strand	Cy5 t2* s* y2*	/5Cy5/ CAAAGT CCTATTCGCTGC AATGAG
Reporter-Co quencher strand	s t2 RQ	GCAGCGAATAGG ACTTTG /3IAbRQSp/
Reporter-C1 fluorophore strand	FAM t2* s* y*	/56-FAM/ CAAAGT CCTATTCGCTGC TGATTG
Reporter-C1 quencher strand	s t2 FQ	GCAGCGAATAGG ACTTTG /3IABkFQ/

Acknowledgements We thank K. Strauss and L. Ceze for their support in initiating this project, and F. Randisi for assistance with oxDNA simulations. This work was supported by NSF grants CCF-1409831, CCF-1317653 and HCC-1212940 and ONR grant N00014-13-1-0880 to G.S. G.C. was partially supported Microsoft Research Ltd.

Author contributions G.C., N. D., R.M., A.P. and G.S. designed experiments and wrote the paper. G.C. performed the experiments. N.D. and A.P. performed the modeling studies.

Chapter 3

LIVE-CELL MRNA DETECTION USING NUCLEIC ACID STRAND DISPLACEMENT

In order to use artificial nucleic-acid nanostructures for in vivo applications, the structures should be stable inside cells under physiological conditions and there should control over intercellular localization of the complexes upon delivery. Chen et al.[1] recently published a comprehensive study of the effect chemical modifications and delivery methods for efficient operation of nucleic acid complexes inside cells using strand displacement. We built on that work to categorically test and design modified RNA-based strand displacement probes which can interact with intracellular mRNAs in living mammalian cells. We modified the probe structures and sequences to facilitate cytoplasmic localization, probe stability and efficient interaction with probe target sites on the intracellular transcribed mRNAs. Yuan-Jyue Chen and I performed the experiments. This is still an ongoing project, and the work presented here a draft version of the manuscript. The final version may change significantly.

Gourab Chatterjee, Yuan-Jyue Chen, Georg Seelig.(2017) "Live-cell mRNA detection using nucleic acid strand displacement"

3.1 Abstract

The intricate dynamic balance between the relative expression levels of different RNAs after transcription plays a major role in defining cellular identity and establishes synergy between different yet genetically identical cells in an organism. Accurate detection of the

spatio-temporal dynamics of intracellular RNAs at the single-cell level can provide valuable insights about gene stochasticity and evolution of genetic diseases. Molecular probes developed to detect intracellular RNAs in living cells till date, operate primarily through one-step nucleic acid hybridization which limits their applicability towards conditional molecular analysis involving multiple intracellular targets. Nucleic acid strand displacement has emerged as a powerful mechanism for building molecular circuits capable of complex multi-parametric molecular information processing. Here, we use nucleic acid strand displacement as the underlying principle to experimentally demonstrate a novel strand displacement probe design for detection of intracellular mRNAs in living mammalian cells. We present a modified molecular probe structure for optimal strand displacement kinetics, probe stability and efficient cytoplasmic localization. We also show that the strand displacement probes can be used to reliably quantify and perform real-time visualization of genetically engineered intracellular mRNAs in living cells. We believe this study will provide fundamental guidelines to researchers interested in building complex molecular diagnostic systems for multi-parametric detection and analysis in mammalian cells.

3.2 Introduction

The fundamental steps of the central dogma[115] of molecular biology: transcription and translation; universally determines the biological complexities of the diverse species of organisms known so far. RNA expression, post-transcriptional modifications, and the spatio-temporal dynamics of coding and non-coding RNAs majorly steer the critical bio-processes responsible for cell phenotype[116, 117], cell state[118, 119], cell function[120] and intercellular communication[121]. A detailed understanding of the biogenesis of different RNAs also becomes critical towards understanding the evolution of various genetic

diseases[122, 123]. Widely-practiced molecular biology techniques like polymerase chain reaction (PCR)[124], microarray analysis[125, 126], northern blot[127] and flow cytometry[128] provide valuable information on RNA expression levels, but these bulk measurement based approaches often fail to capture the dynamic behavior of gene expression at the single cell level and neglect cell-to-cell variability.

Recent advancements in this field has led to the development of a number of single-cell imaging platforms for molecular detection: small molecule fluorescence in situ hybridization (smFISH)[129, 130], multiplexed molecular barcoding[131], single-cell reverse transcription polymerase chain reaction (RT-PCR)[132, 133], MS2-GFP fusion protein based detection[134] and molecular beacons[135, 136]. Endogenous mRNA detection studies with smFISH has yielded valuable insights on spatial intracellular dynamics including mRNA stability and transcriptional bursting. Recently emerging multiplexed molecular barcoding techniques[137, 138] can be very useful for high-throughput detection of multiple RNAs. But, since these techniques can only be performed with either fixed cells or extracted RNA pools, they lacks the ability of real-time monitoring and thus studying the temporal RNA dynamics. Single-cell RT-PCR methods can be used to detect endogenous mRNAs with low copy numbers, but these methods also fail to yield the spatio-temporal dynamics of RNAs and are known to have inconsistent efficiencies. Multiple MS2-GFP fusion proteins can localize on specific mRNAs engineered to carry tandem repeats of MS2 binding sites at 3'-untranslated region (UTR) and generate bright fluorescent spots detectable via fluorescence microscopy. Although this method has provided invaluable details on spatio-temporal dynamics of intracellular RNA localization and processing through real-time visualization, but the the high background fluorescence signal of GFPs was shown to be a significant drawback limiting its sensitivity[139]. This problem was tackled with the use of molecular probes because of their minimal background fluores-

cence and high signal-to-noise ratio. Although molecular probes have been extensively used for live-cell imaging over recent times, but there has been significant concerns about poor probe sensitivities majorly due to high nuclear localization of the probes, giving rise to false-positive signals.

Recent studies with ratiometric bimolecular beacons (RBMB) have demonstrated its potential for highly accurate intracellular mRNA detection in living cells[16, 140]. By design, RBMBs facilitate extranuclear transport[141, 142] and effectively localize in the cytoplasm through electroporation mediated delivery[143], where they interact with the genetically engineered probe target sites at the 3'-UTR of specific mRNAs exhibiting high signal-to-noise ratio. RBMBs have been demonstrated for one-step detection of intracellular mRNAs in living cells primarily through nucleic acid hybridization. But, potential issues with fluorophore quenching due to dye-dye and dye-quencher interactions between multiple RBMBs have also been noted due to the hairpin-shaped probe designs. A strand-displacement based molecular probe where the quencher is displaced away from the probe upon activation, can overcome such drawbacks. Also, interaction between molecular probes and intracellular targets through strand displacement can also facilitate multi-parametric molecular detection and expand the applications of molecular probes for live-cell imaging. Recently, our colleagues has demonstrated molecular logic circuits in mammalian cells using strand displacement and used them to conditionally activate RNAi[1]. Here we report the first evidence of using nucleic acid strand displacement for detection of endogenously transcribed mRNAs in living mammalian cells. Our categorically modified strand displacement probes facilitate nuclear export and localize on cytoplasmic mRNA transcripts in genetically engineered living mammalian cells, facilitating real-time detection. (Fig. 3.1).

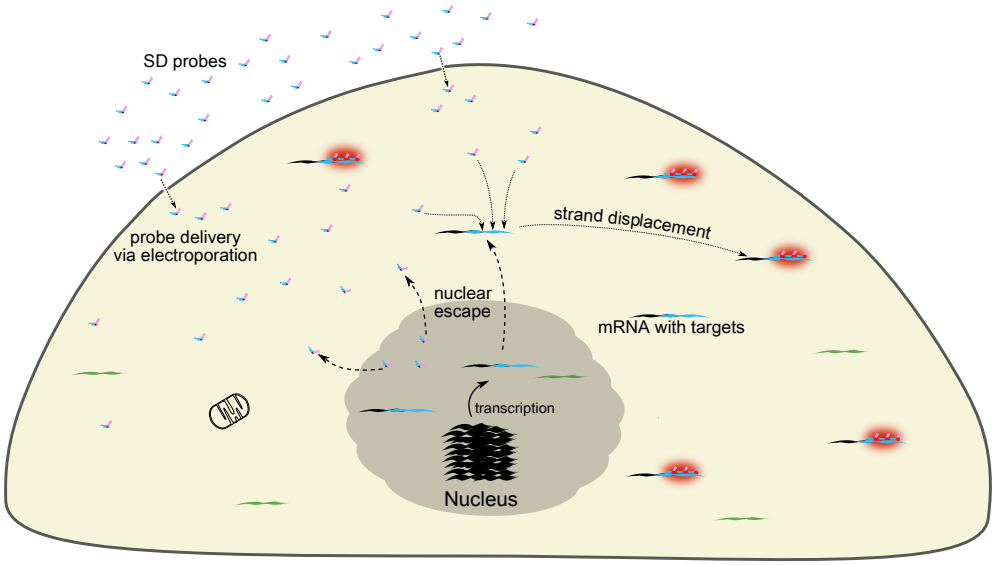

Figure 3.1: Schematic overview of mRNA detection using strand displacement probes.

3.3 Experimental setup and Results

We used genetically-engineered variants of human fibroblastoma cells (HT1080) for our studies. The HT1080-96X cells were engineered to carry 96 tandem repeats of the probe target sequences at the 3′-UTR of the endogenously transcribed GFP mRNA. As a control, we used HT1080-control cells which endogenously transcribed GFP mRNA with no target sites. Due to the proximal localization of multiple unquenched fluorophores at the 3′-UTR target sites of HT1080-96X cells, the signal to background ratio should be significantly improved and the resultant output fluorescence should be detectable under conventional fluorescence microscope (Fig. 3.4(). Indeed, using fluorescence in situ hybridization (FISH), single transcripts expressed in HT1080-96X cells were detectable as bright fluorescent spots (data not shown). In contrast, the HT1080-control cells showed primarily background fluorescence.

We initially designed the strand displacement probe (SDProbe-v0) as a partially double stranded complex with a single stranded toehold and double stranded stem domain (Fig. 3.2,a). The probe comprised of a fluorophore-labeled strand (26 nucleotide long) complementary to a section of the target site at the 3′-UTR of the mRNA of interest and was partially blocked by a complementary quencher-labeled strand. The fluorophore-labeled strand could interact with the target-site at the 3′-UTR of the mRNA via the flanking toehold domain and initiate a three-way branch migration thereby displacing the quencher-labeled strand. The displacement of the quencher-labeled strand should result in unquenching of the fluorophore and generate output fluorescence (Fig. 3.2,a). We varied the lengths of the toehold and stem domains (ds12-t14: 12nt stem-14nt toehold, ds16-t10: 16nt stem-10nt toehold, ds18-t8: 18nt stem-8nt toehold) to observe their effects on in vivo probe stability and intracellular localization. The dst12-t14 and ds16-t10 probes were observed to be primarily localized inside the nucleus(Fig. 3.2,b). This can

be expected due to the fact that complexes with shorter stem domains are more prone to get dissociated and also tend to get localized in the nucleus upon delivery with minimal nuclear export. Although the ds18-t8 probes showed minimal nuclear localization, the probes also had significantly less interaction with the cytoplasmic GFP mRNAs and they rather seemed to form intracellular aggregates, suggesting the need of probe redesign (Fig. 3.2,b).

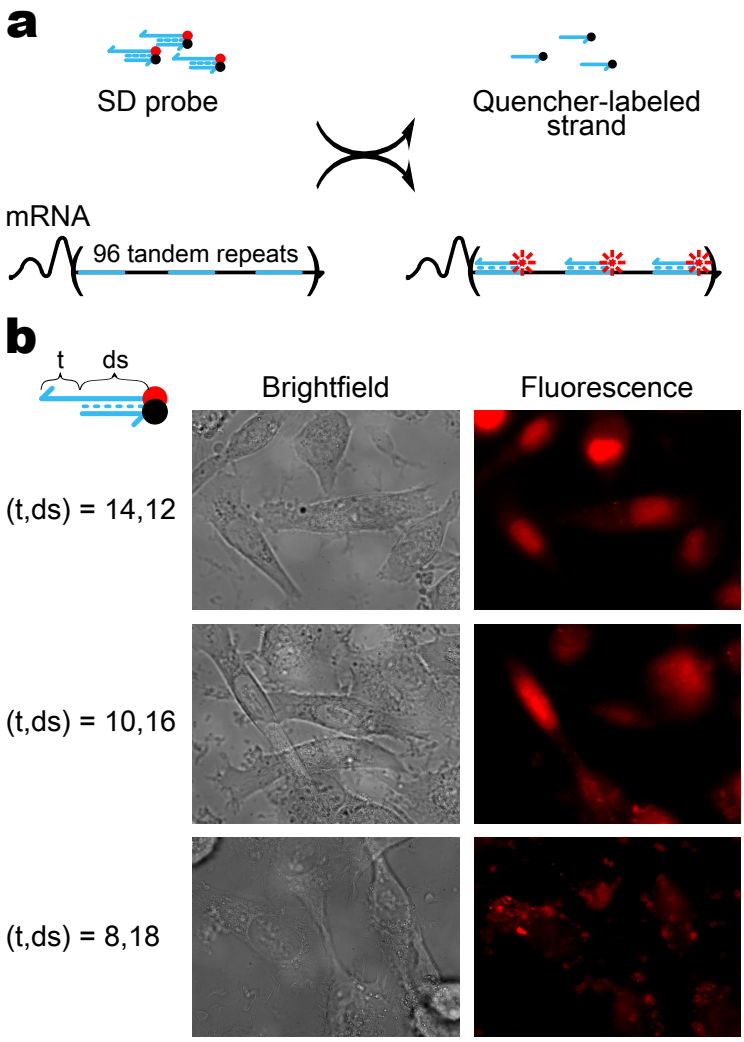

Figure 3.2: Intracellular mRNA detection using strand displacement probes (first design). a) Intended interaction mechanism with 3′-UTR target sites of mRNA. **b)** Representative brightfield and fluorescence channel (TRITC) images of cells electroporated with different variants of the strand displacement probe SDProbe-v0. The structural details of each variant is shown in the left: t is the toehold length and ds is the double stranded stem domain length of the probe in each case.

To improve in vivo strand displacement kinetics and facilitate nuclear escape to increase cytoplasmic localization, we modified the probe design. The redesigned strand displacement probe (SDProbe-v1) was a nicked partially double stranded complex with an interaction domain and an extension domain (Fig. 3.3). The interaction domain can bind to the target site sequence at the 3-UTR through a toehold (8 nucleotide long) mediated strand displacement reaction and release the quencher-labeled strand (18 nucleotide long; Fig. 3.5,a). The extension domain consists of a 22 nucleotide long double stranded region with a 5-fluorophore labeled strand. Longer double stranded nucleic acid complexes have been reported to be preferentially exported outside the nucleus via exportin-mediated pathways. The extension domain was included to the probe to increase cytoplasmic localization by facilitating nuclear escape and also for keeping the probe design scalable for cascading multiple strand displacement reactions towards complex molecular logic. As per the probe design, the release of the quencher-labeled strand un-quenches the fluorophore and generates output fluorescence.

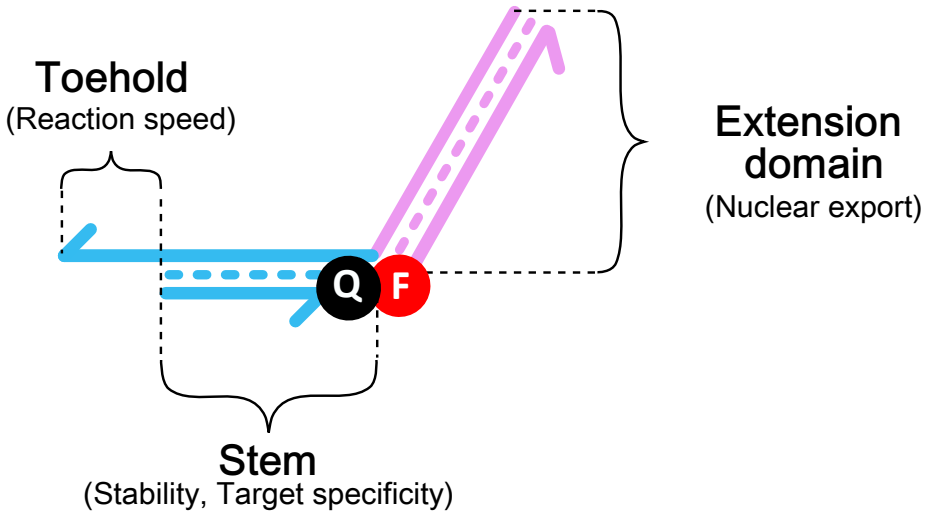

Figure 3.3: Schematic domain-level representation of the strand displacement probe. Individual domains are annotated (in bold) with their respective primary functions in parentheses. Half-arrows indicate 3-ends of the corresponding strands. The toehold and stem domains together constitute the interaction domain (blue). The Fluorophore and Quencher are denoted by red and black circles respectively.

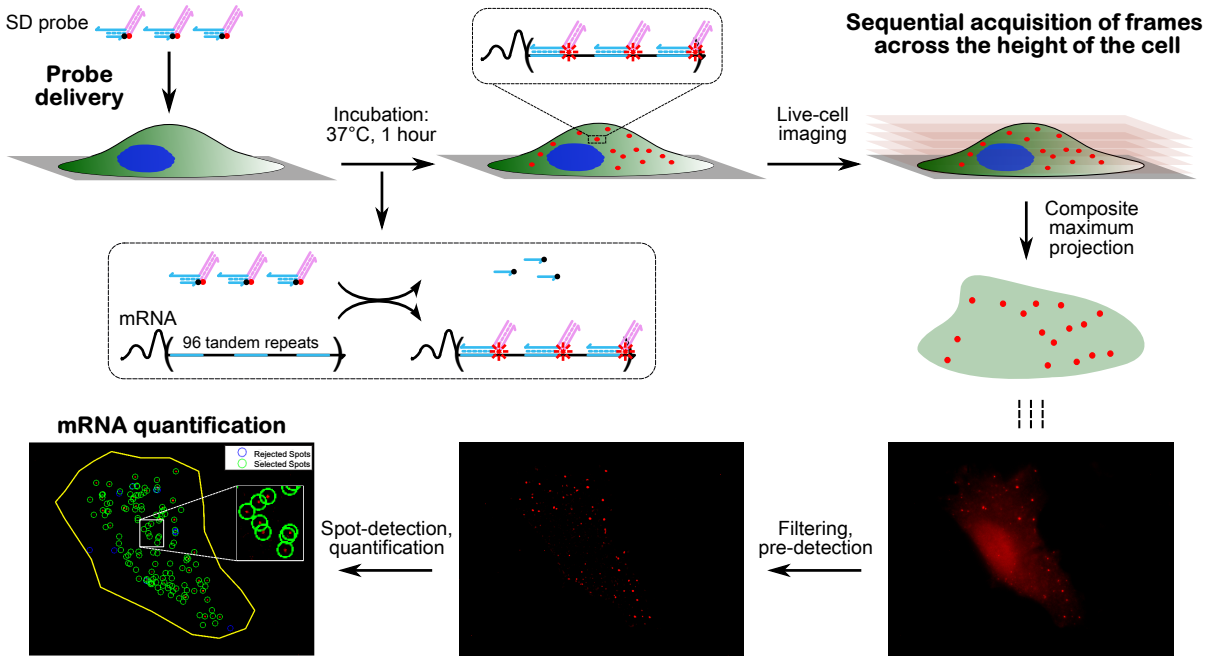

Figure 3.4: Experimental workflow for detection of mRNAs using strand displacement probes. SD probes are delivered via electroporation to the cultured cells and the cells are incubated for 1 hour at 37C allowing the probes to interact with the intracellular mRNA target sites via strand displacement. The co-localization of several probes at each mRNA generates a bright fluorescent spot detectable with fluorescence microscopy. After incubation, sequential image frames are collected at every 0.3 um z-distance across the cell height and the acquired frames are combined to generate maximum intensity projection composite images representing the entire cell volume. These images are processed using FISH-Quant Matlab tool, where a filtering step performs background signal correction and spots are pre-detected based on a threshold signal cut-off. The pre-detected spots are then fitted and examined for accuracy followed by spot quantification, where the spots are either selected or rejected based on signal intensity and elimination of false-positives. The selected spots represent the number of detected mRNAs per cell.

Upon delivery to HT1080-96X cells via electroporation, the SDProbe-v1 probes were effectively transported to the cytoplasmic space and they localized at the 3'-UTR of GFP mRNAs, observable by small distinct fluorescent spots throughout the cells (Mean: 131.35 per cell; Fig. 3.4, Fig. 3.5,a) In contrast, when these probes were electroporated to HT1080-control cells, there was significantly less number of observable spots (Mean: 29.85 per cell; Fig. 3.5,b) This showed that SDprobe-v1 probes can be effectively used to detect intracellular mRNAs via the 3'-UTR target sites. The residual fluorescent spots observed in the HT1080-control cells were possibly due to partial degradation of the probes in the intracellular environment. Control experiments were performed where HT1080-96X cells were electroporated with probe variants having orthogonal toeholds and double-stranded stem domains corresponding to the target sites. For each of these cases, there were minimal activation of the fluorophores (Mean: 12.25 per cell and 10.45 per cell respectively), which showed that the probes had minimal non-specific interaction within the intracellular environment (Fig. 3.5,c, 3.5,d).

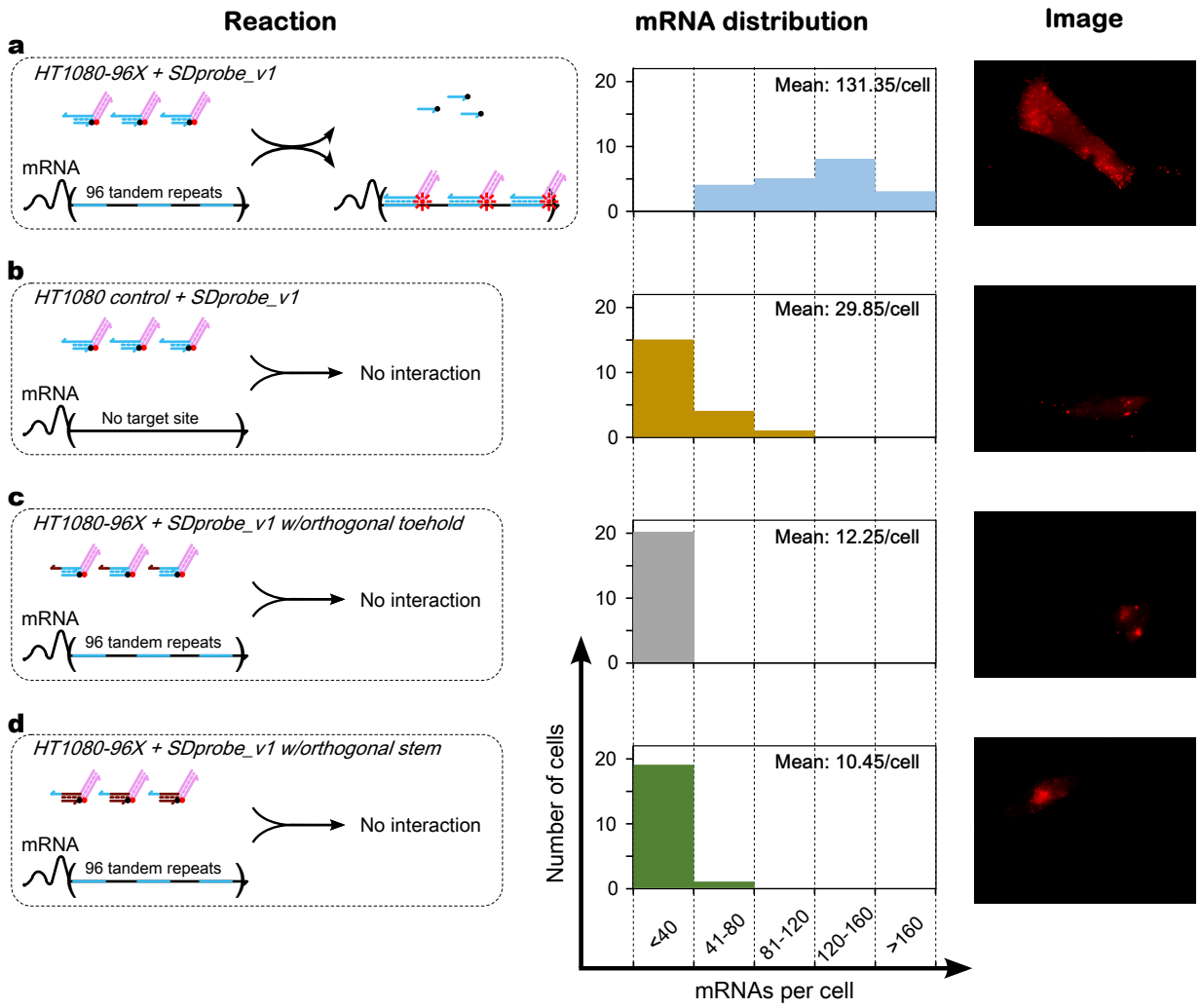

Figure 3.5: Intracellular mRNA quantification using strand displacement probes. Each row demonstrates the reaction mechanism for interaction of probes with mRNAs **(left)**, histogram of detected mRNAs per cell **(middle)** and representative unprocessed image **(right)**. For quantifying the distribution of detected mRNAs per cell, 20 randomly selected cells were imaged for each of the four different conditions: SDProbe-v1 probes were electroporated to **a)** HT1080-96X cells endogenously transcribing GFP mRNAs with 96 tandem repeats of probe target sites at 3′-UTR,**b)** HT1080-control cells transcribing GFP mRNAs with no probe target sites. HT1080-96x cells were electroporated with SD control probes similar to SDProbe-v1 but with **c)** a toehold orthogonal to the corresponding section of the probe target sequence, and **d)** a double stranded stem domain orthogonal to the probe target sequence.For each case, the mean number of spots detected per cell is shown as inset to the histograms.

Strand displacement probes can also be used to track the spatio-temporal dynamics of intracellular mRNAs in living cells. Probe synthesis with chemically modified bases makes the probes more resistant to intracellular degradation and increases their ability to remain bound with intracellular mRNAs for longer time intervals. Using the SDprobe-v1 probes we were able to observe the intracellular movement of GFP mRNAs transcribed with the 3'-UTR 96 target sites in HT1080-96X cells (Supplementary movie 1: available online or upon request).

3.4 Discussion

In this study, we use nucleic acid strand displacement as a primary interaction mechanism for detecting endogenously expressed mRNAs in living mammalian cells. With minor technical improvements, this kind of approach can be used as a more generalizable platform for single-cell molecular imaging. For example, the Alexa fluor dyes in the strand displacement probes provide higher photo-resistance, but we still noticed photo-bleaching of the fluorophores during our real-time monitoring experiments with the HT1080 cells. Also, we noticed some spots in HT1080-control cells with SDprobe-v1 probes, possibly due to partial degradation or non-specific interactions in the intracellular environment. Use of more photo-resistant inorganic fluorophores like Quantum dots[144] can significantly reduce photobleaching and increase in vivo probe stability. Alternatively, photostability can be increased by the use of fluorescence amplifying conjugated polymers[145] or self-healing dyes[146] with triplet-state quenchers, which can extend the fluorophore lifetimes without compromising signal amplification. Secondly, with the current approach, the cells need to be genetically modified to express a specific mRNA with tandem repeats of the target sites. This limits the applicability of the current method in the sense that in order to detect any specific mRNA, it has to be engineered

to include the target sites first. A signal amplification architecture[22] can be useful for accurate detection of intracellular mRNAs requiring a single copy of target site for initiation. Although strand displacement interactions between complexes with secondary structures can be significantly slow, but modifications like the use of spatial localization can dramatically improve reaction speed and make such architectures feasible for in vivo use with realistic experimental time frames.

Here, we have shown a basic module of strand displacement probes which can effectively detect endogenously transcribed mRNAs in the cytoplasm of living mammalian cells. In the future, multiple modules detecting different intracellular mRNAs can be connected downstream for more specialized analysis using molecular logic. The simplicity, scalability and robustness of circuit design with strand displacement[7, 107] opens up the possibilities of a wide range of applications for multi-parameter molecular detection in living cells. We believe the results presented here will act as as a pilot study for future research towards multiplexed molecular detection in living cells using strand displacement.

3.5 Materials and Methods

3.5.1 Probe design

The HT1080-96X and HT0180-control cell lines were kindly shared with us by Andrew Tsourkas. The strand displacement probes were designed to interact with each of the 96 tandem repeat target sequences at the 3′-UTR of the GFP mRNA in the genetically engineered HT1080-96X cells. The target sequence was: 5′-CAGGAGUUGUGUUUGUGGA CGAAGAGCACCAGCCAGCUGAUCGACCUCGA-3′.

Each of the SDProbe-v0 probes consisted of two 2′-O-methylated RNA oligonucleotide sequences which were annealed together to form the probe complex. All the probes had a common fluorophore-labeled strand (26 nucleotide long), which was complementary to a section of the target sequence and was labeled with an Alexa®-546 reporter dye at the 5′-end. The second sequence for each of the probe variants was labeled with an Iowa Black®RQ-Sp quencher dye at the 3′-end. The SDProbe-v1 probes consisted of three 2′-O-methylated strands, which were annealed together to generate the interaction and extension domains, as described before (Fig. 3.3). The fluorophore-labeled strand was a 22 nucleotide long sequence with an Alexa®-546 dye at 5′-end, while the 18 nucleotide long quencher-labeled strand with an Iowa Black®RQ-Sp quencher dye at the 3′-end. These two sequences were localized such that the fluorophore and the quencher are in close proximity by a 48 nucleotide long assembling strand. The proximal placement of fluorophore and quencher upon annealing, resulted in quenching of the fluorophore in the inactive state of the probe. For control experiments, probe with orthogonal toehold was designed with the same fluorophore-labeled strand and quencher-labeled strands as SDProbe-v1, but with the assembling strand having the orthogonal toehold. Similarly, probe with orthogonal stem domain was designed by keeping the same fluorophore-

labeled strand, an orthogonal quencher-labeled strand and corresponding assembling strand.

The corresponding sequences are as follows:

Table 3.1: Sequences for different strand displacement probes used for mRNA detection studies

Probe	Component strand	Sequence (5′ - 3′)
SDProbe-v0	Fluorophore strand	/A546/mUmCmAmGmCmUmGmGmCmU mGmGmUmGmCmUmCmUmUmCmGmUm-CmCmAmC
	Quencher strand: ds12-t14	mCmCmAmGmCmCmAmGmCmU mGmA/3IAbRQSp/
	Quencher strand: ds16-t10	mAmGmCmAmCmCmAmGmCmC mAmGm-CmUmGmA/3IAbRQSp/
	Quencher strand: ds18-t8	mAmGmAmGmCmAmCmCmAmGmC mC-mAmGmCmUmGmA/3IAbRQSp/
SDProbe-v1	Fluorophore strand	/A546/mGmUmAmAmGmAmGmAmAmG mGmAmmGmUmGmGmAmGmGmUmGmA
	Quencher strand	mAmGmAmGmCmAmCmCmAmGmCmC mAmGmCmUmGmA/3IAbRQSp/
	Assembly strand	mUmCmAmCmCmUmCmCmAmCmU mCm-CmUmUmCmUmCmUmUmAmCmUmC-mAmGmCmUmGmGmC mUmGmGmUmGm-CmUmCmUmUmCmGmUmCmCmAmC
SDProbe-v1: orthogonal toehold	Fluorophore strand	/A546/mGmUmAmAmGmAmGmAmAmG mGmAmmGmUmGmGmAmGmGmUmGmA
	Quencher strand	mAmGmAmGmCmAmCmCmAmGmCmC mAmGmCmUmGmA/3IAbRQSp/
	Assembly strand	mUmCmAmCmCmUmCmCmAmCmU mCm-CmUmUmCmUmCmUmUmAmCmUmC-mAmGmCmUmGmGmC mUmGmGmUmGm-CmUmCmUmAmUmAmGmCmAmUmU
SDProbe-v1: orthogonal stem	Fluorophore strand	/A546/mGmUmAmAmGmAmGmAmAmG mGmAmmGmUmGmGmAmGmGmUmGmA
	Quencher strand	mGmUmAmAmUmUmGmUmUmGmCmG mCmAmCmAmUmU/3IAbRQSp/
	Assembly strand	mUmCmAmCmCmUmCmCmAmCmU mCm-CmUmUmCmUmCmUmUmAmCmAmA-mUmGmUmGmCmGmC mAmAmCmAmA-mUmUmAmCmUmCmGmUmCmCmAmC

3.5.2 Probe delivery via electroporation

24 hours before experiments, HT1080-96X and HT1080-control cells were subcultured at 40-50% confluency in DMEM growth medium supplemented with 10% fetal bovine serum (FBS) and 1% Penicillin/Streptomycin antibiotics at 37°C with 5% CO2. 24 well plates (The growth medium was then aspirated and the cells were washed once with 1X DPBS (Ca^{++} and Mg^{++} free). The cells were then incubated at 37°C for 2-3 minutes (min) with 1 ml of 1X TrypLE^{TM} Express. The cell dissociation process was stopped with 1 ml of DMEM supplemented with 10% FBS without antibiotics and phenol red. The suspended cells were spun down at 200 g for 5 min at room temperature. The supernatants were aspirated and the cells were resuspended using 1 mL DPBS with 10% FBS and the cell densities were counted using a haemocytometer or a flow cytometer. For each electroporation, 150,000 cells were transferred to a 1.5 mL eppendorf tube and spun down at 200 g for 5 min. The supernatant was then aspirated and resuspended with 22 μ L resuspension buffer. Then, 2.4 μL of the probe (12 μM stock) was mixed with the suspension by gentle pipetting while avoiding any air bubbles. 10 μL of the probe-cell mix was then collected for electroporation with a Neon®Transfection System using a 10 μL Electroporation pipette tip. The cells were electroporated with 2 pulses of 950 Volts and 25 milliseconds each. The electroporated samples were suspended into 1 mL DMEM media with FBS but without antibiotics and phenol-red, by inverting it several times. The cells were then spun down at 200 g for 5 min, following the removal of the supernatant and resuspension in fresh 1 mL DMEM with FBS but without antibiotics and phenol-red. The cells were washed by repeating this process twice. Ultimately the cells were resuspended in 400 μL DMEM media with 10% FBS without antibiotics and phenol red and plated on a ECM-coated Greiner Bio-One SensoPlate^{TM} 24-well plate. The plated cells were incubated at 37°C with 5% CO2 for at least 1 hour before imaging.

3.5.3 Fluorescence Microscopy

The electroporated cells were imaged with an inverted Nikon Eclipse Ti microscope with a 100X, NA 1.4 oil objective with a TRITC bandpass filter (Nikon) operating on the NIS Elements Advanced Research Imaging software (Nikon). For the mRNA quantification experiments, sequential images were acquired at intervals of 0.3 μm with exposure time of 1 second across each cell height over a total z-range of 6 μm (+/- 3μm), to create corresponding z-stacks using the ND Acquisition Tool. For the real-time visualization experiments, movies were acquired with the Timelapse acquisition tool using the same settings as described above.

3.5.4 Quantification of mRNAs

2D composite maximum intensity projection images were generated from the acquired frames in the z-stacks. The total number of mRNAs was quantified using the FISH-quant MATLAB tool[147]. A detailed schematic representation of the image processing workflow is presented in Fig. 3.4.

BIBLIOGRAPHY

[1] Chen, Y. J., Groves, B., Muscat, R. A. & Seelig, G. DNA nanotechnology from the test tube to the cell. *Nature Nanotechnology* **10**, 748–760 (2015).

[2] Walsh, A. S., Yin, H., Erben, C. M., Wood, M. J. & Turberfield, A. J. Dna cage delivery to mammalian cells. *ACS nano* **5**, 5427–5432 (2011).

[3] Seeman, N. C. Nanomaterials based on dna. *Annual review of biochemistry* **79**, 65–87 (2010).

[4] Endo, M., Yang, Y. & Sugiyama, H. Dna origami technology for biomaterials applications. *Biomaterials Science* **1**, 347–360 (2013).

[5] Bath, J. & Turberfield, A. J. Dna nanomachines. *Nature nanotechnology* **2**, 275–284 (2007).

[6] Liu, H. & Liu, D. Dna nanomachines and their functional evolution. *Chemical Communications* 2625–2636 (2009).

[7] Zhang, D. Y. & Seelig, G. Dynamic DNA nanotechnology using strand-displacement reactions. *Nature Chemistry* **3**, 103–113 (2011). NIHMS150003.

[8] Keefe, A. D., Pai, S. & Ellington, A. Aptamers as therapeutics. *Nature reviews Drug discovery* **9**, 537–550 (2010).

[9] Rudchenko, M. *et al.* Autonomous molecular cascades for evaluation of cell surfaces. *Nature nanotechnology* **8**, 580–586 (2013).

[10] Douglas, S. M., Bachelet, I. & Church, G. M. A logic-gated nanorobot for targeted transport of molecular payloads. *Science (New York, N.Y.)* **335**, 831–4 (2012).

[11] Ko, S., Liu, H., Chen, Y. & Mao, C. Dna nanotubes as combinatorial vehicles for cellular delivery. *Biomacromolecules* **9**, 3039–3043 (2008).

[12] Schuller, V. J. *et al.* Cellular immunostimulation by cpg-sequence-coated dna origami structures. *ACS nano* **5**, 9696–9702 (2011).

[13] Mikkila, J. *et al.* Virus-encapsulated dna origami nanostructures for cellular delivery. *Nano letters* **14**, 2196–2200 (2014).

[14] Modi, S. *et al.* A dna nanomachine that maps spatial and temporal ph changes inside living cells. *Nature Nanotechnology* **4**, 325–330 (2009).

[15] Modi, S., Nizak, C., Surana, S., Halder, S. & Krishnan, Y. Two dna nanomachines map ph changes along intersecting endocytic pathways inside the same cell. *Nature nanotechnology* **8**, 459–467 (2013).

[16] Chen, A. K., Davydenko, O., Behlke, M. A. & Tsourkas, A. Ratiometric bimolecular beacons for the sensitive detection of rna in single living cells. *Nucleic acids research* gkq436 (2010).

[17] Afonin, K. A. *et al.* Activation of different split functionalities on re-association of RNA-DNA hybrids. *Nat Nanotechnol* **8**, 296–304 (2013).

[18] Hochrein, L. M., Schwarzkopf, M., Shahgholi, M., Yin, P. & Pierce, N. A. Conditional dicer substrate formation via shape and sequence transduction with small conditional RNAs. *J. Am. Chem. Soc.* **135**, 17322–30 (2013).

[19] Kumar, D., Kim, S. H. & Yokobayashi, Y. Combinatorially inducible RNA interference triggered by chemically modified oligonucleotides. *J. Am. Chem. Soc.* **133**, 2783–8 (2011).

[20] Hemphill, J. & Deiters, A. DNA computation in mammalian cells: MicroRNA logic operations. *Journal of the American Chemical Society* **135**, 10512–10518 (2013).

[21] Mei, Q. *et al.* Stability of DNA origami nanoarrays in cell lysate. *Nano Lett.* **11**, 1477–82 (2011).

[22] Choi, H. M. *et al.* Programmable in situ amplification for multiplexed imaging of mrna expression. *Nature biotechnology* **28**, 1208–1212 (2010).

[23] Levesque, M. J., Ginart, P., Wei, Y. & Raj, A. Visualizing SNVs to quantify allele-specific expression in single cells. *Nat. Methods* **10**, 865–7 (2013).

[24] Yurke, B., Turberfield, a. J., Mills, a. P., Simmel, F. C. & Neumann, J. L. A DNA-fuelled molecular machine made of DNA. *Nature* **406**, 605–608 (2000).

[25] Simmel, F. & Yurke, B. Using DNA to construct and power a nanoactuator. *Phys Rev E Stat Nonlin Soft Matter Phys* **63**, 041913 (2001).

[26] Chhabra, R., Sharma, J., Liu, Y. & Yan, H. Addressable molecular tweezers for DNA-templated coupling reactions. *Nano Lett.* **6**, 978–83 (2006).

[27] Shen, W., Bruist, M. F., Goodman, S. D. & Seeman, N. C. A protein-driven DNA device that measures the excess binding energy of proteins that distort DNA. *Angew. Chem. Int. Ed. Engl.* **43**, 4750–2 (2004).

[28] Seelig, G., Soloveichik, D., Zhang, D. Y. & Winfree, E. Enzyme-free nucleic acid logic circuits. *Science (New York, N.Y.)* **314**, 1585–8 (2006).

[29] Qian, L. & Winfree, E. A simple DNA gate motif for synthesizing large-scale circuits. *J R Soc Interface* **8**, 1281–97 (2011).

[30] Soloveichik, D., Seelig, G. & Winfree, E. DNA as a universal substrate for chemical kinetics. *Proceedings of the National Academy of Sciences* **107**, 5393–5398 (2010).

[31] Zhang, D. Y., Chen, S. X. & Yin, P. Optimizing the specificity of nucleic acid hybridization. *Nat Chem* **4**, 208–14 (2012).

[32] Turberfield, A. *et al.* DNA fuel for free-running nanomachines. *Phys. Rev. Lett.* **90**, 118102 (2003).

[33] Seelig, G., Yurke, B. & Winfree, E. Catalyzed relaxation of a metastable DNA fuel. *J. Am. Chem. Soc.* **128**, 12211–20 (2006).

[34] Green, S. J., Lubrich, D. & Turberfield, A. J. DNA hairpins: fuel for autonomous DNA devices. *Biophys. J.* **91**, 2966–75 (2006).

[35] Dirks, R. M. & Pierce, N. a. Triggered amplification by hybridization chain reaction. *Proceedings of the National Academy of Sciences of the United States of America* **101**, 15275–8 (2004).

[36] Muscat, R. A., Strauss, K., Ceze, L. & Seelig, G. Dna-based molecular architecture with spatially localized components. *SIGARCH Comput. Archit. News* **41**, 177–188 (2013).

[37] Zhang, D., Turberfield, A. J., Yurke, B. & Winfree, E. Engineering Entropy-Driven reactions and networks catalyzed by DNA. *Science* **318**, 1121–1125 (2007).

[38] Zhang, D. Y. & Winfree, E. Dynamic allosteric control of noncovalent DNA catalysis reactions. *J. Am. Chem. Soc.* **130**, 13921–6 (2008).

[39] Qian, L. & Winfree, E. Scaling up digital circuit computation with DNA strand displacement cascades. *Science (New York, N.Y.)* **332**, 1196–201 (2011).

[40] Chen, S. X., Zhang, D. Y. & Seelig, G. Conditionally fluorescent molecular probes for detecting single base changes in double-stranded DNA. *Nat Chem* **5**, 782–9 (2013).

[41] Zhou, L., Marras, A. E., Su, H. J. & Castro, C. E. DNA origami compliant nanostructures with tunable mechanical properties. *ACS Nano* **8**, 27–34 (2014).

[42] Seeman, N. Nucleic acid junctions and lattices. *J. Theor. Biol.* **99**, 237–47 (1982).

[43] Winfree, E., Liu, F., Wenzler, L. & Seeman, N. Design and self-assembly of two-dimensional DNA crystals. *Nature* **394**, 539–44 (1998).

[44] Goodman, R. *et al.* Rapid chiral assembly of rigid DNA building blocks for molecular nanofabrication. *Science* **310**, 1661–5 (2005).

[45] Zheng, J. *et al.* From molecular to macroscopic via the rational design of a self-assembled 3D DNA crystal. *Nature* **461**, 74–7 (2009).

[46] Rothemund, P. W. K. Folding DNA to create nanoscale shapes and patterns. *Nature* **440**, 297–302 (2006). 0202466.

[47] Dietz, H., Douglas, S. M. & Shih, W. M. Folding DNA into twisted and curved nanoscale shapes. *Science* **325**, 725–30 (2009).

[48] Han, D. *et al.* DNA gridiron nanostructures based on four-arm junctions. *Science* **339**, 1412–5 (2013).

[49] Zhang, F., Nangreave, J., Liu, Y. & Yan, H. Structural DNA nanotechnology: state of the art and future perspective. *J. Am. Chem. Soc.* **136**, 11198–211 (2014).

[50] Funke, J. J. & Dietz, H. Placing molecules with bohr radius resolution using DNA origami. *Nat Nanotechnol* **11**, 47–52 (2016).

[51] Gerling, T., Wagenbauer, K. F., Neuner, A. M. & Dietz, H. Dynamic DNA devices and assemblies formed by shape-complementary, non-base pairing 3D components. *Science* **347**, 1446–52 (2015).

[52] Sherman, W. & Seeman, N. A precisely controlled DNA biped walking device. *Nano Letters* (2004).

[53] Shin, J. S. & Pierce, N. A. A synthetic DNA walker for molecular transport. *J. Am. Chem. Soc.* **126**, 10834–5 (2004).

[54] Yin, P., Yan, H., Daniell, X. G., Turberfield, A. J. & Reif, J. H. A unidirectional DNA walker that moves autonomously along a track. *Angewandte Chemie Int Ed* **43**, 4906–4911 (2004).

[55] Omabegho, T., Sha, R. & Seeman, N. C. A bipedal DNA brownian motor with coordinated legs. *Science* **324**, 67–71 (2009).

[56] Seeman, N. From genes to machines: DNA nanomechanical devices. *Trends in biochemical sciences* (2005).

[57] Simmel, F. Processive motion of bipedal DNA walkers. *ChemPhysChem* (2009).

[58] Venkataraman, S., Dirks, R. & Rothemund, P. An autonomous polymerization motor powered by DNA hybridization. *Nature* (2007).

[59] Simmel, F. C. & Dittmer, W. U. DNA nanodevices **1**, 284–299 (2005).

[60] Lund, K. *et al.* Molecular robots guided by prescriptive landscapes. *Nature* **465**, 206–10 (2010).

[61] Wickham, S. F. J. *et al.* A DNA-based molecular motor that can navigate a network of tracks. *Nature Nanotechnology* **7**, 169–73 (2012).

[62] Gu, H., Chao, J., Xiao, S.-J. & Seeman, N. C. A proximity-based programmable DNA nanoscale assembly line. *Nature* **465**, 202–205 (2010).

[63] Liber, M., Tomov, T. E., Tsukanov, R., Berger, Y. & Nir, E. A bipedal DNA motor that travels back and forth between two DNA origami tiles. *small* **11**, 568–575 (2015).

[64] Tomov, T., Tsukanov, R. & Liber, M. Rational design of DNA motors: fuel optimization through single-molecule fluorescence. *Journal of the* (2013).

[65] Zhou, C., Duan, X. & Liu, N. A plasmonic nanorod that walks on DNA origami. *Nature communications* (2015).

[66] Rajendran, A., Endo, M. & Sugiyama, H. SingleMolecule analysis using DNA origami. *Angew. Chem. Int. Ed. Engl.* **51**, 874–890 (2012).

[67] Jungmann, R., Avendaño, M., Dai, M. & Woehrstein, J. Quantitative superresolution imaging with qPAINT. *Nature* (2016).

[68] Qian, L., Winfree, E. & Bruck, J. Neural network computation with DNA strand displacement cascades. *Nature* **475**, 368–72 (2011).

[69] Chandran, H., Gopalkrishnan, N., Phillips, A. & Reif, J. *Localized Hybridization Circuits*, vol. 6937 (springer, 2011).

[70] Dalchau, N., Chandran, H., Gopalkrishnan, N., Phillips, A. & Reif, J. Probabilistic Analysis of Localized DNA Hybridization Circuits. *ACS Synthetic Biology* **4**, 898–913 (2015).

[71] O'Connell, C. B. & Khodjakov, A. L. Cooperative mechanisms of mitotic spindle formation. *Journal of Cell Science* **120**, 1717–1722 (2007).

[72] Wolpert, L. Positional information and the spatial pattern of cellular differentiation. *Journal of theoretical biology* **25**, 1–47 (1969).

[73] Montagne, K., Plasson, R., Sakai, Y., Fujii, T. & Rondelez, Y. Programming an in vitro DNA oscillator using a molecular networking strategy. *Molecular systems biology* **7**, 466 (2011).

[74] Kim, J., White, K. S. & Winfree, E. Construction of an in vitro bistable circuit from synthetic transcriptional switches. *Mol. Syst. Biol.* **2**, 68 (2006).

[75] Fujii, T. & Rondelez, Y. PredatorPrey molecular ecosystems. *Acs Nano* **7**, 27–34 (2013).

[76] Padirac, A., Fujii, T. & Rondelez, Y. Bottom-up construction of in vitro switchable memories. *Proc. Natl. Acad. Sci. U.S.A.* **109**, E3212–20 (2012).

[77] Bauer, G., JS, M. & Otten, H. Traveling waves of in vitro evolving RNA. *Proc National Acad Sci* **86**, 7937–7941 (1989).

[78] Isalan, M., Lemerle, C. & Serrano, L. Engineering gene networks to emulate drosophila embryonic pattern formation. *Plos Biol* **3**, e64 (2005).

[79] Padirac, A., Fujii, T., Andre, E. & Rondelez, Y. Spatial waves in synthetic biochemical networks. *J Am Chem Soc* **135**, 14586–14592 (2013).

[80] Zadorin, A. S., Rondelez, Y., Galas, J. & André, E. Synthesis of programmable Reaction-Diffusion fronts using DNA catalyzers. *Phys Rev Lett* **114**, 068301 (2015).

[81] Zadorin, A. S. *et al.* Synthesis and materialization of a reactiondiffusion french flag pattern. *Nat Chem* (2017).

[82] Chirieleison, S., Allen, P., Simpson, Z. & Ellington, A. Pattern transformation with DNA circuits. *Nature* (2013).

[83] Scalise, D. & Schulman, R. Designing modular reaction-diffusion programs for complex pattern formation. *Technology* **02**, 55–66 (2014).

[84] Dalchau, N., Seelig, G. & Phillips, A. *Computational Design of Reaction-Diffusion Patterns Using DNA-Based Chemical Reaction Networks*, vol. 8727 (springer, 2014).

[85] Zenk, J. *et al.* Stable DNA-based reactiondiffusion patterns. *Rsc Adv* **7**, 18032–18040 (2017).

[86] Muscat, R. A., Bath, J. & Turberfield, A. J. A programmable molecular robot. *Nano Letters* **11**, 982–987 (2011).

[87] Agapakis, C. M., Boyle, P. M. & Silver, P. A. Natural strategies for the spatial optimization of metabolism in synthetic biology **8**, 527–535 (2012).

[88] Good, M. C., Zalatan, J. G. & Lim, W. A. Scaffold proteins: Hubs for controlling the flow of cellular information. *Science (New York, N.Y.)* **332**, 680–6 (2011).

[89] Morrison, D. & Davis, R. Regulation of MAP kinase signaling modules by scaffold proteins in mammals. *Annual review of cell and* (2003).

[90] Sweetlove, L. J. & Fernie, A. R. The spatial organization of metabolism within the plant cell. *Annu Rev Plant Biol* **64**, 723–46 (2013).

[91] Ellis, R. Macromolecular crowding: an important but neglected aspect of the intracellular environment. *Current opinion in structural biology* (2001).

[92] Konopka, M., Shkel, I., Cayley, S. & Record, M. Crowding and confinement effects on protein diffusion in vivo. *Journal of* (2006).

[93] Polka, J. K., Hays, S. G. & Silver, P. A. Building spatial synthetic biology with compartments, scaffolds, and communities. *Cold Spring Harbor Perspectives in Biology* **8** (2016).

[94] Park, S.-H., Zarrinpar, A. & Lim, W. A. Rewiring MAP kinase pathways using alternative scaffold assembly mechanisms. *Science (New York, N.Y.)* **299**, 1061–1064 (2003).

[95] Delebecque, C. J., Lindner, A. B., Silver, P. A. & Aldaye, F. A. Organization of intracellular reactions with rationally designed RNA assemblies. *Science (New York, N.Y.)* **333**, 470–474 (2011).

[96] Boemo, M. A., Lucas, A. E., Turberfield, A. J. & Cardelli, L. The Formal Language and Design Principles of Autonomous DNA Walker Circuits. *ACS Synthetic Biology* **5**, 878–884 (2016).

[97] Dannenberg, F., Kwiatkowska, M. Z., Thachuk, C. & Turberfield, A. J. DNA walker circuits: computational potential, design, and verification. *Natural Computing* **14**, 195–211 (2015).

[98] Mo, D., Lakin, M. R. & Stefanovic, D. Scalable design of logic circuits using an active molecular spider system. In *Lecture Notes in Computer Science*, vol. 9303, 13–28 (2015).

[99] Chen, Y.-J. *et al.* Programmable chemical controllers made from DNA. *Nature Nanotechnology* **8**, 755–62 (2013). NIHMS150003.

[100] Qian, L. & Winfree, E. Parallel and scalable computation and spatial dynamics with dna-based chemical reaction networks on a surface. In *Lecture Notes in Computer Science*, vol. 8727, 114–131 (2014).

[101] Teichmann, M., Kopperger, E. & Simmel, F. C. Robustness of localized DNA strand displacement cascades. *ACS Nano* **8**, 8487–8496 (2014).

[102] Dunn, K. E., Trefzer, M. A., Johnson, S. & Tyrrell, A. M. Investigating the dynamics of surface-immobilized DNA nanomachines. *Scientific Reports* **6**, 29581 (2016).

[103] Gerasimova, Y. V. & Kolpashchikov, D. M. Towards a dna nanoprocessor: Reusable tile-integrated dna circuits. *Angewandte Chemie International Edition* **55**, 10244–10247 (2016).

[104] Jung, J., Hyun, D. & Shin, Y. Physical synthesis of DNA circuits with spatially localized gates. In *33rd IEEE International Conference on Computer Design, ICCD 2015, New York City, NY, USA, October 18-21, 2015*, 259–265 (2015).

[105] Genot, A. J., Zhang, D. Y., Bath, J. & Turberfield, A. J. Remote toehold: A mechanism for flexible control of DNA hybridization kinetics. *Journal of the American Chemical Society* **133**, 2177–2182 (2011).

[106] Lakin, M. R., Petersen, R. L., Gray, K. E. & Phillips, A. Abstract modelling of tethered DNA circuits. In *Lecture Notes in Computer Science*, vol. 8727, 132–147 (2014).

[107] Groves, B. *et al.* Computing in mammalian cells with nucleic acid strand exchange. *Nature Nanotechnology* 1–18 (2015).

[108] He, Y. & Liu, D. R. Autonomous multistep organic synthesis in a single isothermal solution mediated by a DNA walker. *Nature Nanotechnology* **5**, 778–82 (2010).

[109] Meng, W. *et al.* An autonomous molecular assembler for programmable chemical synthesis. *Nature Chemistry* **8**, 542–8 (2016).

[110] Zadeh, J. *et al.* Nupack: Analysis and design of nucleic acid systems. *Journal of Computational Chemistry* **32**, 170–173 (2011).

[111] Ouldridge, T. E., Louis, A. A. & Doye, J. P. Structural, mechanical, and thermodynamic properties of a coarse-grained DNA model. *The Journal of chemical physics* **134**, 085101 (2011).

[112] Snodin, B. *et al.* Introducing improved structural properties and salt dependence into a coarse-grained model of DNA. *The Journal of Chemical Physics* **142**, 234901 (2015).

[113] Wei, X., Nangreave, J., Jiang, S., Yan, H. & Liu, Y. Mapping the thermal behavior of DNA origami nanostructures. *Journal of the American Chemical Society* **135**, 6165–6176 (2013).

[114] Dunn, K. E. *et al.* Guiding the folding pathway of DNA origami. *Nature* **525**, 82–86 (2015).

[115] Crick, F. *et al.* Central dogma of molecular biology. *Nature* **227**, 561–563 (1970).

[116] Landgraf, P. *et al.* A mammalian microrna expression atlas based on small rna library sequencing. *Cell* **129**, 1401–1414 (2007).

[117] Golub, T. R. *et al.* Molecular classification of cancer: class discovery and class prediction by gene expression monitoring. *science* **286**, 531–537 (1999).

[118] Young, R. A. Control of the embryonic stem cell state. *Cell* **144**, 940–954 (2011).

[119] Ernst, J. *et al.* Mapping and analysis of chromatin state dynamics in nine human cell types. *Nature* **473**, 43–49 (2011).

[120] Polyak, K. & Weinberg, R. A. Transitions between epithelial and mesenchymal states: acquisition of malignant and stem cell traits. *Nature Reviews Cancer* **9**, 265–273 (2009).

[121] Mittelbrunn, M. & Sánchez-Madrid, F. Intercellular communication: diverse structures for exchange of genetic information. *Nature reviews Molecular cell biology* **13**, 328–335 (2012).

[122] Lu, J. *et al.* Microrna expression profiles classify human cancers. *nature* **435**, 834–838 (2005).

[123] Li, G.-W. & Xie, X. S. Central dogma at the single-molecule level in living cells. *Nature* **475**, 308–315 (2011).

[124] Wong, M. L. & Medrano, J. F. Real-time pcr for mrna quantitation. *Biotechniques* **39**, 75 (2005).

[125] Gottardo, F. *et al.* Micro-rna profiling in kidney and bladder cancers. In *Urologic Oncology: Seminars and Original Investigations*, vol. 25, 387–392 (Elsevier, 2007).

[126] Cummins, J. & Velculescu, V. Implications of micro-rna profiling for cancer diagnosis. *Oncogene* **25**, 6220–6227 (2006).

[127] Calin, G. A. *et al.* Microrna profiling reveals distinct signatures in b cell chronic lymphocytic leukemias. *Proceedings of the National Academy of Sciences of the United States of America* **101**, 11755–11760 (2004).

[128] Habib, A. M. *et al.* Overlap of endocrine hormone expression in the mouse intestine revealed by transcriptional profiling and flow cytometry. *Endocrinology* **153**, 3054–3065 (2012).

[129] Raj, A., Van Den Bogaard, P., Rifkin, S. A., Van Oudenaarden, A. & Tyagi, S. Imaging individual mrna molecules using multiple singly labeled probes. *Nature methods* **5**, 877 (2008).

[130] Femino, A. M., Fay, F. S., Fogarty, K. & Singer, R. H. Visualization of single rna transcripts in situ. *Science* **280**, 585–590 (1998).

[131] Chen, K. H., Boettiger, A. N., Moffitt, J. R., Wang, S. & Zhuang, X. Spatially resolved, highly multiplexed rna profiling in single cells. *Science* **348**, aaa6090 (2015).

[132] Tiller, T. *et al.* Efficient generation of monoclonal antibodies from single human b cells by single cell rt-pcr and expression vector cloning. *Journal of immunological methods* **329**, 112–124 (2008).

[133] Warren, L., Bryder, D., Weissman, I. L. & Quake, S. R. Transcription factor profiling in individual hematopoietic progenitors by digital rt-pcr. *Proceedings of the National Academy of Sciences* **103**, 17807–17812 (2006).

[134] Golding, I., Paulsson, J., Zawilski, S. M. & Cox, E. C. Real-time kinetics of gene activity in individual bacteria. *Cell* **123**, 1025–1036 (2005).

[135] Tyagi, S., Kramer, F. R. *et al.* Molecular beacons: probes that fluoresce upon hybridization. *Nature biotechnology* **14**, 303–308 (1996).

[136] Vargas, D. Y., Raj, A., Marras, S. A., Kramer, F. R. & Tyagi, S. Mechanism of mrna transport in the nucleus. *Proceedings of the National Academy of Sciences of the United States of America* **102**, 17008–17013 (2005).

[137] Smith, A. M. *et al.* Highly-multiplexed barcode sequencing: an efficient method for parallel analysis of pooled samples. *Nucleic acids research* gkq368 (2010).

[138] Lee, J. H. *et al.* Highly multiplexed subcellular rna sequencing in situ. *Science* **343**, 1360–1363 (2014).

[139] Raj, A. & van Oudenaarden, A. Single-molecule approaches to stochastic gene expression. *Annual review of biophysics* **38**, 255–270 (2009).

[140] Zhang, X. *et al.* Quantitative assessment of ratiometric bimolecular beacons as a tool for imaging single engineered rna transcripts and measuring gene expression in living cells. *Nucleic acids research* **41**, e152–e152 (2013).

[141] Köhler, A. & Hurt, E. Exporting rna from the nucleus to the cytoplasm. *Nature reviews Molecular cell biology* **8**, 761–773 (2007).

[142] Alberts, B. *et al.* The transport of molecules between the nucleus and the cytosol (2002).

[143] Stewart, M. P. *et al.* In vitro and ex vivo strategies for intracellular delivery. *Nature* **538**, 183–192 (2016).

[144] Resch-Genger, U., Grabolle, M., Cavaliere-Jaricot, S., Nitschke, R. & Nann, T. Quantum dots versus organic dyes as fluorescent labels. *Nature methods* **5**, 763–775 (2008).

[145] Kumaraswamy, S. *et al.* Fluorescent-conjugated polymer superquenching facilitates highly sensitive detection of proteases. *Proceedings of the National Academy of Sciences of the United States of America* **101**, 7511–7515 (2004).

[146] Altman, R. B. *et al.* Cyanine fluorophore derivatives with enhanced photostability. *Nature methods* **9**, 68–71 (2012).

[147] Mueller, F. *et al.* Fish-quant: automatic counting of transcripts in 3d fish images. *Nature Methods* **10**, 277–278 (2013).

[148] Lones, M. A., Tyrrell, A. M., Smith, S. L. & Fogel, G. B. (eds.). *Information Processing in Cells and Tissues - 10th International Conference, IPCAT 2015, San Diego, CA, USA, September 14-16, 2015, Proceedings*, vol. 9303 of *Lecture Notes in Computer Science* (Springer, 2015).

[149] Cardelli, L. & Shih, W. M. (eds.). *DNA Computing and Molecular Programming - 17th International Conference, DNA 17, Pasadena, CA, USA, September 19-23, 2011. Proceedings*, vol. 6937 of *Lecture Notes in Computer Science* (Springer, 2011).

[150] Murata, S. & Kobayashi, S. (eds.). *DNA Computing and Molecular Programming - 20th International Conference, DNA 20, Kyoto, Japan, September 22-26, 2014. Proceedings*, vol. 8727 of *Lecture Notes in Computer Science* (Springer, 2014).

[151] *33rd IEEE International Conference on Computer Design, ICCD 2015, New York City, NY, USA, October 18-21, 2015* (IEEE Computer Society, 2015).

[152] Mullor Ruiz, I. *et al.* Connecting localized dna strand displacement reactions. *Nanoscale* **7**, 12970–12978 (2015).

[153] Nielsen, A. A. K. *et al.* Genetic circuit design automation. *Science (New York, N.Y.)* **352**, aac7341 (2016).

[154] Xie, Z., Wroblewska, L., Prochazka, L., Weiss, R. & Benenson, Y. Multi-input RNAi-based logic circuit for identification of specific cancer cells. *Science (New York, N.Y.)* **333**, 1307–11 (2011).

[155] Zhang, D. Y. & Winfree, E. Control of DNA strand displacement kinetics using toehold exchange. *J Am Chem Soc* **131**, 17303–17314 (2009).

[156] Elowitz, M. B. & Leibler, S. A synthetic oscillatory network of transcriptional regulators. *Nature* **403**, 335–338 (2000).

[157] Niederholtmeyer, H. *et al.* Rapid cell-free forward engineering of novel genetic ring oscillators. *eLife* **4**, 1–18 (2015).

[158] Jung, C., Allen, P. B. & Ellington, A. D. A stochastic DNA walker that traverses a microparticle surface. *Nature Nanotechnology* **11**, 1–8 (2015).

[159] Purnick, P. E. M. & Weiss, R. The second wave of synthetic biology: from modules to systems. *Nature reviews. Molecular cell biology* **10**, 410–22 (2009).

[160] Martin, J. & Hartl, F. The effect of macromolecular crowding on chaperonin-mediated protein folding. *Proceedings of the National Academy of Sciences* **94**, 1107–1112 (1997).

[161] Lakin, M. R., Youssef, S., Polo, F., Emmott, S. & Phillips, A. Visual DSD: A design and analysis tool for DNA strand displacement systems. *Bioinformatics* **27**, 3211–3213 (2011).

[162] Hindmarsh, A. C. *et al.* SUNDIALS: Suite of Nonlinear and Differential/Algebraic Equation Solvers. *ACM Transactions on Mathematical Software* **31**, 363–396 (2005).

[163] Phillips, A. & Cardelli, L. A programming language for composable DNA circuits. *Journal of the Royal Society, Interface / the Royal Society* **6 Suppl 4**, S419–S436 (2009).

[164] Bonnet, G., Krichevsky, O. & Libchaber, A. Kinetics of conformational fluctuations in dna hairpin-loops. *Proceedings of the National Academy of Sciences* **95**, 8602–8606 (1998).

[165] Liedl, T., Sobey, T. & Simmel, F. DNA-based nanodevices. *Nano Today* (2007).

[166] Wang, D. *et al.* Molecular logic gates on DNA origami nanostructures for microRNA diagnostics. *Anal. Chem.* **86**, 1932–6 (2014).

[167] Yin, P., Choi, H. M., Calvert, C. R. & Pierce, N. A. Programming biomolecular self-assembly pathways. *Nature* **451**, 318–22 (2008).

[168] Bath, J., Green, S. J., Allen, K. E. & Turberfield, A. J. Mechanism for a directional, processive, and reversible DNA motor. *Small* **5**, 1513–6 (2009).

[169] Bath, J., Green, S. & Turberfield, A. A FreeRunning DNA motor powered by a nicking enzyme. *Angew. Chem. Int. Ed.* **44**, 4358–4361 (2005).

[170] Frezza, B. M., Cockroft, S. L. & Ghadiri, M. Modular multi-level circuits from immobilized DNA-based logic gates. *J. Am. Chem. Soc.* **129**, 14875–9 (2007).

[171] Picuri, J. M., Frezza, B. M. & Ghadiri, M. Universal translators for nucleic acid diagnosis. *J. Am. Chem. Soc.* **131**, 9368–77 (2009).

[172] Ke, Y., Voigt, N. V., Gothelf, K. V. & Shih, W. M. Multilayer DNA origami packed on hexagonal and hybrid lattices. *J Am Chem Soc* **134**, 1770–1774 (2012).

[173] Kopperger, E., Pirzer, T. & Simmel, F. Diffusive transport of molecular cargo tethered to a DNA origami platform. *Nano letters* (2015).

[174] Woo, S. & Rothemund, P. W. Programmable molecular recognition based on the geometry of DNA nanostructures. *Nat Chem* **3**, 620–7 (2011).

[175] Jung, C. & Ellington, A. Diagnostic applications of nucleic acid circuits. *Accounts of chemical research* (2014).

[176] Saaem, I. & H, L. T. Overview of DNA origami for molecular self assembly **5**, 150–162 (2013).

[177] Santangelo, P. J. *et al.* Single molecule-sensitive probes for imaging RNA in live cells. *Nat. Methods* **6**, 347–9 (2009).

[178] Maya, K., Douek, Y., Adar, R. & Shapiro, E. A library of programmable DNAzymes that operate in a cellular environment. *Sci Rep* **3**, 1535 (2013).

[179] He, Y. *et al.* Hierarchical self-assembly of DNA into symmetric supramolecular polyhedra. *Nature* **452**, 198–201 (2008).

[180] Allen, P., Arshad, S., Li, B., Chen, X. & Ellington, A. DNA circuits as amplifiers for the detection of nucleic acids on a paperfluidic platform. *Lab on a Chip* (2012).

[181] Teller, C. & Willner, I. Functional nucleic acid nanostructures and DNA machines. *Current opinion in biotechnology* (2010).

[182] Shu, W., Liu, D., Watari, M. & Riener, C. DNA molecular motor driven micromechanical cantilever arrays. *Journal of the* (2005).

[183] Wang, Z., Elbaz, J. & Willner, I. DNA machines: bipedal walker and stepper. *Nano letters* (2010).

[184] Surana, S., Bhat, J., Koushika, S. & Krishnan, Y. An autonomous DNA nanomachine maps spatiotemporal pH changes in a multicellular living organism. *Nature communications* (2011).

[185] Kuzuya, A., Watanabe, R., Yamanaka, Y. & Tamaki, T. Nanomechanical DNA origami pH sensors. *Sensors* (2014).

[186] and Berger, Y., Liber, M., Avrahami, D., Gerber, D. & Nir, E. A DNA bipedal motor achieves a large number of steps due to operation using Microfluidics-Based interface. *ACS* (2017).

[187] Tian, Y. & Mao, C. Molecular gears: a pair of DNA circles continuously rolls against each other. *Journal of the American Chemical Society* (2004).

[188] Buranachai, C., SA, M. & Ha, T. Single molecule nanometronome. *Nano letters* (2006).

[189] Maune, H., Han, S., Barish, R. & Bockrath, M. Self-assembly of carbon nanotubes into two-dimensional geometries using DNA origami templates. *Nature* (2010).

[190] Linko, V., Eerikäinen, M. & Kostiainen, M. A modular DNA origami-based enzyme cascade nanoreactor. *Chemical Communications* (2015).

[191] Schreiber, R., Do, J., Roller, E. & Zhang, T. Hierarchical assembly of metal nanoparticles, quantum dots and organic dyes using DNA origami scaffolds. *Nature* (2014).

[192] Fu, Y., Zeng, D., Chao, J., Jin, Y. & Zhang, Z. Single-step rapid assembly of DNA origami nanostructures for addressable nanoscale bioreactors. *Journal of the* (2012).

[193] Genot, A. *et al.* High-resolution mapping of bifurcations in nonlinear biochemical circuits. *Nat Chem* **8**, 760–767 (2016).

[194] Sugiura, H. *et al.* Pulse-density modulation control of chemical oscillation far from equilibrium in a droplet open-reactor system. *Nat Commun* **7**, 10212 (2016).

[195] Niederholtmeyer, H., Stepanova, V. & Maerkl, S. J. Implementation of cell-free biological networks at steady state. *Proc. Natl. Acad. Sci. U.S.A.* **110**, 15985–90 (2013).

[196] Hasatani, K. *et al.* High-throughput and long-term observation of compartmentalized biochemical oscillators. *Chem Commun* **49**, 8090–8092 (2013).

[197] Simpson, Z., Tsai, T. L., Nguyen, N., Chen, X. & Ellington, A. D. Modelling amorphous computations with transcription networks. *J R Soc Interface* **6**, S523–S533 (2009).

[198] Mhlanga, M. M. & Tyagi, S. Using tRNA-linked molecular beacons to image cytoplasmic mRNAs in live cells. *Nat Protoc* **1**, 1392–1398 (2006).